

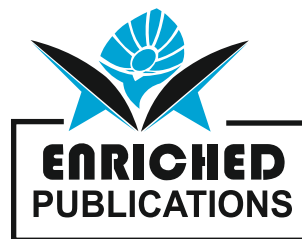
ISSN: 0973-6778

# International Journal of Computational Vision and Biomechanics

**Volume No. 10**

**Issue No. 1**

**January - April 2024**



**ENRICHED PUBLICATIONS PVT.LTD**

**JE - 18, Gupta Colony, Khirki Extn,  
Malviya Nagar, New Delhi - 110017.**

**E- Mail: [info@enrichedpublication.com](mailto:info@enrichedpublication.com)**

**Phone :- +91-8877340707**

ISSN: 0973-6778

# **International Journal of Computational Vision and Biomechanics**

**Managing Editor**

Mr. Amit Prasad

# International Journal of Computational Vision and Biomechanics

(Volume No. 10, Issue No. 1, January - April 2024)

## Contents

Sr. No	Article/ Authors	Pg No
01	Parametric Geometrical Subject-specific Finite Element Models of the Proximal Femur: A Tool to Predict Slipped Capital Femoral Epiphyses - <i>O. Pasetaa, M. J. Gómez-Benitoa, J.M. García-Aznara, C. Barriosb, M. Doblaréa.</i>	1 - 11
02	A Framework for 3D Reconstruction of Human Organs from MR Images: A Model and Fuzzy Set Principles Based Approach. Application to Prostate Segmentation and Reconstruction - <i>Betrouni N.1 &amp; Vermandel M.1</i>	12 - 25
03	Material Properties and Extended Sources for Surface Rendering - <i>Jan J. Koenderink &amp; Sylvia C. Pont</i>	26 - 38
04	Computational Study on Bone Remodeling and Osseointegration for a Hip Replacement using a Conservative Femoral Stem - <i>J. Folgado*, P. R. Fernandes and H. C. Rodrigues</i>	39 - 54
05	Computational Modelling of Ligaments at Non-physiological Situations - <i>B. Calvo, E. Peña, M.A. Martínez and M. Doblaré</i>	55 - 68



---

# Parametric Geometrical Subject-specific Finite Element Models of the Proximal Femur: A Tool to Predict Slipped Capital Femoral

O. Pasetaa, M. J. Gómez-Benitoa, J.M. García-Aznara, C. Barriosb, M. Doblaréa.

aGroup of Structural Mechanics and Materials Modelling, Aragon Institute of Engineering Research (13A)University of Zaragoza, María de Luna s/n, 50018, Zaragoza, Spain

bOrthopaedics and Trauma Unit, Department of Surgery, Valencia University Medical School, Valencia,

## **ABSTRACT**

*Different anatomical and mechanical factors inducing growth plate overloading have been implicated in the etiology of Slipped Capital Femoral Epiphysis (SCFE). Loading and the subsequent risk of fracture at the epiphyseal growth plate of the femoral head have been poorly investigated so far, so in this work, we analyse Slipped Capital Femoral Epiphysis from a mechanical point of view. The aim of this research is to determine the influence of the proximal femoral geometry on the growth plate slippage. This is accomplished by means of Finite Element Analyses (FEA) of a parametric model of the proximal femur previously created. An adolescent standardized femur is defined based on average geometrical parameters collected in literature of healthy and slipped hips. In order to evaluate the potential of this parametric model, we compared successfully their results with those obtained using models from actual geometries of a pre-SCFE and a healthy hip of a child. Next, this parametric model is adapted to simulate subject specific situations. The most important parameters: the Physis Sloping Angle (PSA) and the Posterior Sloping Angle of the Physis (L), are varied and their effect under the same loads corresponding to walking and stairs climbing is investigated. The computed results show a strong dependence of the growth plate failure on the geometry of the proximal femur. Higher values of the Physis Sloping Angle (PSA) and the Posterior Sloping Angle (L) are related to higher growth plate stresses and therefore to a more likely slippage. The highest stress level is always found in the medial region of the physis, a site where usually growth plate starts to fail.*

**Key words:** *Slipped Capital Femoral Epiphysis, Finite Element Analysis, Growth Plate, Biomechanical Parametric Model.*

## **1. INTRODUCTION**

Slipped Capital Femoral Epiphysis (SCFE) is the most common disorder of the adolescent hip [1]. It occurs in 5 of 100.000 children from 10 to 15 years old [2,3]. SCFE consists on a posterior and medial slippage of the proximal femoral epiphysis at the metaphysis, occurring through the physeal plate. The diagnosis of SCFE is, unfortunately, not easy in many cases which implies a delay in its treatment. This delay results in a less favorable long-term prognosis [1] and risk of other secondary effects, such as, osteonecrosis of the femoral head [4] and degenerative hip arthritis [1]. Thus, it is very important to develop predictive methods for early detection of SCFE.

Different factors such as endocrine disorders [5] and radiation therapy [6] have been found to be associated with the development of SCFE. However, in most cases the aetiology remains unknown.

---

Idiopathic SCFE has been related to many factors, including overweight [7], physeal orientation [8,9], abnormalities in the physeal architecture [10,11] and hormonal changes during adolescence that affect the physeal strength [1].

The stress magnitude at the femoral capital physis under physiological and overweight loads has not been sufficiently addressed. To our knowledge, the analysis of the different factors affecting SCFE have been mainly focused on several geometrical features of the proximal femur and parameters such as weight, height or age of the patient [8,9]. However, mechanical factors, such as strain and stress distributions on the growth plate, which could explain failure of the proximal growth plate have not been fully studied. A recent work of Fishkin et al. [12] analyzed the stress distribution in the growth plate in the stance phase activity varying the angle of the femoral neck version. We also recently presented a finite element model of both proximal femora of a child affected by pre-SCFE in his left leg and compared the distribution of stresses in both growth plates when performing different activities [13]. However, a wider study is needed to determine the stress distributions at the proximal femur physeal plate on different patients. Indeed, the determination of the stress level in the growth plate could help to estimate the subjects with a higher probability of slippage.

When a Finite Element model is developed, segmentation of the proximal femur and generation of the associated FE mesh are the most time consuming parts of the process. In this work, we propose the use of a parametric model, where the proximal femur geometry is simplified and defined through a set of anatomical parameters: NeckDiaphysis Angle, Neck Shaft Plate Shaft Angle, Head radius, Medullary channel width; which can be easily adapted to each specific subject. This simplified geometry can be meshed by means of automatic mesh generation

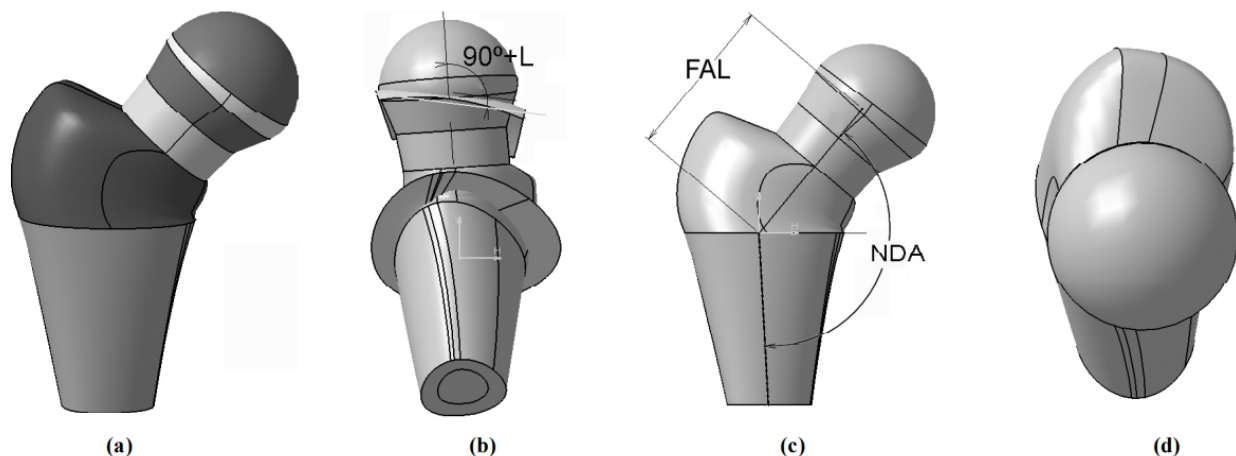


**Figure 1:** Parametrized geometry of the proximal femur (a) different primitive geometries; (b) lateral view; (c) anterior-posterior view; (d) upper view.

programs with good finite element aspect ratios for all the mesh. This model can help to determine the risk of development of SCFE, based on the geometrical morphology of each specific patient's hip. Therefore, the aim of this paper is to develop a model for the parametrized geometry of the proximal femur and evaluate differences in the stress distribution that appears in the growth plate for different femoral configurations.

## 2. MATERIAL AND METHODS

A parametric geometry of the proximal femur including epiphyseal growth plate was developed, based on several parameters that determine the geometry of the proximal femur: head radius (*HR*), physeal

width ( $PW$ ), neck shaftneck plate angle ( $NSNPA$ ), posterior sloping angle ( $L$ ), physis-diaphysis angle ( $PDA$ ), cortical thickness ( $CT$ ), femoral neck width ( $FNW$ ), diaphyseal width ( $DW$ ) (Figs. 1 and 3). These parameters can be trivially modified to simulate different femurs and plates, being therefore easily to adapt to each specific subject.

To develop this parametric model we initially reconstructed the geometry of both proximal femora of a 14-year-old boy with pre-SCFE in his left hip from a set of CT scans. The geometry of these femurs and epiphyseal plates were simplified by means of primitive geometries (Fig. 1.a) and reconstructed through the CAD-program Catia [14]. Then, it was automatically meshed by Harpoon [15] (Fig. 4) with hexahedral elements of characteristic length of 3mm. The geometry of this parametric model can be easily resized and modified to simulate different geometries, a scheme of the process followed to simulate the different geometries and the time consumed in each step could be observed in figure 2.

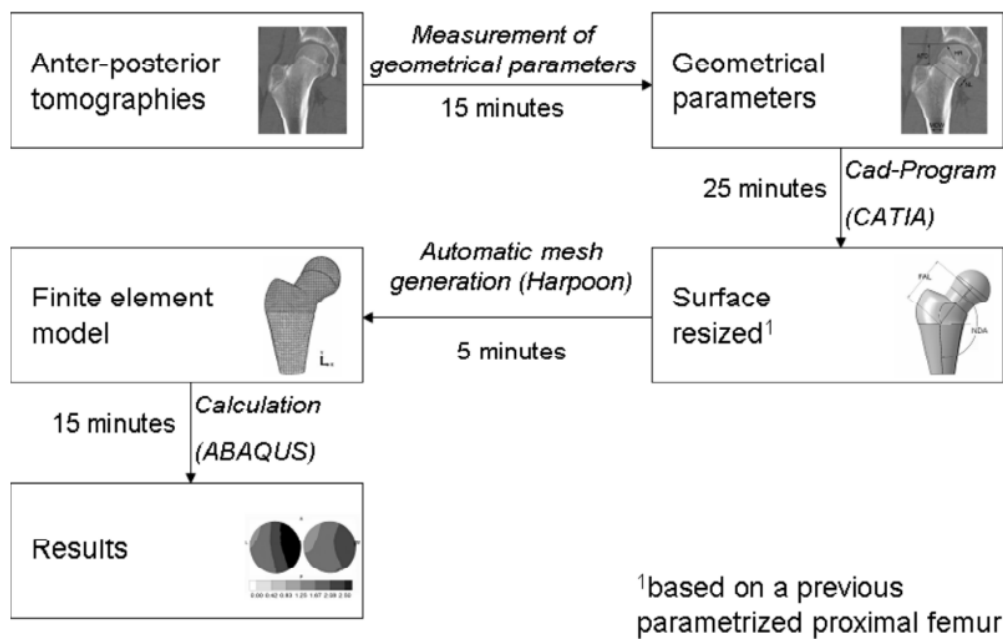


**Figure 2:** Scheme of the process to obtain the specific subject finite element model including the approximate time consumed in each step.

In order to address the main aim of this paper, three different analyses were performed. First, we evaluated the accuracy of the parametric model. Hence, we developed four finite element models, two of them based on the actual geometry of the two femurs of a 14-year-old boy with preSCFE in his left hip and body weight of 92kg, whereas the other two were based on the parametrized geometry of these same femurs. In the second set of analyses, we created two additional independent parametrised models to determine the influence of the overall geometry into the growth plate slippage. The parametrised geometry of these femurs was based on measurements of morphometric parameters of a previous study of 36 healthy hips and 47 unaffected hips of patients with unilateral SCFE [8]. The mean values of these parameters were used to reconstruct the parametrised geometry of a healthy “standardised” femur and a “standardised” non-slipped hip of children with unilateral SCFE. This second femur has been reported to be more prone to suffer slippage [8]. The body weight for both “standardised” femurs was estimated in 58.8kg [8] in order to minimize the influence of the body weight on the results. Finally, we performed a sensitivity analysis with respect to different geometrical parameters that are the most determinant in the development of SCFE [8] in order to determine their respective individual influence: the physeal sloping angle ( $PSA$ ) and the posterior sloping angle ( $L$ ) were varied in ten degrees in two independent

models based on the geometry of the “standardised” healthy femur.

The geometrical parameters which define the geometry of the simulated femurs are summarized in table 1. In all cases, the growth plate thickness was assumed constant and estimated in 1mm [16]. We considered three different materials: cartilage for the growth plate, trabecular and cortical bone. Linear elastic isotropic behavior was assumed for all of them with elastic moduli of 5MPa, 700MPa and 17000MPa and Poisson’s ratios of 0.45, 0.2 and 0.3 respectively [17,18,19]. Different loading conditions were simulated in each analysis: (1) heel strike during walking; (2) midstance; (3) toe off; (4) heel strike during stairs climbing. These loads were applied on the femoral head including also the reaction at the abductor. Both were scaled by the body weight of the patient (Table 2)[20].

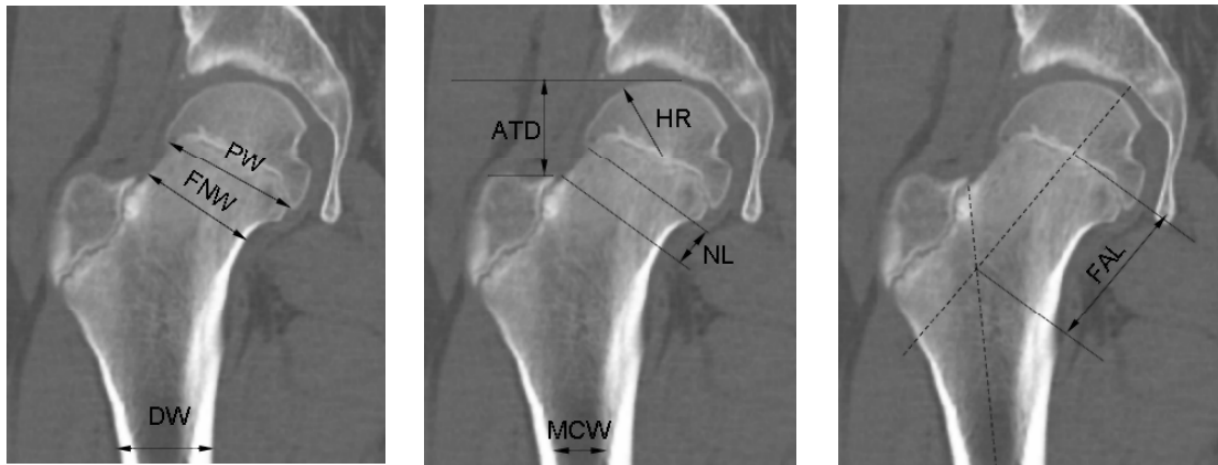


**Figure 3:** Geometrical parameters of the defined femurs measured on anterior-posterior tomographies (acronyms are fully defined in table 1)

Growth plate failure is assumed to be mainly produced by a combination of shear stresses, which may induce slip of the head, and tensile stresses, that might tear up the growth plate from the trabecular bone [10,11,21,22,23]. In order to estimate the growth plate risk to failure, we chose the Tresca failure criterion because it is the most appropriate for shear failure. We could also consider von Mises stresses which takes into account normal and shear stresses. In fact, von Mises stress for the analysed load cases were qualitatively similar to Tresca’s although the latter resulted slightly lower, the conclusions drawn from von Mises stress distributions were the same than those obtained from Tresca stresses [13].

### 3. RESULTS

First, the distributions of Tresca stresses and the maximum value of these stresses at the growth plate were compared between the models developed for actual and parametric geometries of these femurs. Second, we analysed the stress distribution on the two standardised healthy and affected femurs. Finally, the stress distribution was studied for the standardised healthy femur after modifying the posterior slopping angle (PSA) in  $10^\circ$  and the physeal slopping angle (L) also in  $10^\circ$ .

#### 3.1 Comparative validation of the parametric model

To evaluate the parametric model, the results obtained in a FE analysis of real geometry were compared to those computed from the parametrised geometry. The Tresca stress distributions for the different activities simulated at the growth plate are shown from an upper view in figure 5. The load transfer mechanism through the growth plate in both models was very similar. A stress concentration at the

medial

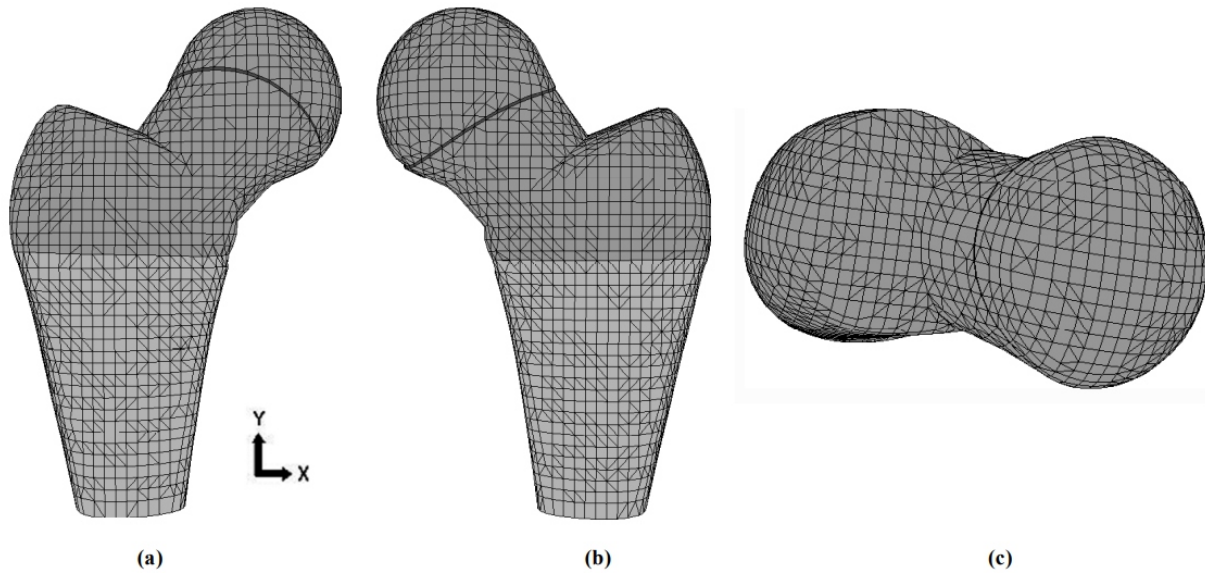


**Figure 4:** Finite element model of the healthy femur including the growth plate based on the parametrised geometry.

**Table 1** Geometrical Parameters of the Simulated Femurs [8,13].

Geometric Parameters	Patient		"Standardised" [8]		Sensitivity analysis	
	Healthy	pre-SCFE	Healthy	Affected	L angle	PSA
Growth Plate Area (cm <sup>2</sup> )	30,9	24,7	15.2	14.5	15.2	15.2
Neck-Diaphysis Angle (NDA) (o)	48	51	39.2	39.2	39.2	39.2
Neck Shaft Plate Shaft (NSPSA) (o)	18	14	8.1	4.6	8.1	1.7
Posterior Sloping Angle of Physis (L) (o)	11	13	5.0	13.6	<b>15.0</b>	5.0
Physcal slopping angle (PSA) (o)	26	34	30	34	30	<b>40</b>
Physcal diaphysis angle (PDA) (o)	59	55	59	55	59	49
Head radius (HR) (mm)	32.4	33	22	21.5	22	22
Femoral neck width (FNW) (mm)	26	24	17.5	17	17.5	17.5
Medullary channel width (MCW) (mm)	25	24	15	15	15	15
Diaphyseal width (DW) (mm)	40	40	28	28	28	28
Femoral axis length (FAL) (mm)	78	77	56	56	56	56
Articulo trochanteric distance (ATD) (mm)	35	33	25	23	25	25
Plate thickness (PT) (mm)	1	1	1	1	1	1
Neck length (NL) (mm)	18	20	14	14	14	14
Diaphyseal length (DL) (mm)	84	81	58.75	58.75	58.75	58.75

**Table 2** Components of the Femoral Loads for each Activity Simulated, Normalized to the Body Weight (BW) [20].

Reference Axes in **Figure 4**

Load case	Head Load (N)			Abductor Load (N)		
	X Dir.	Y Dir.	Z Dir.	X Dir.	Y Dir.	Z Dir.
Heel strike during walking	-0.32 · BW	-2.21 · BW	-2.95 · BW	0.78 · BW	0.76 · BW	0.14 · BW
Midstance	0.74 · BW	-0.86 · BW	-0.41 · BW	-0.34 · BW	0.05 · BW	0.02 · BW
Toe off	-0.36 · BW	-0.59 · BW	1.31 · BW	0.21 · BW	0.44 · BW	-0.13 · BW
Heel strike during climbing stairs	-0.41 · BW	-2.27 · BW	-0.70 · BW	0.89 · BW	1.00 · BW	0.32 · BW

area was observed at the heel strike moment during stairs climbing; this concentration was also medial in the pre-slipped hip, but oriented towards the anterior area in both parametric and real geometries at this pre-slipped hip. In addition, the maximum Tresca stresses were always higher for the pre-slipped hip when compared to the healthy model in both actual and parametrised geometries.

### 3.2 Standardised Femurs

The parametrised geometry of the femur was adapted to the geometry of a “standardised” healthy femur and a “standardised” non-affected hip of children with unilateral SFCE. The healthy growth plate of the SCFE-affected child exhibited higher stresses (Fig. 6) than the growth plate of the healthy femur used as control. During heel strike, while

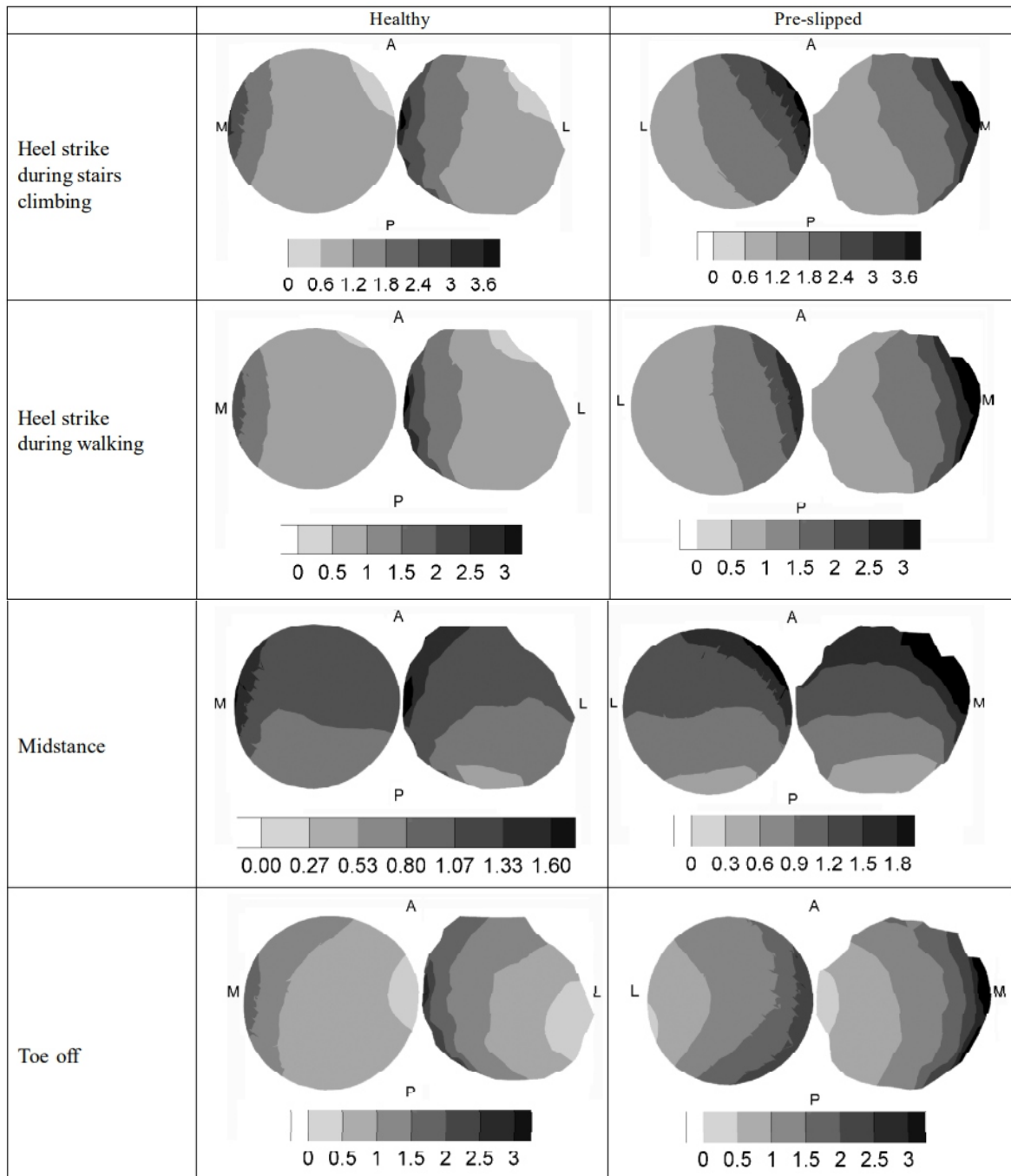


**Figure 5:** Distributions of Tresca stresses (MPa) at the plates of a 14 year old child, models based on parametrised and real geometry (A-Anterior, P-Posterior, M-Medial, L-Lateral)

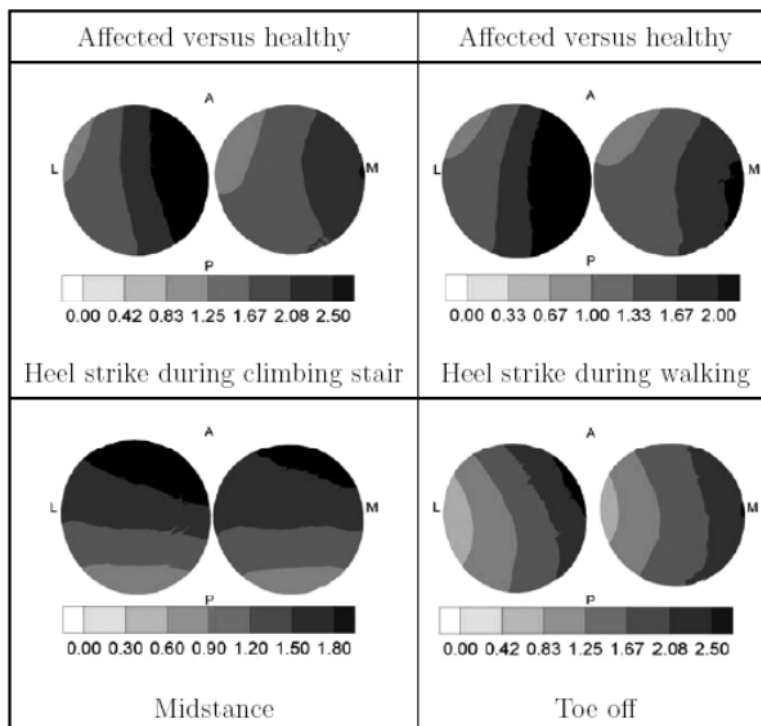


**Figure 6:** Distributions of Tresca stresses (MPa) at the parametrised growth plates of the “standardised” affected and “standardised” healthy femurs (A-Anterior, P-Posterior, M-Medial, L-Lateral).

stairs climbing, Tresca stresses over 2.5MPa were observed at the medial region of the affected growth plate. A stress concentration was also observed in this same region of the healthy hip, although with a lower value of the Tresca stress. No area appeared with stresses higher than 2.5MPa the difference was not so apparent at midstance and toe off, but the stresses were always higher for the affected hip than for the healthy one. At the midstance stage, the stress concentration was localized in the anterior region of the physis.

### 3.3 Influence of the Posterior Slopping Angle and the Physeal Slopping Angle

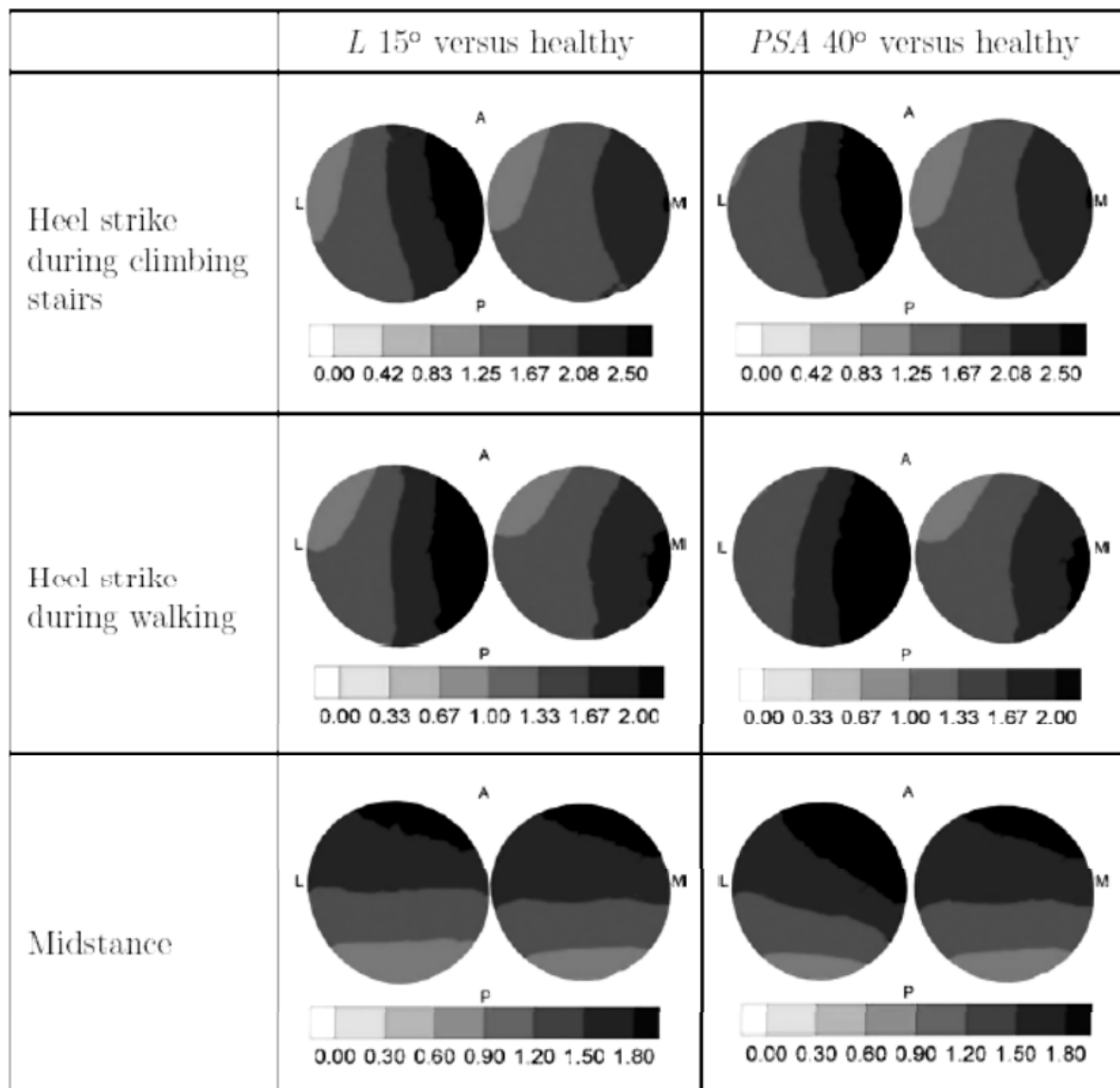
Tresca stresses increased with both angles: posterior slopping and physeal slopping. The greatest differences were observed when increasing the physeal slopping angle (Fig. 7). At the heel strike stage, during stairs climbing, a maximum Tresca stress of 2.15MPa for the standardised healthy growth plate was observed. This stress increased to values higher than 2.5MPa when increasing the L angle in 10° and the PSA in 10° (Fig. 7), being the area subjected to this stress bigger when increasing the PSA. The maximum Tresca stresses were localized in the medial region during heel strike and toe off, while this concentration appeared in the anterior region during the midstance phase.

## 4. DISCUSSION

This paper describes how a parametrised geometry of the proximal femur morphology of a child may be used to fastly obtain a prediction of the stress distribution at the growth plate and thus determine the risk of development of SCFE. Despite the qualitative character of the conclusions here obtained, the proposed model might be useful to determine if pinnig of the healthy femur can be recommended or not

in patients suffering from unilateral SCFE. To evaluate the potential of this parametrised model we performed a comparison between the results obtained by means of finite element simulations of actual geometries of the proximal femurs of a child and the parametrised geometry of these same femurs. The similar distributions of stresses computed in both growth plates validate the accuracy of the parametric finite element model. Even though the distributions were not identical, the parametrised model was able to identify the areas of maximum stresses and the maximum value of the Tresca stress with sufficient accuracy.

Assuming the same body weight, the differences observed between the standardised healthy femur and the parametrised unaffected femur of children with unilateral SCFE, indicate the strong influence of the geometrical parameters on the development of slipped capital epiphysis [8, 9, 24]. The differences in stresses when modifying the L



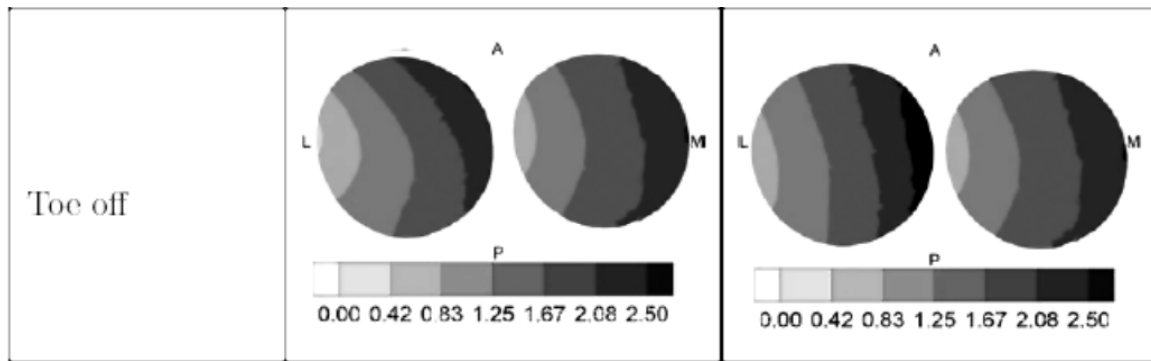


**Figure 7:** Distributions of Tresca stresses (MPa) at the parametrised growth plates of the standardised healthy femur when varying the L angle and PSA in  $10^\circ$  (A-Anterior, P-Posterior, M-Medial, L-Lateral).

and PSA angles follow a similar trend to that observed clinically [9,8]. Highest values of L and PSA angles resulted in higher stresses and therefore a higher probability of slippage. However, the same variation in L and PSA angle results in a different influence on the stress distribution. When modifying the L angle in  $10^\circ$  an increase of 15% was observed in the maximum Tresca stress at the heel strike moment during stairs climbing and walking. These differences were higher when increasing the PSA angle: an increase of the Tresca stress of about 35% was observed at the moment of heel strike.

The highest stress concentration was observed at the medial region of the physis at the heel strike moment during stairs climbing. Worse mechanical properties have been reported at the posterior-medial area of the physis [25]. These two facts could indicate the beginning of the plate failure in the medial region.

Despite the results obtained, we have to keep in mind that modelling in biomechanics involves a number of simplifications on different levels that have to be interpreted carefully. The main assumptions of this work are:

First, we assume all materials to be linear elastic. This hypothesis has been used by many authors in FE models of bone and cartilage [26] reporting sufficiently accurate results for this type of analyses. The mechanical properties used for the growth plate were determined from animal experiments [10,11]. We have to remark the few experimental works designed to obtain mechanical properties of femoral growth plates [21]. There are several works to determine the mechanical properties in bovine tibial growth plates. Ultimate shear stress was reported to be between 1.66MPa and 3.81MPa depending on the anatomical location [11] and tensile stress between 0.83MPa and 1.89MPa [10]. In bovine distal femora the maximum and average ultimate tensile stress registered were 5MPa and 3MPa respectively [25]. The differences reported may be due to biologic variations, animal specie, anatomic form of the growth plate and testing modalities. To our knowledge, there are very few experimental works performed to determine mechanical properties of human growth plates, thus the properties had to be extracted from animal experiments and our results has to be analysed from a qualitative point of view. The same elastic moduli and Poisson's ratios were considered for the simulated hips despite the fact that these properties decrease in slipped hips [27].

Second, the applied forces used to drive the simulations were considered the same (just scaled by the body weight) for healthy, pre-slipped and unaffected hips of children affected by unilateral SCFE, although they are likely to vary between normal and diseased children due to compensatory mechanisms [27].

Third, other effects such as the influence of cyclic loads that could produce fatigue and a possible

---

increment of cartilage stiffness due to closing of cartilage pores by plate compression have not been considered in this approach. As has been reported in a previous work [13], we do not take into consideration the poroelastic behavior of the growth plate because the same conclusions as in the elastic model may be drawn.

Finally, the growth plate was considered homogeneous not taking into account its microstructural properties which may vary with age and sex. The microstructural geometry and mechanical properties of the physis could influence the failure mechanism locally [28]; however we are most interested in the global failure mechanism. Few experimental works have been performed to determine the mechanism of failure of the growth plate. Moen and Pelker [28] tested bovine femurs and tibias to determine the failure mechanism of the growth plate. They concluded that a different mechanism and zone of failure is expected when loading the specimens in tension, shear or compression. For each of these load cases, failure is expected in the hypertrophic zone, columnation zone and ossification zone respectively. Also the loading rate, maturity of the physis and sex alter the zones and mechanism of failure. All these effects have not been taken into consideration in this work.

The uncertainties in data of mechanical properties, correct consideration of loading, material characterization and geometric modelling are a direct consequence of the fact that each individual is unique. Average values might not be representative of a large percentage of the cases of interest. Therefore a more flexible and easily adjustable model to make approximate subject-specific analyses could be helpful when studying each specific individual. The parametrised geometry of the proximal femur in combination with FE is, despite the simplifications made in the geometry, suitable for the assessment of magnitudes of stress under mechanical loads for subject-specific geometries, so it can be used to determine the risk of SCFE development in different individuals, and help to a very important early diagnosis and a successful outcome [29].

## ACKNOWLEDGMENTS

The authors gratefully acknowledge the research support of the Spanish Ministry of Science and Technology through the research project DPI2006-09692 and the financial support by IBERCAJA.

## REFERENCES

- [1] R. T. Loder, *Slipped capital femoral epiphysis*, *Am Fam Physician* 57(9) (1998) 2135-42.
- [2] S. T. Canale, *Campbell's Operative Orthopaedics*, 2003, pp. 1481-1503.
- [3] R. T. Loder, *The demographics of slipped capital femoral epiphysis. an international multicenter study.*, *Clin Orthop Relat Res.* 322 (1996) 8-27.
- [4] J. G. Kennedy, M. T. Hresko, J. R. Kasser, K. B. Shrock, D. Zurakowski, P. M. Waters, M. B. Millis, *Osteonecrosis of the femoral head associated with slipped capital femoral epiphysis*, *J Pediatr Orthop* 21(2) (2001) 189-193.
- [5] R. T. Loder, B. Wittenberg, G. DeSilva, *Slipped capital femoral epiphysis associated with endocrine disorders*, *J Pediatr Orthop* 15(3) (1995) 349-356.
- [6] R. T. Loder, R. N. Hensinger, P. D. Alburger, D. D. Aronsson, J. H. Beaty, D. R. Roy, R. P. Stanton, R. Turker, *Slipped capital femoral epiphysis associated with radiation therapy*, *J Pediatr Orthop* 18(5) (1998) 630-636.
- [7] E. M. Manoff, M. B. Banffy, J. J. Winell, *Relationship between body mass index and slipped capital femoral epiphysis*, *J. Pediatr Orthop* 25(6) (2005) 744-746.
- [8] C. Barrios, M. A. Blasco, M. C. Blasco, J. Gascó, *Posterior sloping angle of the capital femoral physis. a predictor of bilatery in slipped capital femoral epiphysis.*, *J. Pediatr. Orthop.* 25(4) (2005) 1067-1078.

- 
- [9] J. W. Pritchett, K. D. Perdue, G. Dona, *The neck shaft-plate shaft angle in slipped capital femoral epiphysis*, *Orthop. Rev.* 18(11) (1989) 1187-1192.
- [10] J. L. Williams, P. D. Do, J. D. Eick, T. L. Schmidt, *Tensile properties of the physis vary with anatomic location, thickness, strain rate and age*, *J. Orthop. Res.* 19 (2001) 1043-1048.
- [11] J. L. Williams, J. N. Vani, J. D. Eick, E. C. Petersen, T. L. Schmidt, *Shear strength of the physis varies with anatomic location and is a function of modulus, inclination and thickness*, *J. Orthop. Res.* 17 (1999) 214-222.
- [12] Z. Fishkin, D. G. Armstrong, H. Shah, A. Patra, W. M. Mihalko, *Proximal femoral physis shear in slipped capital femoral epiphysis-a finite element study*, *J. Pediatr. Orthop.* 26(3) (2006) 291-294.
- [13] O. Paseta, M. J. Gómez-Benito, J. M. García-Aznar, C. Barrios, J. Gascó, M. Doblaré, *Biomechanical analysis of a slipped capital femoral epiphysis*, *Medical Engineering and Physics* (submitted).
- [14] CATIA, *Version 5, release 11 online documentation*, Dassault Systems, 1994-2003.
- [15] Harpoon, *Version 2.0*, cei.
- [16] D. D. Cody, G. J. Gross, F. J. Hou, H. J. Spencer, S. A. Goldstein, D. P. Pyhrie, *Femoral strength is better predicted by finite element models than QCT and DXA*, *J. Biomech.* 32 (1999) 1013-1020.
- [17] W. C. Hayes, J. L. W. Swenson, D. J. Schurman, *Asymmetrix finite element analysis of the lateral tibial plateau*, *J. Biomech.* 11 (1978) 21-33.
- [18] F. G. Evans, *Mechanical Properties of Bone*, Charles C. Thomas, 1973.
- [19] R. L. Spilker, J. K. Suh, V. C. Mow, *A finite element analysis of the indentation stress-relaxation response of linear biphasic articular cartilage.*, *J. Biomech. Eng.* 114(2) (1992) 191-201.
- [20] V. M. Goldberg, D. T. Davy, G. L. Kotzar, et al., *In Vivo Hip Forces*, New York, 1988, pp. 251-255.
- [21] S. M. Chung, S. C. Batterman, C. T. Brighton, *Shear strength of the human femoral capital epiphyseal plate*, *J. Bone Joint Surg. Am.* 58(1) (1976) 94-103.
- [22] J. W. Pritchett, K. D. Perdue, *Mechanical factors in slipped capital femoral epiphysis*, *J. Pediatr. Orthop.* 3 (1989) 385-388.
- [23] H. M. Litchman, J. Duffy, *Slipped capital femoral epiphysis: Factors shear forces on the epiphyseal plate*, *J. Pediatr. Orthop.* 4 (1984) 745-748.
- [24] J. Kordelle, M. Millis, F. A. Jolesz, R. Kikinis, J. A. Richolt, *Three-dimensional analysis of the proximal femur in patients with slipped capital femoral epiphysis based on computed tomography*, *J. Pediatr. Orthop.* 21(2) (2001) 179-182.
- [25] B. Cohen, G. S. Chorney, D. P. Phillips, H. M. Dick, J. A. Buckwalter, A. Ratcliffe, V. C. Mow, *The microstructural tensile properties and biochemical composition of the bovine distal femoral growth plate*, *J. Orthop. Res.* 10(2) (1992) 263-275.
- [26] S. Kumaresan, N. Yoganandan, F. A. Pintar, D. J. Maiman, *Biomechanical study of pediatric human cervical spine: A finite element approach*, *J. Biomech. Eng.* 122(1) (2000) 60-71.
- [27] K. M. Song, S. Halliday, C. Reilly, W. Kezsel, *Gait abnormalities following slipped capital femoral epiphysis*. 24(2) (2004) 148-155.
- [28] C. T. Moen, R. R. Pelker, *Biomechanical and histological correlations in growth plate failure*, *J. Pediatr. Orthop.* 4(2) (1984) 180-184.
- [29] T. Odent, S. Pannier, C. Glorion, *Epifisiólisis femoral superior*, *Enciclopedia médico-quirúrgica* 14 (2006) 396-401.

---

# A Framework for 3D Reconstruction of Human Organs from MR Images: A Model and Fuzzy Set Principles Based Approach. Application to Prostate Segmentation and Reconstruction

**Betrouni N.1 & Vermandel M.1**

1Inserm, U703, Medical Technology Institute, CHRU Lille, France. Faculty of Medicine, University of Lille II, UPRES EA 1049, Lille, France.

## **ABSTRACT**

*In this work we present a method for automatic 3D segmentation of prostate on MR images and volume reconstruction by fuzzy sets fusion algorithm. The segmentation is model based method and the reconstruction takes into account the slice thickness to reduce the partial volume effect. The tool is applied for prostate segmentation in radiotherapy planning.*

**Keywords :** 3D segmentation, deformable model, Fuzzy sets reconstruction, Prostate, MRI

## **I. INTRODUCTION**

3D segmentation and reconstruction is a difficult process because they must take into account the different deformations which characterize the object to be segmented. In the medical field, manual body delineation is a time consuming task and often requires prior knowledge to cope absence of contours due to the lack of contrast of images as well as the great variability of body shapes and positions.

For these reasons, researches in this field were directed towards methods which combine image information and a priori knowledge about the structure of the studied object. These methods are an extension of active contours ([1], [2]) and can be classified in two classes:

*Methods with a priori knowledge on the geometry:* The first work was that of [3] and its 3D extension in [4], [5] and [6] and m-reps multiscale description introduced by [7].

*Methods with a priori knowledge on appearance:* In this category, in addition of information about the geometry of the object, information on its appearance, in particular gray levels and textures are included [8] and [9] where knowledge about the probabilities densities of the pixels inside the form is added.

In many medical fields, the needs for segmentation are very important. In this paper, we propose a general framework for 3D reconstruction of human organs from MRI. This framework is described here through the process of prostate segmentation and reconstruction for prostate cancer diagnosis and image-guided therapy planning. Because automatic prostate segmentation remains complicated-in particular at apex either from transrectal ultrasound images (used for brachytherapy) or from MRI or CT (used for radiotherapy)-it seems to be an appropriate field of application of our approach.

This article is presented as follow: first, we shortly present the context of prostate segmentation for radiotherapy planning, then we detail the model-based approach and the fuzzy set principles method used for reconstruction.

## **II. CONTEXT**

---

For image guided therapy, some solutions appeared and especially to be applied in clinical practice. In [10], the authors proposed a method to segment the bladder, the rectum and the femoral heads on CT images. The method is based on a 3D model and user interaction to correct erroneous contour. Deformable image registration is a technique used in prostate segmentation in ([11], [12], [13], [14], [9]).

Considering the emerging role of MR imaging in radiotherapy treatment planning and the non-existence of a complete solution to assist the physician in target delineation i.e. prostate, we have designed an automatic segmentation tools based on a two steps framework. First, the prostate is automatically delineated using a deformable model algorithm. An implementation of the delineation algorithm was evaluated by comparing the results to manual segmentations made by a senior radiologist on images of 24 patients. Then, after the prostate is delineated, in order to perform a more realistic reconstruction and quantification of the prostate, we use a fuzzy set based algorithm [15]. This second step takes into account the partial volume effect and the MRI signal properties in a slice in order to obtain a volume closer to the physical one.

### III. METHODS

#### 3.1 Prostate Delineation with a Deformable Model

In a precedent report we have described a model based automatic prostate segmentation from ultrasound images combining an adaptive morphological filtering and a heuristic optimisation algorithm ([16]). We propose here an adaptation of this algorithm for 3D model-based segmentation of prostate on MR images. Prostate model was trained based on manual segmentations from  $N = 15$  patients MRI images that did not include the targets. According to the slice thickness and to its size and its shape, the prostate often appears on 8 to 12 slices in standard pelvic MR exam. In order to get a 3D model, the prostate was contoured, on each slice, by placing 20 points represented by their 3D coordinates  $pi = (xi, yi, zi)$ . Thus, the prostate surface was modelled by a vector  $X = [x0, y0, z0, x1, y1, z1 \dots, xP, yP, zP]$ , where P is the total number of surface points. For this study, whatever the number of slices used the total number of prostate points P was brought to 200.

Twenty points were used to describe each 2D contour as a compromise between the time spending and a detailed description of the contour variation. It should be underlined that this number of points is higher than the number of points usually laid out by the experts for delineating the prostate for radiotherapy purposes.

As the training set contained intra-patients data and the modelisation process was based on the variation of the positions of points over the set, it was important to align the points in the same way according to a set of axes. This alignment (rotation, translation and scaling) was achieved using the Iterative Closest Point (ICP) algorithm [17]. The ICP is based on an iterative alignment of the points through the minimization of a cost function which is the quadratic distance between the points. The method alternates pairing and calculation of the transformation between the paired points. Pairing is done by associating each point to its nearest neighbour

##### *(a) Extraction of statistical information*

Principal Component Analysis (PCA) enabled us to extract the model shape and the most important modes [3] of deformation. Model shape of the N-contours was computed as the mean  $x$  of the vectors components:

$$\bar{X} = \frac{1}{N} \sum_{i=1}^N X_i \quad (1)$$

Main variations around mean shape correspond to eigen values of the covariance matrix S:

$$S = \frac{1}{N-1} \sum_{i=1}^{i=N} dX_i \overline{dX_i} \quad (2)$$

wherein

$$dX_i = X_i - \bar{X} \quad (3)$$

is the displacement vector.

Each eigenvector is responsible for a variance equal to its eigen value. Its contribution to total shape variation can be expressed as:

$$\alpha_k = \frac{\lambda_k}{\sum_{i=1}^{3P} \lambda_i} \quad (4)$$

wherein  $\lambda_k$  and  $\phi_k$  represent eigen values and eigenvectors contribution to shape variance respectively. The method of determining the main modes of deformation consists in decomposing the displacement vector on an orthonormal base:

$$dX = \sum_{i=1}^{3P} b_i \theta_i \quad (5)$$

wherein  $\{\theta_i\}_{i=1..3P}$  are the base vectors and  $b_i$  represented the coordinates of vector  $dX$  in this base. This decomposition was carried out using the Karhunen–Loeve transform [18], which consists in decomposing a random vector according to the eigenvectors of its covariance matrix:

$$S\phi_i = \lambda_i \phi_i \quad (6)$$

wherein  $\lambda_i$  represents the normalized eigen values of the covariance matrix S and  $\phi_i$  its eigenvectors. These eigen values represent the variances of parameters  $b_i$ . An approximation of displacement vector  $dX$  was obtained through linear combination of  $m$  eigenvectors of covariance matrix S. These eigenvectors corresponded to the  $m$  most representative eigen values  $\lambda_i$  such as:

$$\sum_{i=1}^{i=m} \alpha_i \cong 1 \quad (7)$$

Thus a displacement vector can be expressed as:

$$dX \cong \sum_{i=1}^m b_i \phi_i \quad (8)$$

*b- Model*

Let  $\Phi = (\phi_1, \phi_2, \dots, \phi_m)$  the matrix composed by  $m$  most important eigenvectors of S, a vector  $X$  can

be expressed as:

$$X = \bar{X} + \phi b \quad (9)$$

wherein  $b = \{b_i\}$  is a  $R^m$  vector.

Assuming that the distribution of the  $b_i$  components is gaussian, all vector  $b$  component is included in  $[a, b]$  interval. Interval limits were used for restraining model deformation. Then, organ segmentation consists in finding the  $m$  deformation parameters  $b_i$  and the interval parameter  $a$ , that characterize its contour.

Figure 1 shows the 3D rendering of the prostate model.

### c- Contour searching

Contour searching was realised by optimising an energy function.

#### Contour energy

An energy defined by Terzopoulos et al. [2] is associated with each contour  $C$ :

$$E(C) = E_{\text{internal}} - E_{\text{external}} \quad (10)$$

The internal energy  $E_{\text{internal}}$  represents length and elasticity of the contour. The external energy  $E_{\text{external}}$  is

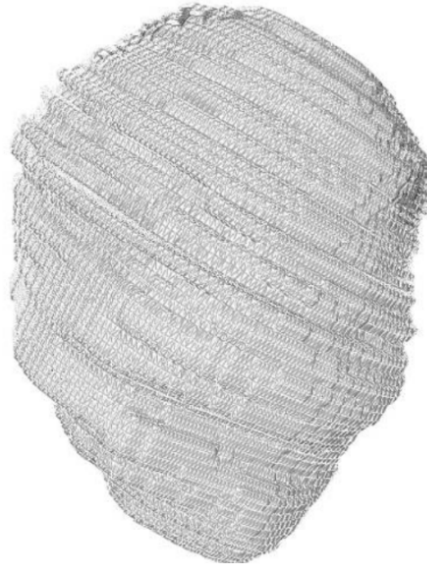


**Figure 1:** Prostate Model Rendering

associated with the image data. Its minimization tends the contour to recover the lines of steepest gradient. It's expressed as:

$$E_{\text{external}} = \int_a^b |\nabla |v(s)||^2 ds \quad (11)$$

wherein  $\nabla$  represents the image gradient calculated using the Deriche operator [19].

---

### Contour optimization

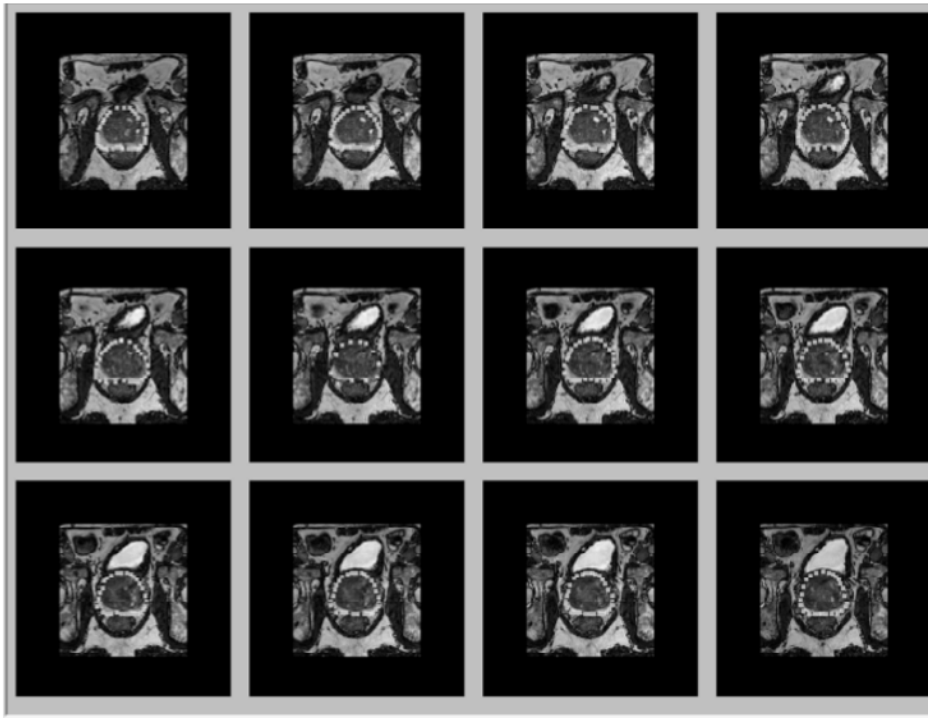
Segmentation began with interactive initialisation to position the model over the target in the image using axial and sagittal sequences. The second stage consisted in iteratively searching for the final contour. This search was performed by a simulated annealing algorithm known for its ability to explore a large range of parameters [20]. At each step, a new parameters  $b_i$  vector was randomly generated and introduced in Eq. (9) to form a new contour and compute its energy. If the visually assessed delineation accuracy was insufficient, the procedure was repeated until a visual match between the deformable prostate model and the organ was reached. These interactive corrections were only used in the areas of large mismatch, where the model was attracted to close structures.

Figure 2 shows an example of prostate automatic delineation.

### 3.2 Evaluation of Automatic Delineation

The delineation method was evaluated by comparing the results to manual segmentations performed by a senior physician involved in the management of prostate cancer. He operated on an images base of 24 patients with prostate cancer. Images were acquired on a 1.5 T Philips Intera® scanner with a phased array coil, with the following sequence parameters: a sagittal T2-w Turbo Spin Echo (TSE) (Field of view (FOV) = 24 cm x 24 cm, matrix 512 x 512, Time Repetition (TR)/Time Echo (TE) = 1630/110 ms, Echo Train Length (ETL) = 16, Slice Thickness (ST) = 4 mm) and a T1-w 3D Fast Field Echo (FFE) (FOV = 40 cm x 40 cm, matrix 512 x 512, TR/TE = 25/4.5 ms, ST = 5 mm) or a T1-w TSE SENSE (FOV = 40 cm x 40 cm, matrix 512 x 512, TR/TE = 499/12 ms, ETL = 5, ST = 5 mm).

The comparison between manual and automatic delineation was made on ARTIVIEW™ software



**Figure 2:** Example of Automatic Prostate Delineation on MR Images

(AQUILAB®SAS). This program identified the pixels located inside or outside a contour and assigned them a 0 or 1 value, respectively. The method was iterated for each slice of a given set of MR images. The following parameters were measured:

Volume Overlap (ratio of the volume of intersection to the volume of union, optimal value = 1)

$$VO = \frac{Vm \cap Va}{Vm \cup Va} \quad (12)$$

VO = volume overlap, Vm = manual volume, Va = automatic volume

It's important to stress that this index is very sensitive to small variations in overlap because it is normalized to the union of the volumes. As an example, if two equal volumes overlap by 85% of each, the volume overlap would be only 0.74.

Correctly delineated volume (percent ratio of the volume of intersection to the manual defined volume, optimal value = 100);

$$VC = \frac{Vm \cap Va}{Vm} \quad (13)$$

VC = correctly delineated volume.

### 3.3 Prostate 3D reconstruction

Once the volume was delineated, we performed a 3D reconstruction which takes into account the slice profile and the 3-D neighboring [15]. This algorithm, using fuzzy set tools, enabled to perform a more realistic reconstruction. This algorithm was previously validated for radiotherapy planning [15] and for cerebral vessels segmentation on MR images [21].

The aim was to define, for each slice, a minimum region within which was surely inside the structure (i.e. prostate in this application), and a maximum region which was surely outside this structure. A degree of membership equal to one (1) was, thus, assigned to the pixels inside the minimum volume, and a degree of membership equal to zero (0) was assigned to the pixels outside the maximum volume (figure 3). The degree of membership of the pixels in the intermediate area was obtained with the theory of possibility [22] using distribution functions taking into account:

- (1) the gray levels and the orientation of their local gradient in the image
- (2) the local CNR in the vicinity of the intermediate area

The degree of membership of a given pixel within the fuzzy area was determined in considering the distribution of the gray levels between the external and the internal border (figure 4). Thus, for a given pixel among the distribution, the gray level is converted to a degree of membership according to a distribution (triangular, trapezoidal, exponential, etc.) As proposed in [15], we used a sigmoid distribution given by:

$$\mu = \begin{cases} 1 & \text{if } Gl \geq Max \\ 1 - \frac{(Gl - Max)^2}{2 \cdot \alpha^2} & \text{if } Max \geq Gl \geq c \\ \frac{(Gl - Min)^2}{2 \cdot \alpha^2} & \text{if } c \geq Gl \geq Min \\ 0 & \text{if } Gl \leq Min \end{cases} \quad (14)$$

where:  $c = \frac{\text{Min} + \text{Max}}{2}$  and  $|\alpha| = |c - \text{Min}| = |c - \text{Max}|$ ,

GI is the gray level of a given pixel, Max and Min are the minimum and the maximum gray level among the distribution as shown figure. 6

Eq. 14 assigned to each pixel of each slice a degree of membership. In the case of a heterogeneous contrast around the structure, the pixel degree of membership of this structure should be greater in the higher-contrast area than in the lower-contrast area. Therefore, the membership distribution function has to be weighted as a function of contrast (Eq. 15). To do so, the CNR was calculated locally for each of the pixels belonging to the fuzziness region. This was achieved by calculating the local contrast along the structure boundary, taking a measurement of the noise in a local area, in the neighbourhood of the volume. The weighting function was then given by Eq. 15.

$$W_s = 1 - \exp(-\alpha \times \text{CNR}_s) \quad (15)$$

$$\mu' = W_s \times \mu$$

where  $W_s$  is the weighting factor according to the CNR in the area ( $\alpha$  is fixed at  $\text{Log}(100)/\text{CNR}_{\text{Max}}$  so that  $W_s = 0.99$  for the higher  $\text{CNR}_{\text{Max}}$  value observed in the whole set of MRA images) and  $\mu'$  is the weighted degree of membership.

To take into account the slice thickness and the volume partial effect, all the pixels from all the slices were considered

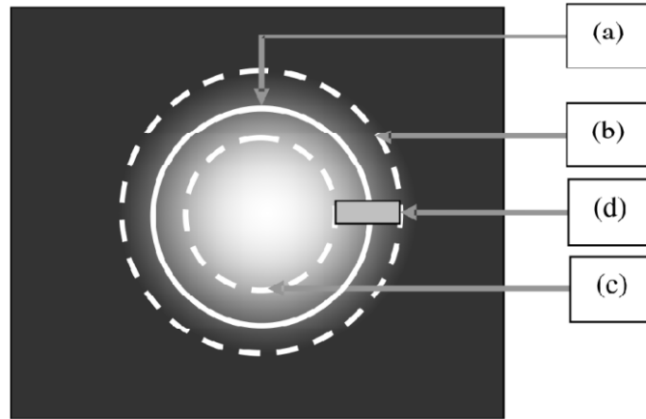


**Figure 3:** Definition of Fuzzy area Derived from the Initial Contour. (a) Initial Contour, (b) External Border of the Vascular Structure Obtained in Dilating (a) and Outside of which the Membership being Equal to 0. (c) Internal Border Obtained in Eroding (a) and Inside of which the degree of Membership being equal to 1. (d) Fuzzy Area.

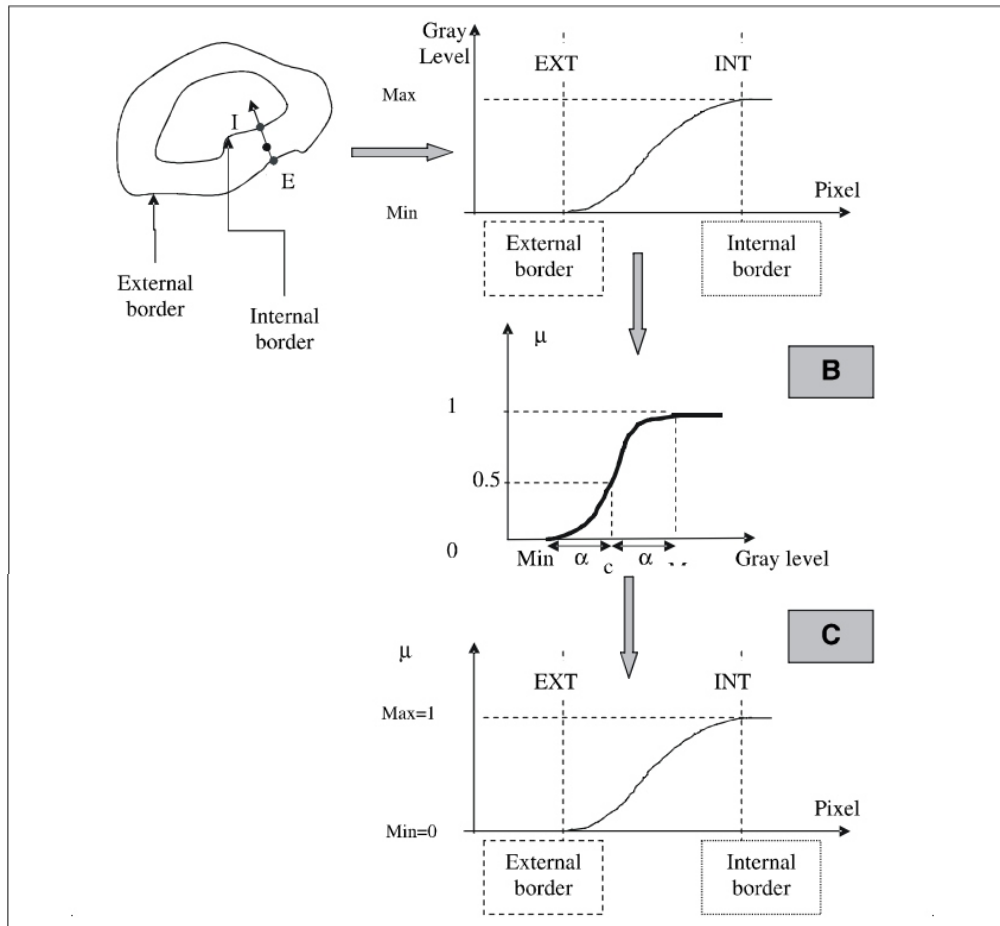


**Figure 4:** Computation of the Degree of Membership of the Pixels within the Fuzzy Area. For a given point of the External Border, the Gray Level Distribution is Measured (A) and is used to Convert the Pixels Gray Level into Degree of Membership ©. The Conversion from Gray Level to Degree of Membership is Achieved using a Sigmoid Function (B) (see Eq. 14). Note that in this Example, the Sigmoid Function is given for Dark Background and Bright Structure.

as voxels having a degree of membership to the structure. The first step in this 3-D process was the over-sampling of the volume according to the slice thickness (figure 5) and to take into account the slice profile of signal sensitivity (figure 6). This MR slice sensitivity profile was previously obtained by measurements taken on a phantom of known geometry [16].

Once this over-sampling performed, the degree of membership of each voxel  $\mu_n$ , obtained from Eq. 15, was attributed to all the sub-voxels, weighted by signal sensitivity distribution into the slice as well as by the simultaneous contribution of the neighbouring slices (figure 6). For the sub-voxel  $n$  belonging to the slice  $i$ , we finally obtained the degree of membership  $\mu_n$ :

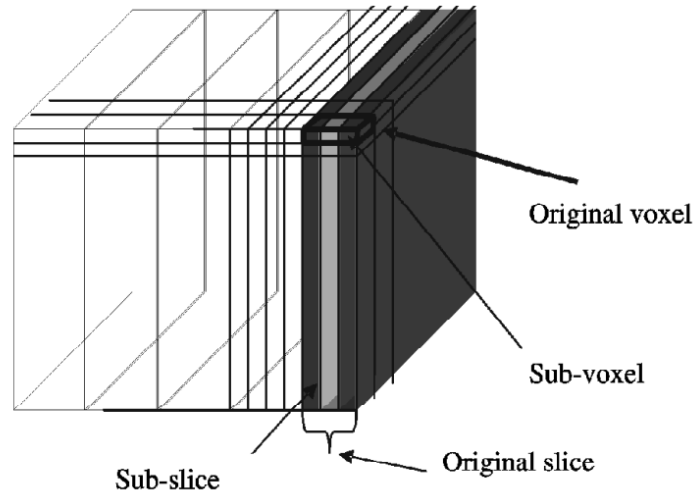


**Figure 5:** Over-sampling the Volume to Obtain Sub-voxels.

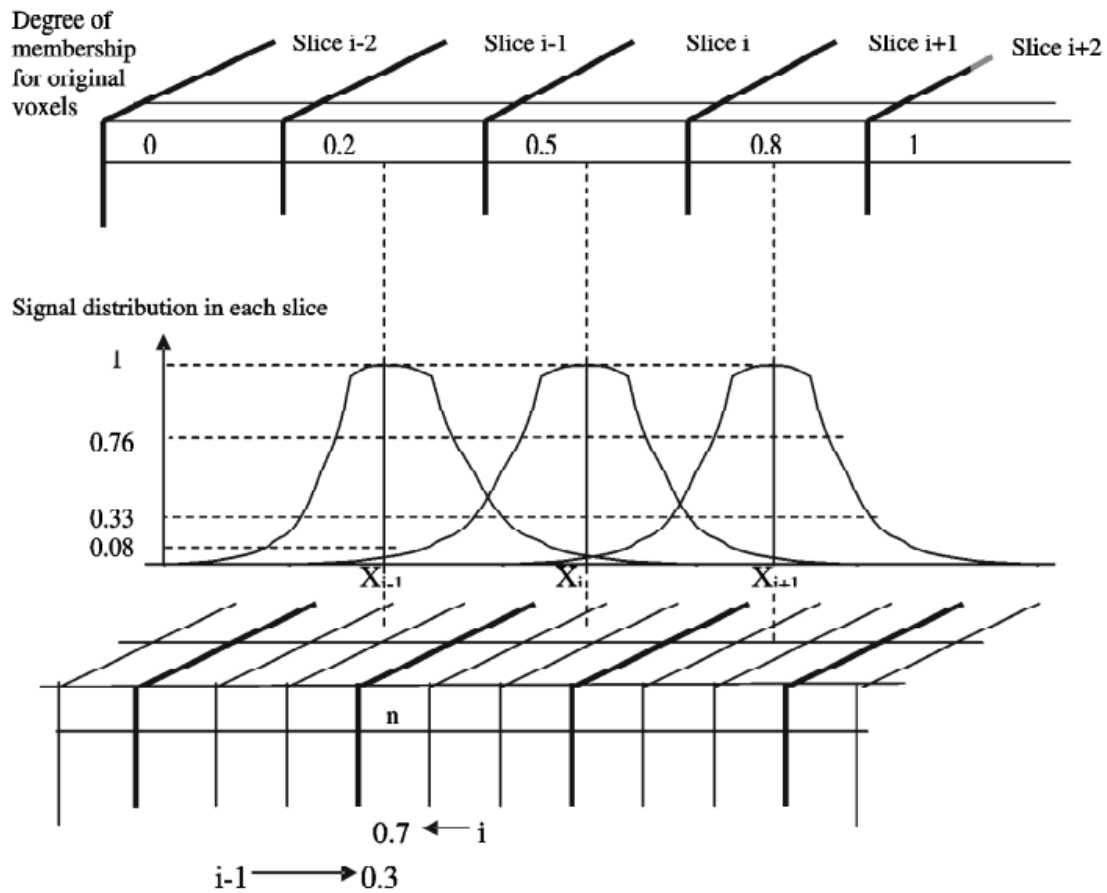


Figure 6: Signal distribution in the slices and contribution of contiguous slices to the calculation of membership for the sub-voxel in position  $n$ . Take, for example, 5 contiguous slices ( $i-2, i-1, i, i+1, i+2$ ) 4 mm thick, each of them being divided into 3 subslices. Let us also assume that, for the thickness of the slices in question, the distribution function of the signal is a gaussian function with a standard deviation of  $\sigma = 1.8$  mm. Numeric calculation on the basis of this gaussian function shows that the relative contribution of slice  $i$  to sub-voxel  $n$  is 0.76, and that of slice  $i-1$  is 0.33. The weighting factors are then  $w_{i,n} = 0.76 / (0.76 + 0.33) = 0.7$  and  $w_{i-1,n} = 0.33 / (0.76 + 0.33) = 0.3$ .

$$\mu_n'' = (\xi_{n,i} \cdot \mu_i' + \xi_{n,i-1} \cdot \mu_{i-1}' + \xi_{n,i+1} \cdot \mu_{i+1}') \quad (16)$$

where :  $\mu_i'$ ,  $\mu_{i-1}'$ ,  $\mu_{i+1}'$  are the degree of membership of the original voxels in the vicinity of the sub-voxel  $n$  and belonging to the slices  $i$ ,  $i-1$ ,  $i+1$ ;  $\xi_{n,i}$ ,  $\xi_{n,i-1}$ ,  $\xi_{n,i+1}$  are the weighting coefficients obtained from the signal slice profile of slices  $i$ ,  $i+1$ ,  $i-1$  in the sub-voxel  $n$  (figure 6).

Finally, using the marching cube algorithm [24], an iso surface was determined for visualization and quantification. This surface, which delineates the vascular structure from the background, was determined using a degree of membership threshold of 0.5. The choice of this value was justified by a previous study which has shown the robustness and the low variability of the segmentation results when using threshold value from 0.2 to 0.8 [15].

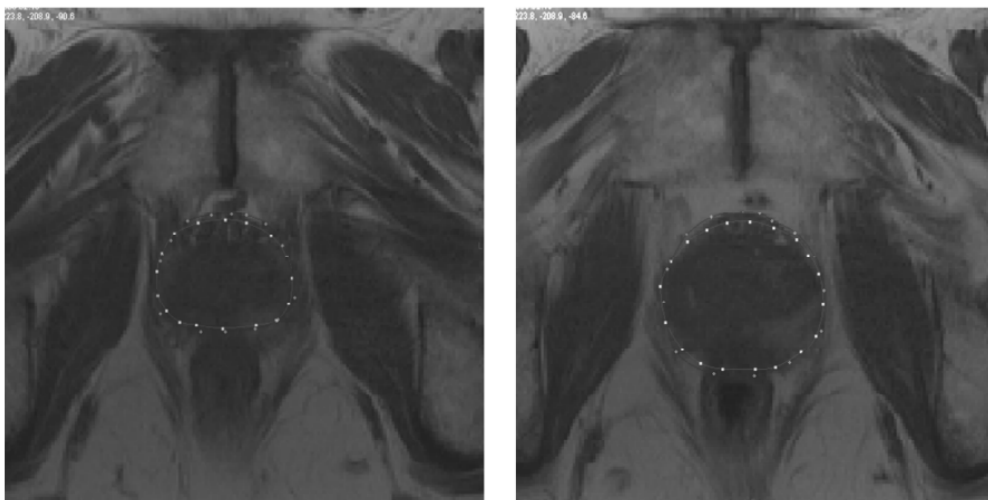
#### IV. RESULTS

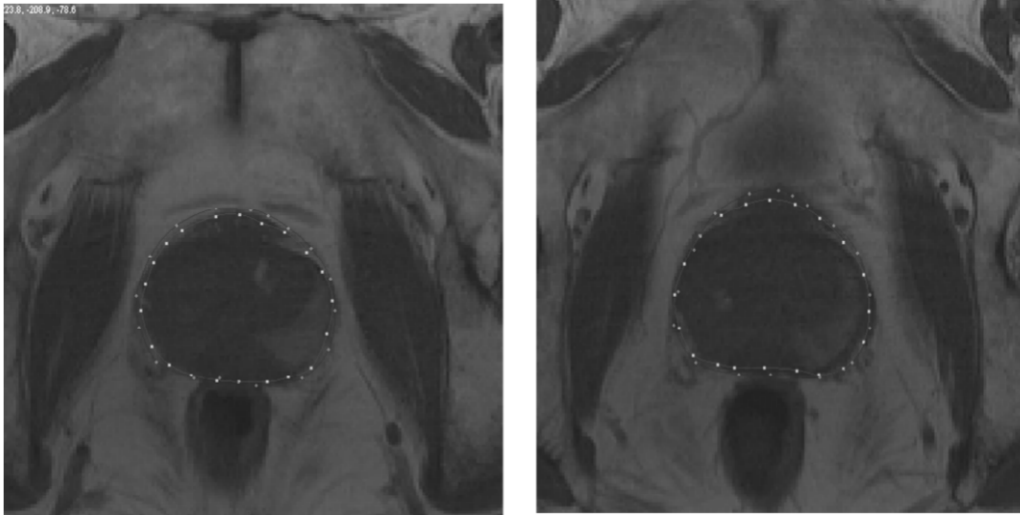
Volume ratio (VR) was  $1.130 \pm 0.09$ ; automatic volume is slightly larger than manual volumes (Wilcoxon test,  $p < 10^{-4}$ ). Volume Overlap (VO) and correctly delineated volume (VC) were  $0.784 \pm 0.05$  (min.: 0.71, max.: 0.86) and  $94.7 \pm 3.3$  (min: 0.89, max 0.99) respectively.

Figure 7 shows a comparison between manual and automatic segmentation for a patient. Figure 8 shows a volume rendered after delineation and reconstruction.

#### V. DISCUSSION

Different automated organ delineation methods have been studied in radiotherapy treatment planning. Automated 2D contouring aimed at robust detection of organ boundaries in 2D slices. Bueno et al. [25] have presented a 2D morphologic approach based on watershed transformation for automatic rectum, bladder and seminal vesicles segmentation. A good segmentation accuracy has been reported for the tested slices (1.2 to 1.7 mm average distance to ground truth for bladder and rectum respectively), but no validation of complete 3D data sets has been done. Mazonakis et al. [26] have proposed a region growing technique for the segmentation of prostate, bladder and rectum on CT images but a slider was used to define three independent threshold ranges and consequently this method cannot be considered as automatic. Lee et al. [27] have recently presented a semi-automatic segmentation of nasopharyngeal carcinoma in MR images. Concerning





**Figure 7:** Comparison between automatic prostate delineation and manual delineation by an expert

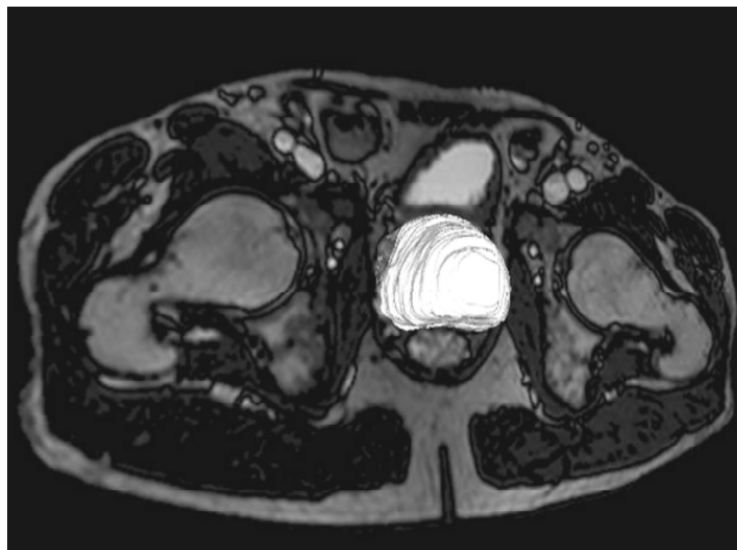


**Figure 8:** Final volume of the prostate

prostate automatic delineation most of the authors consider organ model based segmentation as a promising method but no detailed evaluation has been published to date. Pekar et al. [10] have proposed an automated model based organ at risk (rectum, bladder and femoral heads) delineation on TDM images. Reproducible and accurate results for automatic brainstem and kidney delineation have also been found with this model based method in Rao et al. [28] and Bondiau et al. [29]. Broadhurst et al. [30] in their method based on mreps [7] and statistical modelling of non-parametric histograms built a prostate and rectum models from 17 images of a single patient. Although the approach is interesting, it remains far from the practice since it is evaluated on the same data having been used to build the models. In Lu et al. and Foskey et al. [11, 12] the key idea is the use of the result of a deformable image registration to match two CT exams and automatically replace manual segmentation initially laid out on the reference image. The method provides good results for intra-patient exams but suffers of weakness for inter-patients exams because of the assumption of conservation of voxels values. Freedman et al. [9] combined a shape-appearance model and a probability distribution of photometric variables inside the

---

object to segment the prostate and the rectum. The authors reported major user interactions to correct the results.

Our study is one of the first to propose a truly 3D evaluation of an automated model based prostate delineation and consequently, our results are difficult to compare to others previous reports using a wide range of mainly 2D evaluation methods. Some authors have used the distances between the automatic and the manual contours (Hausdorff and radial distances). Also Pekar et al. [10] have compared automatic and manual rectum, bladder and femoral head contours; manual delineation was performed by a single observator. A good overall delineation accuracy (mean error 1.7 mm for bladder) was achieved but no 3D evaluation has been done. A 3D evaluation is also missed in Mazonakis et al. [26] where prostate, bladder and rectum volumes have been compared but on a slice-by-slice basis only. We have also to point out that a comparison based on volume index is more sensitive to small overlap differences than a comparison based on Hausdorff or radial distances. For example, two voxel cubes of  $10 \times 10 \times 10$  shifted by one voxel along the space diagonal direction results in only a 57 % volume overlap (729/1271) although the mean distance of surfaces is around one voxel. In the same way we compared radial distances and overlap volume in one patient after shifting the prostate volume by 5 voxels along the space diagonal direction in the axial plane, resulting in a maximal distance of 4 mm between automatic and manual volume: VO and VC were respectively 0.77 and 87%.

Manual segmentation is considered as the reference but cannot be considered as a perfect ground truth due to interobserver variability. Cazzaniga et al. [31] have assessed the variability between 6 physicians in defining the prostate on CT for three prostate tumour cases, the percentage differences between the measured volumes and the mean values ( $100 \times (\text{volume} - \text{mean volume}) / \text{mean volume}$ ) were ranged from 53.6 % to 60.5 %. Fiorino et al. [32] and Seddon et al. [33] have evaluated inter-observer difference in delineating prostate on CT between 5 and 15 physicians respectively. The variation in volume was estimated at 10% ( $\pm 18$ ) and 10 % ( $\pm 15$ ) respectively.

This variability has led Vial et al. [15] to propose a solution for reducing this variability while improving the volume quantification from manual delineation. This method has been applied on the automatic delineated structure because the contours obtained were closed to the expert ones. Indeed, even if the variability of the automatic delineation approach is lower than the manual way and more precise according to the image segmentation, the contours obtained did not necessary provide a good volume estimation due the inherent image partial volume effect what is corrected thanks to the reconstruction step of our framework.

Note that we do not discuss about the evaluation of this fuzzy approach because it has been already validated earlier [15,21].

## V. CONCLUSION

We have developed and evaluated a new MR images anatomy automatic delineation tool based on a deformable model and a fuzzy set approach for volume quantification. We have found good accuracy but also robustness of our algorithms on a 24 prostate cancer cases evaluation study. However automatic delineation could be compared to contours made by a panel of experts to definitely confirm its robustness and reproducibility. To our knowledge, our study is one of the first 3D evaluation of an automated model based prostate delineation. Software developments are ongoing to further reduce the process time calculation allowing a daily routine use. It is probably of importance to evaluate the influence of this new automated delineation on inter-observer delineation variability and dosimetry.

Whatever segmentation technique used (manual, automatic or semi-automatic), the ultimate gold standard is, and will remain, the clinical expert's eye. The goal of the automated procedures is to relieve as much as possible the physician of time consuming tasks while assuring accuracy and reproducibility

---

at least as high as manual method.

However there is also some other parameters to take into account as the national or international regulation as well as the software conformance to the professional recommendations. Collaboration with expert committees and industrial partners that respect the standards in use could contribute to the validation and a larger spreading of these techniques.

## REFERENCES

- [1] Kass M. Witkin A. Terzopoulos D. Snakes: Active contour models. *Int. J. Comput. Vis.* 1(4): 321-331. 1988.
- [2] Terzopoulos D. Platt J. Barr A. Fleischer K. Elastically deformable models. *Computer Graphics* 21(4): 205-214. 1987.
- [3] Cootes T. F. Hill A. Taylor C. J. Haslam J. The use of Active Shape Models for locating structures in Medical Images. *Image Vision and Computing* 12(6): 355-366. 1994.
- [4] Staib Lawrence H. Duncan James S. Model-based deformable surface finding for medical images. *IEEE Trans. Med. Imag* 15(5): 720-731. 1996.
- [5] Shen D. Davatzikos C. An adaptive-focus deformable model using statistical and geometric information. *IEEE Trans. Pattern Anal. Machine Intell.* 22(8): 906-913. 2000.
- [6] Tsai A. Yezzi A. Wells W. Tempanu C. Tucker D. Fan A. Grimson E. Willsky A. A shape based approach to curve evolution for segmentation of medical imagery. *IEEE Trans. Med. Imag* 22(2): 137-154. 2003.
- [7] Pizer Stephen M. Fletcher Thomas P. Sarang Joshi Gash Graham A. Stough J. Thall A. Tracton G. Chaney Edward L. A method and software for segmentation of anatomic object ensembles by deformable m-reps. *Medical Physics* 32(5): 1335-1345. 2005.
- [8] Cootes T. F. Taylor C. J. Statistical models of appearance for medical image analysis and computer vision. 4322 (*Proc. SPIE Medical Imaging*), 236-248. 2001. San Diego, CA.
- [9] Freedman D. Radke Richard J. Zhang Tao Yongwon Jeong Lovelock M. Chen George T. Y. Model-based segmentation of medical imagery by matching distributions. *IEEE Trans. Med. Imag.* 24(3): 281-292. 2005.
- [10] Pekar V, McNutt Todd R, and Kaus Micheal. Automated model based organ delineation for radiotherapy planning in prostatic region. *Int. J. Radiat. Oncol. Biol. Phys.* 60(3): 973-980. 2004.
- [11] Lu W., Chen M. L., Olivera G. O., Ruchala K. J., Mackie T. R. Fast free-form deformable registration via calculus of variations. *Phys. Med. Biol.* 49:3067-3087. 2004.
- [12] Foskey M., Davis B., Goyal L., Chang S., Chaney E., Strehl N., Tomei S., Rosenman, Joshi S. Large deformation threedimensional image registration in image-guided radiation therapy. *Phys. Med. Biol.* 50: 5869-5892. 2005.
- [13] Mohan R., Zhang X., Wang H., Kang Y., Wang X., Liu H., Ang K., Kuban D., and Dong L. Use of deformed intensity distributions for on-line modification of image-guided IMRT to account for interfractional anatomic changes. *Int. J. Rad Oncol. Biol. Phys.* 61(4): 1258-1266. 2005
- [14] Wang H., Dong l, Lii M., Lee A., De Crevoisier R., Mohan R., Cox J., Kuban D., and Cheung R. Implementation and validation of a three-dimensional deformable registration algorithm for targeted prostate cancer radiotherapy, *Int. J. Rad Oncol. Biol. Phys.* 61: 7.
- [15] Vial S., Gibon D., Vasseur C., Rousseau J. Volume delineation by fusion of fuzzy sets obtained from multiplanar tomographic images. *IEEE Trans. Med. Imaging* 2001; 20: 1362-1372.25- 735, 2005.
- [16] Betrouni N. Vermandel M. Pasquier D. Maouche S. Rousseau J. Segmentation of abdominal ultrasound images of the prostate using a priori information and an adapted noise filter. *Computerized Medical Imaging and Graphics* 29(1): 43-51. 2005.

- 
- [17] Besl P. J. N. D. McKay. *A Method for Registration of 3-D Shapes*. *IEEE Transactions on Pattern Analysis and Matching Intelligence* 14(2): 239-256. 1992.
- [18] Helstrom C. W. *Statistical Theory of Signal Detection*. 1968.
- [19] Deriche R. *Using Canny's Criteria to Derive a Resursively Implemented Optimal Edge Detector*. *International Journal of Computer Vision* 1(2): 167-187. 1987.
- [20] Kirkpatrick S. Gelatt CD. Vecchi MP. *Optimization by simulated Annealing*. *Science* 220, 671-680. 1983.
- [21] Vermandel M, Betrouni N., Taschner C., Vasseur C., Rousseau J. *From MIP image to MRA segmentation using fuzzy set theory*. *Comput Med Imaging Graphics (In Press)*. 2007.
- [22] Dubois D. *Combination of information in the framework of possibility theory*. New York: Abidi et al., *Data fusion in robotics and machine intelligence Academic*; 1992.
- [23] Bourel P. Gibon D. Coste E. Daanen V. Rousseau J. *Automatic quality assessment protocol for MRI equipment*. *Medical Physics*. 26: 2693-2700. 1999.
- [24] Bloomenthal J. *An Implicit Surface Polygonizer*. *Graphics Gems IV*. Morgan Kaufmann publ. Paul S. Heckbert ed. 1994. 324-350.
- [25] Bueno G., Fisher M., Burnham K., et al. *Automatic segmentation of clinical structures for RTP: Evaluation of a morphological approach*. In: *Proceedings of Medical Image Understanding and Analysis (MIUA '01)*. Birmingham, UK: BMVA Press: 36-73, 2001.
- [26] Mazonakis M., Damilakis J., Varveris H., et al. *Image segmentation in treatment planning for prostate cancer using the region growing technique*. *Br. J. Radiol* 74: 243-248, 2001.
- [27] Lee F. K., Yeung D. K., King A. D., et al. *Segmentation of nasopharyngeal carcinoma (NPC) in MR images*. *Int J. Radiat Oncol Biol. Phys.* 61: 608-620, 2005.
- [28] Rao M., Stough J., Chi Y. Y., et al. *Comparison of human and automatic segmentations of kidneys from CT images*. *Int J. Radiat Oncol Biol Phys*, 61: 954-960, 2005.
- [29] Bondiau P.Y., Malandain G., Chanalet S., et al. *Atlas-based automatic segmentation of MR images : validation study on the brainstem in radiotherapy context*. *Int J. Radiat Oncol Biol Phys.*, 61:289-298, 2005.
- [30] Broadhurst R.E., Stough J., Pizer S.M., and Chaney E.L., *Histogram Statistics of Local Model-Relative Image Regions*. in *International Workshop on Deep Structure, Singularities and Computer Vision (DSSCV)*, *Lecture Notes in Computer Science Vol. 3753*, of Olsen, L Florack, and A. Kuijper, eds: 71-82, (2005).
- [31] Cazzaniga LF, Marinoni MA, Bossi A, et al. *Interphysician variability in defining the planning target volume in the irradiation of prostate and seminal vesicles*. *Radio. Oncol.*, 47: 293-296, 1998.
- [32] Fiorino C, Reni M, Bolognesi A, et al. *Intra- and inter-observer variability in contouring prostate and seminal vesicles: implications for conformal treatment planning*. *Radio. Oncol.*,47(3): 285-292, 1998.
- [33] Seddon B, Bidmead M, Wilson J, et al. *Target volume definition in conformal radiotherapy for prostate cancer: quality assurance in the MRC RT-01 trial*. *Radio. Oncol.*, 56: 73-83, 2000.

---

---

# Material Properties and Extended Sources for Surface Rendering

Jan J. Koenderink & Sylvia C. Pont

Department of Physics and Astronomy, Universiteit Utrecht, The Netherlands

## ABSTRACT

*We consider generic BRDFs (Bidirectional Reflectance Distribution Functions) for rendering material surface properties. This is of importance in diverse graphics applications. Of various formal proposals found in the literature many are not plausible because they violate one or more physical constraints on BRDFs and of the plausible ones it is often unknown whether they are feasible, i.e., whether an exact physical model exists. Apart from the (default) Lambertian case, no analytical examples from the literature are conservative (i.e., remit all of the incident light). We investigate the simplest types of plausible BRDF that mimic the generic lobes commonly encountered in the daily environment: diffuse lobe (sand, paper, ...), specular lobe (smooth plastic, brushed metal, ...), backscatter lobe (rough plaster, lawn, ...) and asperity scattering lobe (velvet, hairy or dusty surfaces, ...). We propose novel methods to handle not just collimated, but also diffuse and ambient light beams for arbitrary surface rendering. These methods allow rendering of plausible “material properties” with no more overhead than the familiar “Lambertian surface illuminated by point source at infinity with ambient term”. The results are exact for convex objects, though only approximate in more complicated cases.*

**Keywords:** BRDF, material rendering, diffuse beams, extended sources, scientific visualization.

## INTRODUCTION

In scientific visualization one often uses “shading” to augment the visual impression of three-dimensionality of mere outline graphics [11]. In order to do so one has to simulate light sources and the way photons are bounced off the surfaces.

With “local rendering” we imply the determination of the radiance of the beam scattered towards the eye in the absence of such multilocal effects as cast shadowing and multiple scattering (reflexes). The most general case where local rendering is exact is that of arbitrarily illuminated convex objects. In this paper we restrict the radiation to beams due to sources at (effective) infinity, though this is not an essential constraint. The simplest implementation of the irradiating beam involves a “point source at infinity” and the simplest implementation of scattering the “Lambertian surface” [19,5]. More “realistic” implementations consider “extended sources” [29] and general BRDFs.

As is well known from photography, in order to suggest both shape and material properties one needs strategically placed extended sources and characteristic, non-Lambertian BRDFs [22]. This is awkward from the perspective of computer graphics implementation since standard graphics pipelines assume point sources and Lambertian surfaces. For “cheap rendering” the choice of suitable BRDFs and extended sources are critical in computer graphics.

## EXTENDED SOURCES

An “extended source” is fully described through the radiance of the incident beam [4]. Let  $\mathbf{n}$  denote the unit surface normal,  $\mathbf{i}$  the direction towards an infinitesimal element of the source,  $N_i(\mathbf{i})$  the radiance.

Then the irradiance  $H(\mathbf{n})$  of a surface element is

$$H(\mathbf{n}) = \int_{\mathbf{i} \cdot \mathbf{n} > 0} (\mathbf{i} \cdot \mathbf{n}) N_i(\mathbf{i}) d\mathbf{i},$$

where  $d\mathbf{i}$  denotes an infinitesimal vector solid angle in the direction of  $\mathbf{i}$ . The irradiance depends upon the spatial attitude of the surface element with respect to the incident beam through the “Lambert cosine Law” ( $\mathbf{i} \cdot \mathbf{n}$ ).

For the purposes of this paper we consider only three extreme types of incident beams, namely the collimated beam (often—rather awkwardly—called “point source at infinity”), the hemispherical diffuse beam with a total angular spread of  $2\pi$  steradians, and the Ganzfeld with a total angular spread of  $4\pi$  steradians. The collimated beam is a good model for direct sunlight (actual angular spread  $6 \times 10^{-5}$  steradians), the hemispherical diffuse beam for overcast sky (though we take the sky radiance as uniform instead of decreasing by about a factor of three from zenith to horizon), and the Ganzfeld for “ambient light” (a pure Ganzfeld exists only in circumstances like the “polar white-out”).

**Collimated beam** Consider a surface element with unit (outward) normal  $\mathbf{n}$ , irradiated from the direction (unit vector)  $\mathbf{i}$  and viewed from the direction (unit vector)  $\mathbf{j}$ . Let the normal irradiance caused by the incident beam be  $H_0$ , then the irradiance is  $H(\mathbf{i}, \mathbf{n}) = H_0 \mathbf{i} \cdot \mathbf{n}$  (by Lambert’s law). The radiance arriving at the eye is proportional with the irradiance, thus  $N(\mathbf{i}, \mathbf{j}, \mathbf{n}) = f(\mathbf{i}, \mathbf{j}, \mathbf{n}) H(\mathbf{i}, \mathbf{n})$ . Here the function  $f(\mathbf{i}, \mathbf{j}, \mathbf{n})$  is the “bidirectional reflectance distribution function (BRDF)”. Notice that  $\mathbf{i} \cdot \mathbf{n} \in [0, 1]$ , whereas  $\mathbf{i} \cdot \mathbf{n} < 0$  implies “body shadow”. (For an overview of recommended terminology see [1].)

**Hemispherical diffuse beam** Consider a surface that is irradiated with a hemispherical diffuse beam of radiance  $N(\mathbf{k}) = N_i$  for  $\mathbf{i} \cdot \mathbf{k} > 0$  and zero otherwise. The “direction” of the beam is  $\mathbf{i}$ . The radiance of the scattered beam is (notice that you may take  $\mathbf{i} \cdot \mathbf{n} \in [0, 1]$  here!):

$$N_j(\mathbf{i}, \mathbf{j}, \mathbf{n}) = \int_{(\mathbf{i} \cdot \mathbf{n} > 0) \wedge (\mathbf{i} \cdot \mathbf{k} > 0)} (\mathbf{k} \cdot \mathbf{n}) N_i(\mathbf{k}) f(\mathbf{k}, \mathbf{j}, \mathbf{n}) d\mathbf{k} = N_i g(\mathbf{i}, \mathbf{j}, \mathbf{n}).$$

The function  $g(\mathbf{i}, \mathbf{j}, \mathbf{n})$  sums up the effect of self-occultation (or “vignetting”) of the source, so it may be called the “Law of Vignetting”. For a white, Lambertian surface you obtain  $g(\mathbf{i}, \mathbf{j}, \mathbf{n}) = \mathbf{i} \cdot \mathbf{j} \mathbf{n} \cdot \mathbf{n}$ , thus the scattered radiance does not depend on the viewing direction  $\mathbf{j}$ . In the Lambertian case the result is reminiscent to the “point source at infinity with ambient light” formula. This is a mere accidental fact that applies only to the Lambertian case and does not generalize to general surfaces (vide infra).

**Fully diffuse beam: “Ganzfeld”** Since the incident radiance is independent of direction, the integrand depends only on the nature of the BRDF. One has

$$N_j(\mathbf{j}, \mathbf{n}) = N_i \int_{\mathbf{i} \cdot \mathbf{n} > 0} (\mathbf{i} \cdot \mathbf{n}) f(\mathbf{i}, \mathbf{j}, \mathbf{n}) d\mathbf{i} = N_i h(\mathbf{j}, \mathbf{n}).$$

Thus the scattered radiance depends only on the viewing direction  $\mathbf{j}$ . In analogy with the case of radiation seeping out of a translucent medium one might call  $h(\mathbf{j}, \mathbf{n})$  the “Law of Darkening” [7]. For a white Lambertian surface the law of darkening is  $hL = 1$ . Thus a white Lambertian surface becomes invisible in a Ganzfeld whereas a convex, gray Lambertian surface is rendered as a uniform silhouette. For general BRDFs the law of darkening is not constant and characteristic of the material though. Thus in general the contribution due to “ambient light” is not an additive constant as it is in the case of Lambertian surfaces. In order to render correctly one has to precompute the proper law of darkening for any material in the scene.

In general the case of diffuse beams is very complicated, since one has to perform a double integration

for each location. The use of a canonical beam, such as the hemispherical diffuse beam, allows one to use a function of three directions instead. This is convenient, since  $\mathbf{i}$ ,  $\mathbf{j}$  and  $\mathbf{n}$  are available in the graphics pipeline. Thus it really saves much computation to stick to canonical illuminations and analytical BRDFs.

Notice that the material (scattering) properties of a surface are conveniently summed up in terms of three functions, namely

- the “Law of Shading”  $f(\mathbf{I}, \mathbf{j}, \mathbf{n})$ ,
- the “Law of Vignetting”  $g(\mathbf{I}, \mathbf{j}, \mathbf{n})$ , and
- the “Law of Darkening”  $h(\mathbf{j}, \mathbf{n})$ .

A convenient measure of the “lightness” of a surface is the double diffuse reflectance, that is the fraction of a fully diffuse beam (Ganzfeld) scattered into any direction. One has

$$r = \frac{1}{\pi} \int_{\mathbf{j} \cdot \mathbf{n} > 0} \int_{\mathbf{i} \cdot \mathbf{n} > 0} (\mathbf{i} \cdot \mathbf{n})(\mathbf{j} \cdot \mathbf{n}) f(\mathbf{i}, \mathbf{j}, \mathbf{n}) d\mathbf{i} d\mathbf{j}.$$

For the Lambertian surface  $rL = 1$ , this surface is a perfect scatterer. For a surface that is not a perfect scatterer (“not conservative”) is it useful to define the “albedo” as the function  $a(\mathbf{i}, \mathbf{j}, \mathbf{n})$ . Because of “Helmholtz reciprocity” (see below) one has that  $a(\mathbf{i}, \mathbf{j}, \mathbf{n}) = a(\mathbf{j}, \mathbf{i}, \mathbf{n})$ . Apparently  $0 \leq a(\mathbf{i}, \mathbf{j}, \mathbf{n}) \leq 1$ . For the Lambertian white surface  $a(\mathbf{i}, \mathbf{j}, \mathbf{n}) = 1$ , in general  $a(\mathbf{i}, \mathbf{j}, \mathbf{n}) < 1$ , due to the requirement of conservation of radiant flux. For purposes of rendering in collimated and diffuse light fields surfaces are fully described through the functions  $f(\mathbf{i}, \mathbf{j}, \mathbf{n})$ ,  $g(\mathbf{i}, \mathbf{j}, \mathbf{n})$ ,  $h(\mathbf{j}, \mathbf{n})$ , whereas  $a(\mathbf{i}, \mathbf{j}, \mathbf{n})$  and  $r$  characterize overall reflecting properties. For the Lambertian surface you have the simple expressions  $f(\mathbf{i}, \mathbf{j}, \mathbf{n}) = \frac{1}{\pi} (\mathbf{i} \cdot \mathbf{n})(\mathbf{j} \cdot \mathbf{n})$ ,  $g(\mathbf{i}, \mathbf{j}, \mathbf{n}) = 1$  and  $h(\mathbf{j}, \mathbf{n}) = 1$  that are usually implemented in rendering pipelines (see figure 1). For more general surfaces these functions can be almost arbitrarily complicated. This is no problem in practice though since they may be precomputed and frozen in lookup tables.

## BRDFS

“Default” material properties are Lambertian [19], but often one prefers a “more realistic” type of surface material with a certain degree of gloss, etc. This introduces the problem of theoretical (analytic or algorithmic) surface scattering, typically handled via special BRDFs [1,25]. Often such BRDFs are chosen for computational convenience [11], rather than physical plausibility. Many shading algorithms in common use implement physically impossible surface scattering properties [2, 3, 27]. Attempts to replace these with physically realistic alternatives meet with perhaps unexpected problems. For instance, it is very hard to conceive of “interesting” (that is different from the default Lambertian) analytical expressions that would simulate physically admissible surface scattering properties and that are also conservative, i.e., that scatter all incident photons without absorbing any.

Notice that the Lambertian BRDF (the generic instance) is plausible in the sense that it does not violate known physical constraints (non-negativity, Helmholtz reciprocity and energy conservation, vide infra), but that it is unknown whether it is also feasible. A BRDF may be called “feasible” if there exists a model surface that yields that BRDF in terms of geometrical optics. (For examples [18,8, 33].) Although we can easily check BRDFs on plausibility, we can less easily check them on feasibility. Attempts to “explain” the Lambertian BRDF have been going on since the 18th century [5], but so far all have failed. The BRDFs known to be feasible have all started out as models (e.g., the perfect mirror, etc.) of particular physical surfaces [16,28], not as ad hoc postulated analytical expressions.

---

## General Properties of BRDFs

The BRDF is a property of a surface. It is clearly non-negative throughout. General arguments suggest that the BRDF is a symmetrical function in the directions of the entrance and exit beams, so called “Helmholtz reciprocity” [25, 21, 14, 18]. For a surface area  $A$  the incident radiant power is  $H(\mathbf{l}, \mathbf{n})A$ , whereas the total remitted radiant power is

$$\int_{(2\pi)} N(\mathbf{i}, \mathbf{j}, \mathbf{n}) d\epsilon = \int_{(2\pi)} N(\mathbf{i}, \mathbf{j}, \mathbf{n})(\mathbf{j} \cdot \mathbf{n}) A d\mathbf{j}.$$

Here  $d\epsilon$  is the element of étendue (or throughput), and  $d\mathbf{j}$  is an element of solid angle in the direction of  $\mathbf{j}$ . The symbol  $\int_{(2\pi)}$  denotes integration over the hemisphere  $\mathbf{j} \cdot \mathbf{n} \geq 0$ . Since the surface is assumed to (perhaps) absorb radiation, but emit none, conservation of energy requires that the “albedo”  $a(\mathbf{i}, \mathbf{n}) \leq 1$ . A “conservative” surface is a surface of “unit albedo”, that is one that remits all radiation falling upon it, irrespective the direction of the entrance beam. These exhaust all constraints on the BRDF that are listed in the literature:

$$f(\mathbf{i}, \mathbf{j}, \mathbf{n}) \geq 0 \quad \text{non-negativity} \quad (1)$$

$$f(\mathbf{i}, \mathbf{j}, \mathbf{n}) = f(\mathbf{j}, \mathbf{i}, \mathbf{n}) \quad \text{Helmholtz reciprocity} \quad (2)$$

$$a(\mathbf{i}, \mathbf{n}) \leq 1 \quad \text{“conservation of energy”} \quad (3)$$

Although there are several BRDFs in use that “conserve energy [20]” none of them has unit albedo except for the Lambertian case. In this paper we restrict the term “energy conservation” solely to the case of unit albedo. The final inequality is then simply a necessary condition for a BRDF to be counted as “plausible”.

A great many BRDFs in common use fail to be plausible [20]. Although this is known to violate basic radiometry such BRDFs are used because of algorithmic speed or ease of use in hardware graphics pipelines. Many users prefer speed over realism that they “can’t see”. Perhaps the most popular choices are the Phong [27] and the Blinn–Phong [2,3] BRDFs. Neither of these are plausible though because they violate Helmholtz reciprocity

## Generic, Simple, Analytic BRDFs

One can easily frame plausible BRDFs through simple analytic expressions. Many are simple enough that they pose no problems of algorithmic speed or ease of implementation. We suggest useful examples below.

The major modes of surface scattering are bulk scattering, specular reflection, backscattering and asperity scattering. Together (and in various combinations) these account for most of the materials encountered in the daily human environment. Exceptions involve macroscopic or microscopic deterministic structure [34,35,36] (combed hair, opals, peacock feathers), we ignore these. The generic scattering modes give rise to more or less well defined “lobes” in the scattering indicatrix, often easily identified in empirically determined BRDFs.

**Bulk scattering** is due to photons that did enter the bulk of the material and emerge after multiple (sub-surface) scattering events [26, 7]. After such multiple scattering events all traces of the direction of incidence are wiped out. This results in a broad, diffuse lobe centered on  $\mathbf{n}$ . Almost any material shows some bulk scattering;

**Specular reflection** is due to Fresnel reflection at planar interfaces between materials of different refractive index [4,14]. Often the surface is only locally planar, but macroscopically or mesoscopically

“bumpy”. In such cases one observes a lobe that is roughly centered on  $\mathbf{k} \cdot \mathbf{n} \approx 2(\mathbf{i} \cdot \mathbf{n})$ , that is the direction of the mirror–reflected ray, but broadened due to the bumpiness [32,12]. The degree of broadening can vary enormously. In some cases (lemon– peel for instance) the lobe has stochastic structure due to sparse sampling of the bumpiness;

**Backscattering** is typical for rough surfaces [18]. The combined influence of cast shadowing and visual occlusion (both due to vignetting) makes that only illuminated parts of the surface are seen from the direction of incidence [31,22] (“heilighenschein”). One obtains a rather broad lobe centered on  $\mathbf{i}$ . This is why the full moon is so bright [13,22] (for that reason called “opposition effect”);

**Asperity scattering** is due [17,10] to a layer of asperities that cover the nominal surface like a thin “atmosphere”. Common examples are human skin or plant leaves covered with tiny hairs, the tips of which act as asperities. Dust or face powder has a similar effect. Synthetic examples include various types of velvet. Peaches are optically different from plums due to asperity scattering. One has a typically narrow lobe extended along the surface, orthogonal to  $\mathbf{n}$ .

Models of various complexity (and physical realism) can be framed for any of these modes. Usually one has insufficient knowledge concerning a surface to actually apply a full blown physical model though. There is a room for simple analytical expressions that manage to capture the essence of the major modes. One may regard them as “phenomenological models” since they not necessarily respect all kinds of physical constraints. We will only consider plausible models though. Since we require the BRDFs to be plausible, they have to be non–negative functions of the basic constituents:

$$f_{\star}(\mathbf{i}, \mathbf{j}, \mathbf{n}) = 1,$$

$$f_{\star}(\mathbf{i}, \mathbf{j}, \mathbf{n}) = \frac{1}{2}(1 + \mathbf{i} \cdot \mathbf{j}),$$

$$f_{\star}(\mathbf{i}, \mathbf{j}, \mathbf{n}) = \frac{1}{2}(\mathbf{i} + \mathbf{j}) \cdot \mathbf{n},$$

$$f_{\star}(\mathbf{i}, \mathbf{j}, \mathbf{n}) = ((\mathbf{i} \cdot \mathbf{n})(\mathbf{j} \cdot \mathbf{n})).$$

Notice that these parts are all in the range [0, 1], thus they are not to be considered BRDF’s as such. Since the parts satisfy Helmholtz reciprocity, any function of them will too. The scalar product  $\mathbf{i} \cdot \mathbf{j}$  captures the similarity between the directions of exit and incidence and thus allows one to capture the geometry of backscattering. Likewise, the product  $(\mathbf{i} + \mathbf{j}) \cdot \mathbf{n}$  allows one to capture the geometry of asperity scattering. In order to capture the characteristic properties of the “lobes” we only consider unimodal BRDFs.

All cases are illustrated in figure 1.

For typical materials the BRDF is multimodal and determined by a combination of bulk scattering (“diffuse reflectance”), specular reflectance (“gloss”), backscattering and asperity scattering [9]. Such combinations can be constructed by “partitive mixture of BRDFs”, that is to say

$$f(\mathbf{i}, \mathbf{j}, \mathbf{n}) = \frac{\sum_{k=1}^N \mu_k f_k(\mathbf{i}, \mathbf{j}, \mathbf{n})}{\sum_{k=1}^N \mu_k}.$$

One easily shows that such a mixture is non-negative throughout, conforms to Helmholtz reciprocity and does not violate energy conservation if this applies to the individual components. The method is well suited to be combined with a method suggested by Ngan et al. [24] for image driven BRDF selection.

### Bulk Scattering

The best known (and most frequently used) instance of bulk scattering is of course the Lambertian surface. There doesn't exist a physical model, so the Lambertian BRDF is a phenomenological model. It does not fit cases of actual diffuse scattering particularly well, especially in the cases of grazing directions of incidence or viewing [23,26]. In order to correct for this Minnaert [22] suggested the expression ("d" for "diffuse")

$$f_d(\mathbf{i}, \mathbf{j}, \mathbf{n}) = C_d ((\mathbf{i} \cdot \mathbf{n})(\mathbf{j} \cdot \mathbf{n}))^\xi, \text{ with } C_d = \frac{2 + \xi}{2\pi}.$$

The parameter  $\xi$  controls the degree of "edge darkening". The parameter  $\xi$  may take any positive values, but realistic values are in the range from zero to one. For  $\xi = 0$  the Minnaert BRDF turns into the Lambertian, a realistic value for use is  $\xi = 1$ . The value of the constant  $C_d$  has been chosen to be the maximum value that does not violate energy conservation. This simple but instructive case allows us to introduce some important notions. The Minnaert BRDF produces a lobe centered upon the surface normal, irrespective of the direction of the incident beam. The radiance in directions that graze the surface is zero. Thus an object rendered with a Minnaert BRDF will have a dark edge, different from the Lambertian case. The Law of Vignetting can be found analytically by straightforward integration, but is complicated, because expressed in terms of confluent hypergeometric functions [6]:

$$g_d(\mathbf{i}, \mathbf{j}, \mathbf{n}) = \frac{\Gamma(\frac{3+\xi}{2})}{\sqrt{\pi}\Gamma(1+\frac{\xi}{2})} (\mathbf{i} \cdot \mathbf{n})(\mathbf{j} \cdot \mathbf{n})^\xi {}_2F_1\left(\frac{1}{2}, -\frac{\xi}{2}, \frac{3}{2}, (\mathbf{i} \cdot \mathbf{n})^2\right),$$

for integer  $\xi$

$$g_d(\mathbf{i}, \mathbf{j}, \mathbf{n}) = \frac{\Gamma(\frac{3+\xi}{2})}{\xi\sqrt{\pi}\Gamma(\frac{\xi}{2})} (\mathbf{j} \cdot \mathbf{n})^\xi B_{(\mathbf{i} \cdot \mathbf{n})^2}\left(\frac{1}{2}, 1 + \frac{\xi}{2}\right),$$

where  $B_z$  denotes the incomplete beta-function. Simple expressions are obtained for small integer exponents, e.g., for  $\xi = 1$  one has:

$$g_d(\mathbf{i}, \mathbf{j}, \mathbf{n}) = \frac{\mathbf{j} \cdot \mathbf{n}}{\pi} \left( \pi - \arccos(\mathbf{i} \cdot \mathbf{n}) + \mathbf{i} \cdot \mathbf{n} \sqrt{1 - (\mathbf{i} \cdot \mathbf{n})^2} \right).$$

Thus it is indeed different from the Lambertian expression. In the case of the Lambertian BRDF the rendering function is equal to that for a "point source at infinity with ambient light", but we now see that this is fortuitous. The law of darkening can also be obtained in closed form, namely  $(\mathbf{j} \cdot \mathbf{n})^\xi \left( \pi - \arccos(\mathbf{i} \cdot \mathbf{n}) + \mathbf{i} \cdot \mathbf{n} \sqrt{1 - (\mathbf{i} \cdot \mathbf{n})^2} \right)$ . It depends on the value of the edge darkening parameter. (See figure 2) Apparently the Minnaert BRDF is not conservative, indeed the albedo for collimated illumination is  $\frac{2 + \xi}{2\pi}$  and  $\frac{2 + \xi}{2\pi} \int \mathbf{i} \cdot \mathbf{n} d\mathbf{i}$ . Since  $\frac{2 + \xi}{2\pi} < 1$  for  $\xi < 0$  the Minnaert surface does not scatter all photons, but absorbs some. The surface is as bright as the constraints allow, yet scatters less effectively than the Lambertian surface. The double diffuse reflectance is

## Specular reflection

A simple expression for a specular lobe is (“s” stands for “specular”):

$$f_s(k, \mathbf{i}, \mathbf{j}, \mathbf{n}) = C_s \left( \frac{1 + \mathbf{k} \cdot \mathbf{j}}{2} \right)^\alpha$$

$$= C_s \left( \frac{1}{2} + (\mathbf{i} \cdot \mathbf{n})(\mathbf{j} \cdot \mathbf{n}) - \frac{\mathbf{i} \cdot \mathbf{j}}{2} \right)^\alpha \text{ with } C_s(k) = \frac{(1 + \alpha)(2 + \alpha)}{2\pi(2\alpha + 2^{-\alpha})},$$

where we limit  $\alpha$  to positive integer values. The expression captures the mirror reflection in the simplest possible way. An expression due to Lewis [20] (known as “cosine lobe” illumination model) is very similar, but fails to be non-negative and when this is cured turns out to have a spurious lobe (due to the original negative part). The above expression is unimodal by design. Again, the normalization factor  $C_s$  has been chosen to be as large as is compatible with energy conservation. This BRDF has a single lobe in the direction of the reflected ray. The width of the lobe can be controlled through the parameter  $\alpha$ . Realistic values run from  $\alpha = 1$  (a dull gloss) to very high (looks more specular). The illustration is for  $\alpha = 8$ . Although the Law of Vignetting and the Law of Darkening can be obtained in terms of elementary functions for integer values of  $\alpha > 0$ , the resulting expressions contain so many terms that they are practically useless for realistic values of the parameter. It is a simple matter to precalculate a lookup table of course. The BRDF is not conservative, e.g., the albedo is  $\frac{5}{32}$  for  $\alpha = 1$ , and as  $\alpha \rightarrow \infty$

$$\frac{(24201945 + 33554432 \cos \theta + 9773400 \cos 2\theta - 415212 \cos 4\theta + 10728 \cos 6\theta - 45 \cos 8\theta)}{67125248},$$

for  $\alpha = 8$ , where  $\theta = \arccos(\mathbf{i} \cdot \mathbf{n})$ . A sphere in a Ganzfeld shows a dark edge. (See figure 3).

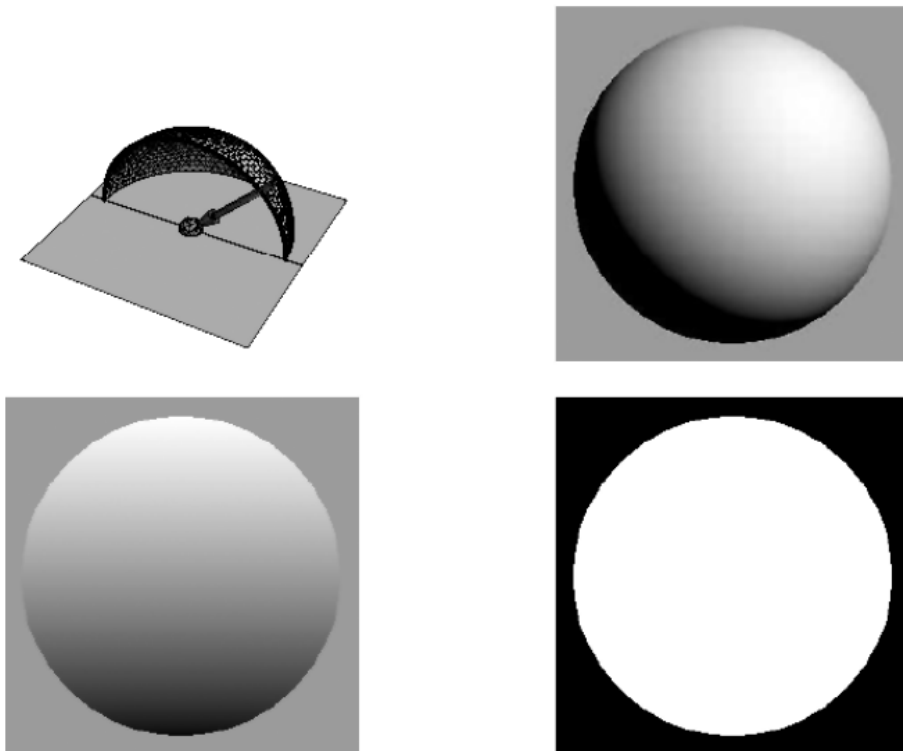


**Figure 1:** The Lambertian case. At top left a graphical rendering of the scattering indicatrix and right a rendering of a sphere illuminated with a collimated beam (at  $45^\circ$  from the viewing direction, from upper right—as indicated by the arrow). At bottom left a sphere illuminated with a hemispherical diffuse beam and right a sphere in a Ganzfeld.

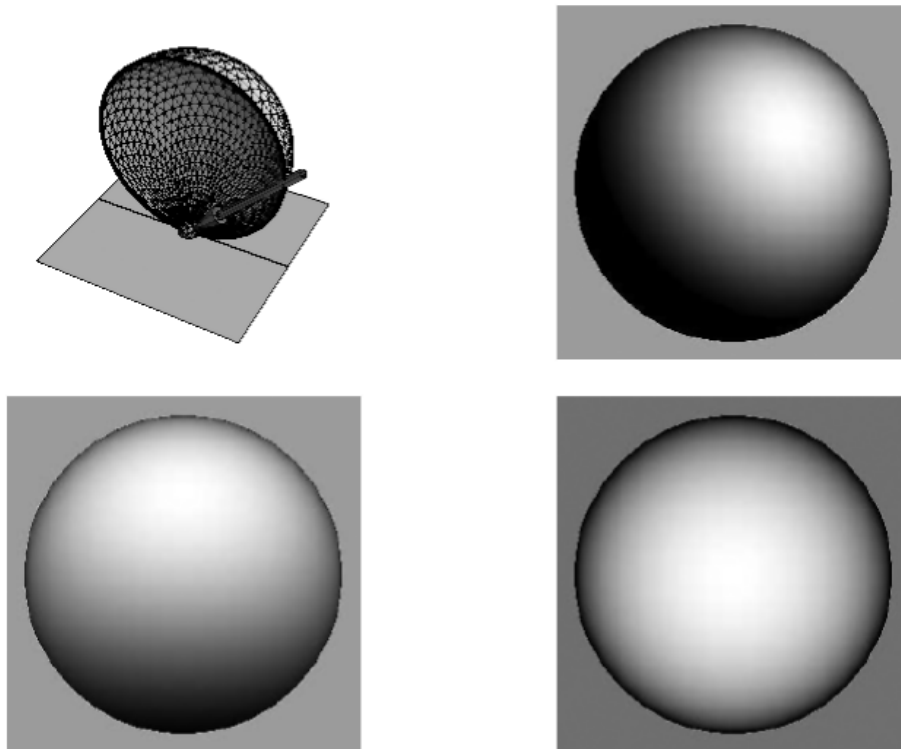


**Figure 2:** The Minnaert diffuse lobe for  $n = 1$ . At top left a graphical rendering of the scattering indicatrix and right a rendering of a sphere illuminated with a collimated beam (at  $45^\circ$  from the viewing direction, from upper right—as indicated by the arrow). At bottom left a sphere illuminated with a hemispherical diffuse beam and right a sphere in a Ganzfeld.

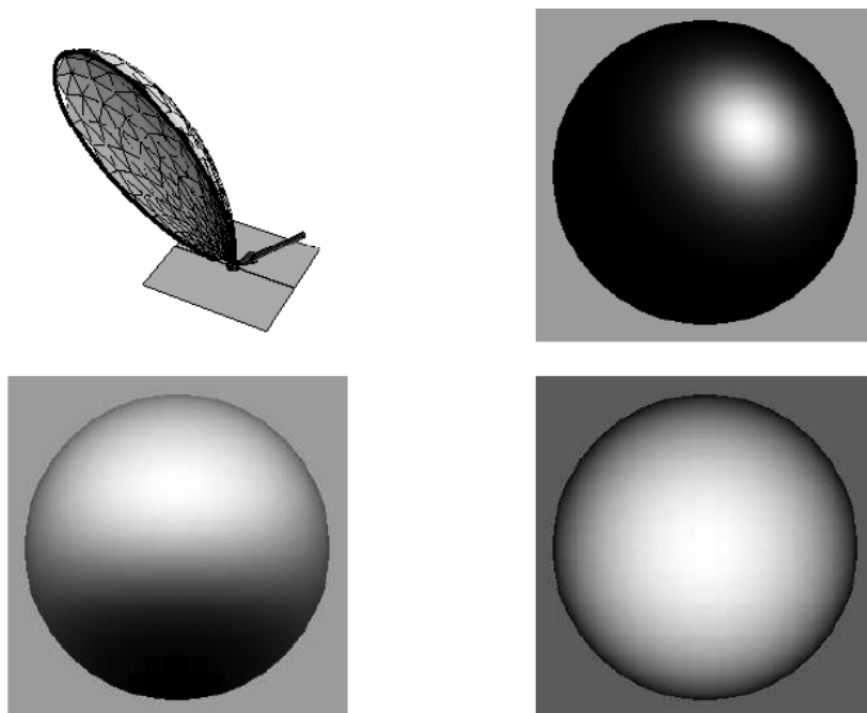


**Figure 3:** The specular lobe for  $\alpha = 8$ . At top left a graphical rendering of the scattering indicatrix and right a rendering of a sphere illuminated with a collimated beam (at  $45^\circ$  from the viewing direction, from upper right—as indicated by the arrow). At bottom left a sphere illuminated with a hemispherical diffuse beam and right a sphere in a Ganzfeld.

### Backscattering

Arguably the simplest expression that yields a true backscatter lobe is (“b” stands for “backscatter”):

$$f_b(k, \mathbf{i}, \mathbf{j}, \mathbf{n}) = C_b \left( \frac{1 + \mathbf{i} \cdot \mathbf{j}}{2} \right)^\alpha \text{ with } C_b = \frac{6}{5\pi 2^\alpha},$$

where the normalizing factor  $C_b$  has been chosen to maximize the reflectance. One easily checks that the scattered beam is unimodal, its width can be controlled through the parameter  $\alpha$ . The Law of Vignetting and the Law of Darkening can be obtained analytically for integer values of  $\alpha > 0$ . The resulting expressions are numerically useful for small values of  $\alpha$  (a realistic case). For instance, for  $\alpha = 1$  you have that

$$g_b(\mathbf{i}, \mathbf{j}, \mathbf{n}) = \frac{3}{10}(1 + \cos \theta) + \frac{1}{5\pi}(\cos \eta - \cos(\eta + 2\theta) + 2(\pi - \theta) \sin \eta \sin \zeta),$$

where  $\mathbf{i} \cdot \mathbf{n} = \cos \theta$ ,  $\mathbf{j} \cdot \mathbf{n} = \sin \theta \sin \eta \cos \zeta$  and  $[\ ] \cos \sin \mathbf{i} \cdot \mathbf{j} \cdot \mathbf{n} = \cos \theta \sin \eta \sin \zeta$ . For instance, for  $\alpha = 1$  the Law of Darkening is  $f_b(k, \mathbf{i}, \mathbf{j}, \mathbf{n}) = \frac{3}{10}(1 + \cos \theta) + \frac{1}{5\pi}(\cos \eta - \cos(\eta + 2\theta) + 2(\pi - \theta) \sin \eta \sin \zeta)$ . Thus the BRDF is not conservative, there is a slight edge darkening. (See figure 4).

Perhaps remarkably, it is possible to design a “perfect backscatterer”, that is a surface whose reflectance in the backscatter direction does not depend upon the direction of incidence. A sphere of such a material, when viewed from the direction of the incident beam (e.g., the full moon), appears like a featureless, uniform disk. A simple BRDF that achieves this is

$$f_{pb}(k, \mathbf{i}, \mathbf{j}, \mathbf{n}) = C_{pb} \frac{(1 + \mathbf{i} \cdot \mathbf{j})^\alpha}{(\mathbf{i} + \mathbf{j}) \cdot \mathbf{n}} \text{ with } C_{pb}(k) = \frac{1 + \alpha}{2^{1+\alpha} \pi}$$

for integer  $\alpha \geq 2$ . We do not know whether this is the only possible BRDF with this property.

### Asperity Scattering

A simple expression that yields a “surface lobe” typical of asperity scattering is (“a” stands for “asperity scattering”):

$$f_a(k, \mathbf{i}, \mathbf{j}, \mathbf{n}) = C_a (1 - (\mathbf{i} \cdot \mathbf{n})(\mathbf{j} \cdot \mathbf{n}))^\alpha \text{ with } C_a = \frac{1}{\pi}.$$

The normalizing factor  $C_a$  is as large as possible as is compatible with the plausibility constraints. The parameter  $\alpha$  should be larger than one. For high values of the parameter one has strong, velvet-like, asperity scattering. Notice that the expression is much like the “complementary” of the Minnaert BRDF. For any direction of incidence the radiance is highest (namely  $C_a$ ) in directions grazing the surface. The radiance falls off rapidly for less oblique rays. The parameter  $\alpha$  controls the “width” of the asperity scattering lobe. The Law of Vignetting and the Law of Darkening can be obtained analytically for integer values of  $\alpha > 0$ . For small values of  $\alpha$  one obtains useful expressions though.

---

For instance, for the realistic value  $\rho = 1$  one has

$$g_a(\mathbf{i}, \mathbf{j}, \mathbf{n}) = \frac{1 + \mathbf{i} \cdot \mathbf{n}}{2} - \frac{4\mathbf{j} \cdot \mathbf{n}}{3\pi} \left( \pi - \arccos(\mathbf{i} \cdot \mathbf{n}) + \mathbf{i} \cdot \mathbf{n} \sqrt{1 - (\mathbf{i} \cdot \mathbf{n})^2} \right) - \frac{1}{8} (\mathbf{j} \cdot \mathbf{n})^2 (\mathbf{i} \cdot \mathbf{n} - 2)(\mathbf{i} \cdot \mathbf{n} + 1)^2,$$

$$h_a(\mathbf{j}, \mathbf{n}) = 1 - \frac{2}{3} (\mathbf{j} \cdot \mathbf{n}).$$

The BRDF is not conservative. This material shows an edge lightening, as is typical for a material like velvet which shows strong asperity scattering. (See figure 5)

## CONCLUSIONS

The literature on ad hoc expressions for the bidirectional reflectance distribution function is rather muddled. Even today (mainly in the computer graphics community) BRDF expressions that fail on mere plausibility are in common use. Non-plausible BRDF expressions have become scarce in applied optics after Minnaert's work. As we have shown simple analytical expressions can be framed such that no physical constraints are violated and yet such that well known generic physical properties of common materials such as diffuse scattering, specular scattering (gloss), backscattering and asperity scattering are represented in a parameterized manner. One property that cannot so easily be accommodated is conservation of radiant power though.

The choice of a few canonical surfaces and a few canonical light fields as advocated here has the merit that it is easily integrated in existing graphics pipelines with almost negligible (as compared to the Lambertian assumption) overhead, yet without violating basic physical constraints.

This allows more realistic rendering to be done "on the cheap". The method is exact for convex objects, though only approximate for non-convex ones, precisely as with the standard default rendering. In general one will assign different colors to the various components, e.g., the diffuse component is due to the bulk material and will be assigned the "body color", the backscatter component is due to multiple scattering microcavities, thus will be assigned the body color at higher saturation level, whereas the specular and asperity components are due to directly scattered or Fresnel reflected radiation, thus will be assigned the color of the source [15, 30, 37].

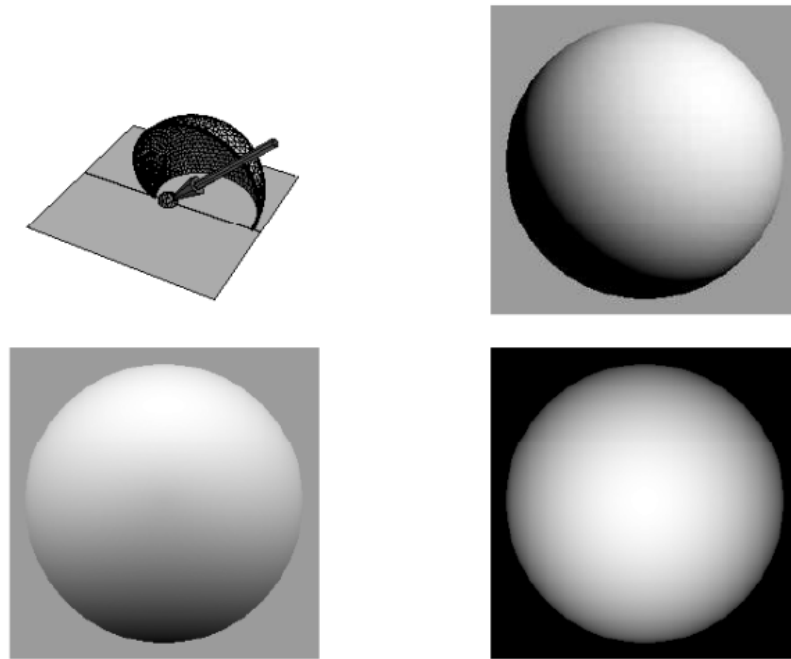


**Figure 4:** The backscatter lobe for  $\mu = 1$ . At top left a graphical rendering of the scattering indicatrix and right a rendering of a sphere illuminated with a collimated beam (at  $45^\circ$  from the viewing direction, from upper right—as indicated by the arrow). At bottom left a sphere illuminated with a hemispherical diffuse beam and right a sphere in a Ganzfeld.

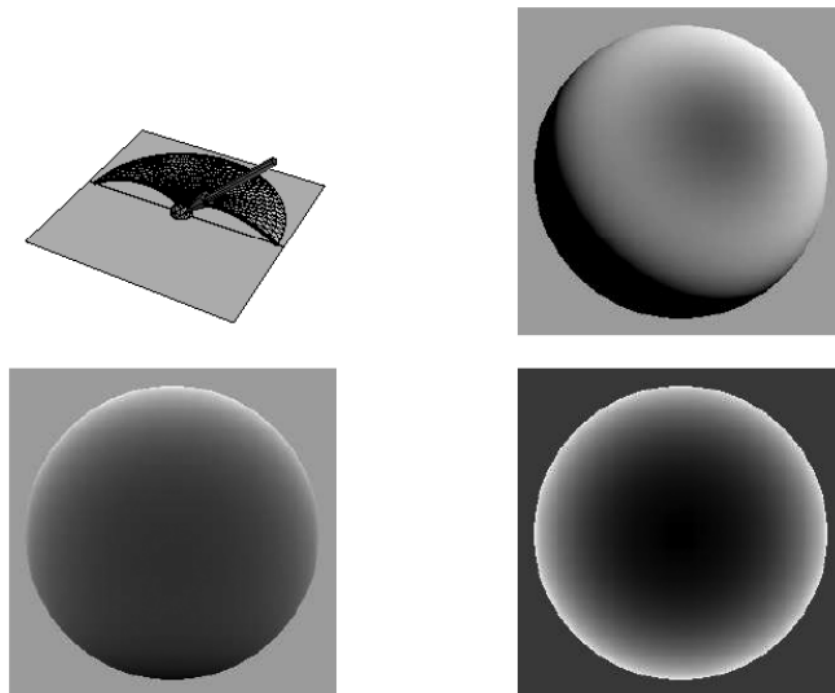


**Figure 5:** The asperity scattering lobe for  $\mu = 1$ . At top left a graphical rendering of the scattering indicatrix and right a rendering of a sphere illuminated with a collimated beam (at  $45^\circ$  from the viewing direction, from upper right—as indicated by the arrow). At bottom left a sphere illuminated with a hemispherical diffuse beam and right a sphere in a Ganzfeld.

---

## ACKNOWLEDGEMENTS

This work was sponsored via the European program Visiontrain contract number MRTNCT2004005439. Sylvia Pont was supported by the Netherlands Organisation for Scientific Research (NWO).

## REFERENCES

- [1] American National Standards Institute/Illuminating Engineering Society of North America, *Nomenclature and definitions for illuminating engineering, ansi/ies rp-16-1986 edition*, 1986.
- [2] Blinn, J. F. and Newell, M. E., *Texture and reflection in computer generated images*, *Communications of the ACM* 19, pp. 542–546, 1976.
- [3] Blinn, J. F. and Newell, M. E., *Models of light reflection for computer synthesized pictures*, *Computer Graphics (SIGGRAPH '77 Proceedings)* 11, pp. 192–198, 1977.
- [4] Born, M. and Wolf, E., *Principles of Optics*, Cambridge University Press, Cambridge, 1998.
- [5] Bouguer, P., *Traité d'optique sur la gradation de la lumière*, posthumous edition arranged by Nicolas Louis de la Caille, H. L. Guerin & L. F. Delatour, Paris, 1760.
- [6] Buchholz, H. *The Confluent Hypergeometric Function with Special Emphasis on its Applications*. Springer-Verlag, New York, 1969.
- [7] Chandrasekhar, S., *Radiative Transfer*, Dover Publications, Inc., New York, 1960.
- [8] Cook, R. L. and Torrance, K. E., *A reflection model for computer graphics*, *ACM Transactions on Graphics* 1, pp. 7–24, 1982.
- [9] Dana, K. J., Van-Ginneken, B., Nayar, S. K. and Koenderink, J. J., *Reflectance and Texture of Real World Surfaces*, *ACM Transactions on Graphics (TOG)*, 18, pp. 1–34, 1999.
- [10] Egan, W. G. and Hilgerman, T., *Spectral reflectance of particulate materials: a Monte Carlo model including asperity scattering*. *Applied Optics* 17, pp. 245–252, 1978.
- [11] Foley, J. D., Dam A. van, Feiner, S. K. and Hughes, J. F., *Computer graphics, Principles and Practice*, 2nd Ed., Addison-Wesley, Reading Massachusetts, 1990.
- [12] Ginneken, B. van, Stavridi, M. and Koenderink, J. J., *Diffuse and specular reflection from rough surfaces*, *Applied Optics* 37(1), pp. 130–139 1998.
- [13] Hapke, B., Nelson, R. and Smythe, W., *The opposition effect of the moon: coherent backscatter and shadow hiding*. *Icarus* 133, pp. 89–97, 1998.
- [14] Hecht, E., *Optics*, Addison-Wesley Publishing Company, Reading, Massachusetts, 2002.
- [15] Klinker, G. J., Shafer, S. A. and Kanade, T., *Using a color reflection model to separate highlights from object color*, in: *Proceedings of the First International Conference on Computer Vision*, Computer Society Press of the IEEE, Washington, pp. 145–150, 1987.
- [16] Koenderink, J. J., A. J. van Doorn, K. J. Dana, and S. Nayar, *Bidirectional Reflection Distribution Function of thoroughly pitted surfaces*, *International Journal of Computer Vision*, 31 (2/3), pp. 129–144, 1999.
- [17] Koenderink, J. J. and Pont, S. C., *The secret of velvety skin*, *Machine Vision and Applications; Special Issue on Human Modeling, Analysis and Synthesis*, 14, pp. 260–268, 2003.
- [18] Kortüm, G., *Reflexionsspektroskopie. Grundlagen, Methodik, Anwendungen*. Springer, Heidelberg, 1969.
- [19] Lambert, J. H., *Photometria, sive de Mensura et gradibus luminis, colorum et umbræ*, Eberhard Klett, Augsburg, 1760.
- [20] Lewis, R. R., *Making shaders more physically plausible*, In: *Fourth Eurographics Workshop on Rendering*, pp. 47–62, 1993.
- [21] Minnaert, M., *The reciprocity principle in lunar photometry*, *Astrophysical Journal* 93, pp.

---

403–410, 1941.

- [22] Minnaert, M., *The Nature of Light and Colour in the Open Air* Dover, New York, 1954.
- [23] Nayar, S. K. and Oren, M., *Visual appearance of matte surfaces*, *Science* 267, pp. 1153–1156, 1995.
- [24] Ngan, A., Durand, F. and Matusik, W., *Image-driven navigation of analytical BRDF models*, *Eurographics Symposium on Rendering 2006*, Eds., Akenine-Möller and Wolfgang Heidrich, 2006.
- [25] Nicodemus, F. E., Richmond, J. C., Hsia, J. J., Ginsberg, I. W. and Limperis, T., *Geometric considerations and nomenclature for reflectance*, *Natl. Bur. Stand. (U. S.) Monogr. 160 (U. S. Department of Commerce, Washington D. C.)*, 1977.
- [26] Oren, M. and Nayar, S. K., *Generalization of the Lambertian model and implications for machine vision*, *International Journal of Computer Vision* 14, pp. 227–251, 1995.
- [27] Phong, B. T., *Illumination for computer generated pictures*, *Communications of the ACM* 18, pp. 311–317, 1975.
- [28] Pont, S. C., and Koenderink, J. J. *BRDF of specular surfaces with hemispherical pits*, *Journal of the Optical Society of America A* 19, pp. 2456–2466, 2002.
- [29] Pomraning, G. C., *The Equations of Radiation Hydrodynamics*, Pergamon Press, Oxford, 1973.
- [30] Shafer, S. A., *Using color to separate reflection components*, " *Color Research Applications* 10, pp. 210–218, 1985.
- [31] Schlichting, H. J. and Uhlenbrock, M., *Der Heiligenschein als Naturer Scheinung*, *Physik in unserer Zeit*, 3, pp. 173–175, 1999.
- [32] Torrance, K. E. and Sparrow, E. M., *Theory of off-specular reflection from roughened surfaces*, *Journal of the Optical Society of America* 57, pp. 1105–1114, 1967.
- [33] Torrance, K. E., Sparrow, E. M. and Birkebak, R. C., *Polarization, directional distribution, and off-specular peak phenomena in light reflected from roughened surfaces*, *Journal of the Optical Society of America A* 56, pp. 916–925, 1966.
- [34] Vukosic, P., Sambles, J. R. and Lawrence, C. R., *Color mixing in wing scales of a butterfly*, *Nature* 404, p. 457, 2000.
- [35] Vukosic, P., Sambles, J. R., Lawrence, C. R. and Wakely, G., *Sculpted-multilayer optical effects in two species of Papilio butterfly*, *Applied Optics* 40, pp. 1116–1125, 2001.
- [36] Vukosic, P. and Sambles, J. R., *Photonic structures in biology*, *Nature* 424, pp. 852–855, 2003.
- [37] Wolff, L. B., *Relative brightness of specular and diffuse reflection*, ' *Optical Engineering* 33, pp. 285–293, 1994

---

---

# Computational Study on Bone Remodeling and Osseointegration for a Hip Replacement using a Conservative Femoral Stem

**J. Folgado\*, P. R. Fernandes and H. C. Rodrigues**

IDMEC–Instituto Superior Técnico, Technical University of Lisbon, Av. Rovisco Pais, 1049-001  
Lisboa, Portugal

## **ABSTRACT**

*In this work a computational model to simulate the osseointegration fixation of cementless femoral stems is described. This biological fixation and the bone remodeling are not independent. Thus this model combines the osseointegration analysis with a bone remodeling model. The osseointegration process is modeled based on the relative displacement between bone and stem as well as on the interface stress level, i.e., the osseointegration depends on the mechanical stability of the stem. The law of bone remodeling is derived from a material optimization problem, via the minimization of a function that takes into account structural stiffness and the metabolic cost related with bone mass maintenance. The problem is solved considering contact conditions on the interface between bone and implant. The model is used to analyze a conservative stem (Mayo, Zimmer Inc.) and to compare its performance with a tapered one (Trilock, Depuy Orthopaedics, Johnson&Johnson). These conservative stems require minimal bone removal, and are suitable to apply minimally invasive surgery techniques. However, the fixation and the stability of the stem is one aspect of major concern. The model developed in this paper allows us to investigate the performance of such stems with respect to stability and compare them with conventional stems.*

**Keywords: Biomechanics, Hip, Prosthesis, Stability, Osseointegration, Bone remodeling**

## **1. INTRODUCTION**

Nowadays, Total Hip Arthroplasty (THA) is one of the most important and common orthopedic procedures. This fact is related with population ageing and also with the development achieved in the medical technology.

The main reason for a THA is hip joint diseases such as primary osteoarthritis, but it is also a successful treatment in several other situations such as fracture repair [1]. The THA consists on the replacement of the natural hip joint by an artificial one. This artificial hip joint has two components, the acetabular cup and the femoral component. In a total hip arthroplasty, femoral head is removed and the stem component is inserted into the femoral canal removing a considerable amount of host bone (figure 1).

Recently the interest on conservative stem design for minimally invasive hip replacement surgery has been increased. These conservative stems are smaller than conventional ones, and require less bone removal thus leaving intact many elements of fixation, that would otherwise be lost in a traditional primary arthroplasty. However, one aspect of major concern with these stems is its fixation and stability.

Stem stability plays a decisive role in the success of a Total Hip Arthroplasty and thus in order to assure the long term stability, the cementless stems should be designed to promote biologic fixation, i.e., the bone attachment into the stem surface. This osseointegration (or bone ingrowth) is achieved coating the surface with hydroxyapatite (HA) or with a porous coating layer. However, even with such a special

coated surfaces, several factors can inhibit or destroy the biologic fixation. In fact clinical studies show that retrieved stems do not present uniform osseointegration all over the porous coated surfaces and some stems are surrounded by a layer of soft tissue [2]. Among the factors that may inhibit or destroy the osseointegration are the mechanical ones, such as large displacements and high stresses in the bone/implant interface. Thus, for a long term stability it is required a satisfactory initial stability, that is, in order to have a stable and well osseointegrated stem it is necessary that the interface displacements and stresses are within admissible biological values. An adverse interface condition can be induced by a severe or inconvenient load, but the stem properties (shape, size, material and coating) also play a role in the process. The biologic limits of relative displacement and stresses to have osseointegration are not definitely known. For instance, Viceconti et al. [3] reports that the limit value for the tangential relative displacement, in order to have bone ingrowth, is a value between 30 and 150  $\mu\text{m}$ , and that displacements between 150 and 220  $\mu\text{m}$  lead to the formation of a soft tissue fibrous layer, circumventing a complete fixation. Concerning the decision of employing cement versus cementless stems, there are several factors of influence but among them is the patient age [1]. In fact cementless stems have some advantages, mainly in the event of revision surgeries and this is especially significant for younger patients.

Although interface conditions and the osseointegration process have been studied in several research works (see e.g. [4, 5]), the only method that integrates osseointegration analysis and bone remodeling is presented in Fernandes *et al.*

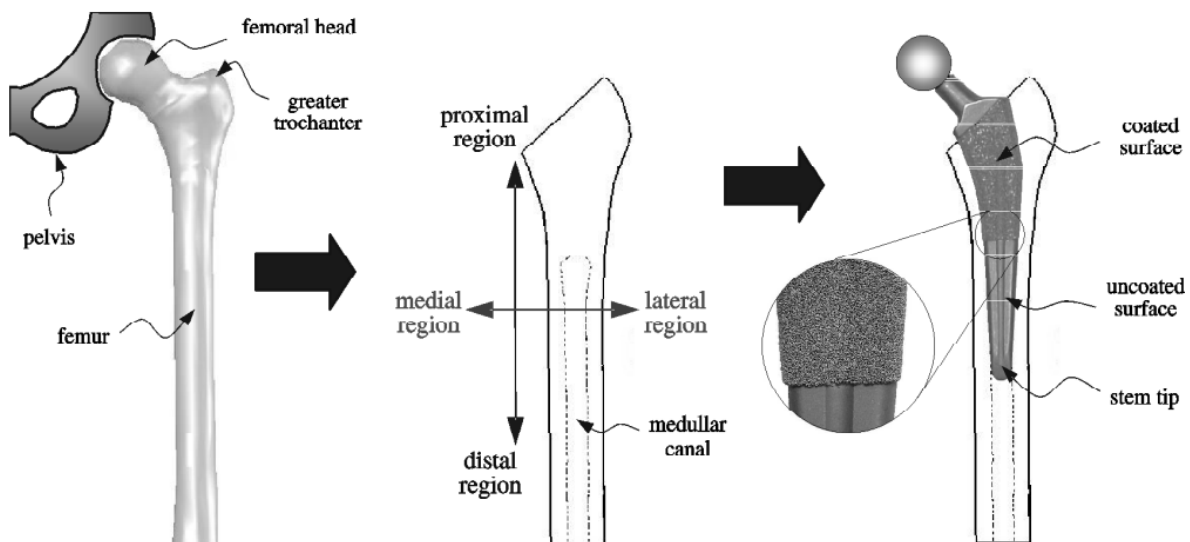


**Figure 1:** Cementless Total Hip Arthroplasty.

al. [6]. The work reported herein extends this work improving the model by incorporating the interface stress influence.

In the present model, the osseointegration process is modeled based on the relative displacement between bone and stem as well as on interface stress level. The biological fixation is not dissociated with the surrounded bone remodeling. Thus the model combines osseointegration with bone remodeling. The law of bone remodeling is derived from a material optimization criterion, based on the minimization of a function that takes into account structural stiffness and bone mass maintenance metabolic cost, and where bone is modeled as a porous material with variable relative density. The problem considers contact conditions on the interface between bone and implant. During the remodeling process, the mechanical interface conditions are updated according with the

---

osseointegration algorithm: if the displacement and stress conditions required for bone attachment are satisfied, then a connection between bone and implant is established. Consequently, the bone behavior is fully simulated from the immediate post operative condition to a long term condition. The osseointegration process emphasizes the behavior of the bone/stem interface, addressing the problem of prosthesis stability.

The model developed is used to analyze a conservative stem (Mayo, Zimmer Inc.) comparing its performance with a conventional one (Trilock, Depuy Orthopaedics, Johnson&Johnson). Results allow the computational model validation and appraise the performance of these two distinct stems.

## 2 METHODS

An iterative procedure is developed to simulate the bone behavior from the immediate post operative condition until a long term condition. This iterative procedure includes two biomechanical models, the osseointegration model and the bone remodeling model. The osseointegration model is presented in first place followed by the remodeling model and by the concurrent computational model.

### 2.1 Osseointegration Model

A characteristic of a porous coated cementless stems is the biological fixation by bone and metal interaction [2]. After insertion, the bone starts to attach to the stem surface stabilizing the prosthesis (figure 2).

This process is enhanced by the high coefficient of friction of a coated surface [7]. However and despite the coating, high relative displacements can occur in certain regions resulting in inhibition of osseointegration [4]. Furthermore, this early bony attachment can be destroyed [8] and among possible reasons one can postulate that the stress level is the most relevant. In fact, in the osseointegration model proposed in Viceconti et al. [5] the interface stress level is taken into account. However, clinical experience states that stem failure is observed to result from failure of initial ingrowth attachment rather than deterioration of osseointegration [6]. Notwithstanding one can consider that a large and well established osseointegrated zone can hardly be disrupted, in the early stage the existing spot weld sites of bony attachment can be broken, and that can affect the overall pattern of osseointegration. Therefore, in this work the osseointegration process is modeled based on the relative displacement between bone and stem as well as on the interface stress level. The model proposes an evolutionary or iterative procedure to determine where osseointegration occurs.

The implanted femur is considered under the action of several load cases, simulating the patient activity. In the immediate post-operative situation no osseointegration is considered. In fact, after the insertion of the stem into the bone one should consider, for the bone/stem interface

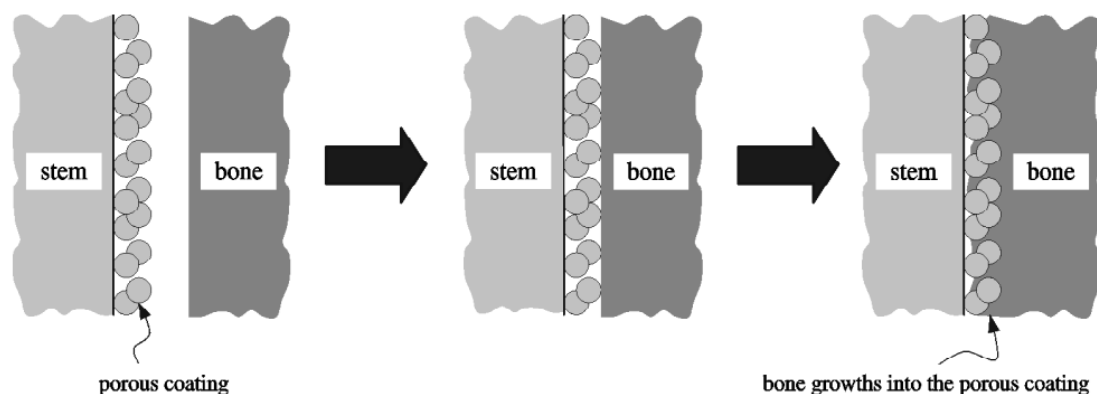


**Figure 2: Osseointegration**

condition, the contact between bone and stem. Thus, the initial interface conditions are contact with friction in the coated surface and contact without friction in the smooth uncoated surface. In each iteration (or time step) of the osseointegration algorithm, the interface relative displacement and interface stresses are computed. If, at a certain point in the contact interface, contact actually happens and the bone/stem relative displacement is less than a threshold value, than a connection between bone and stem is established. Osseointegration is assumed and the connection is set to completely bounded. If, at a certain point where osseointegration was already achieved, the interface stress level is too severe, than the connection between bone and stem is removed. In the next iteration that point will belong to the bone/stem contact interface. The osseointegration algorithm is illustrated in figure 3.

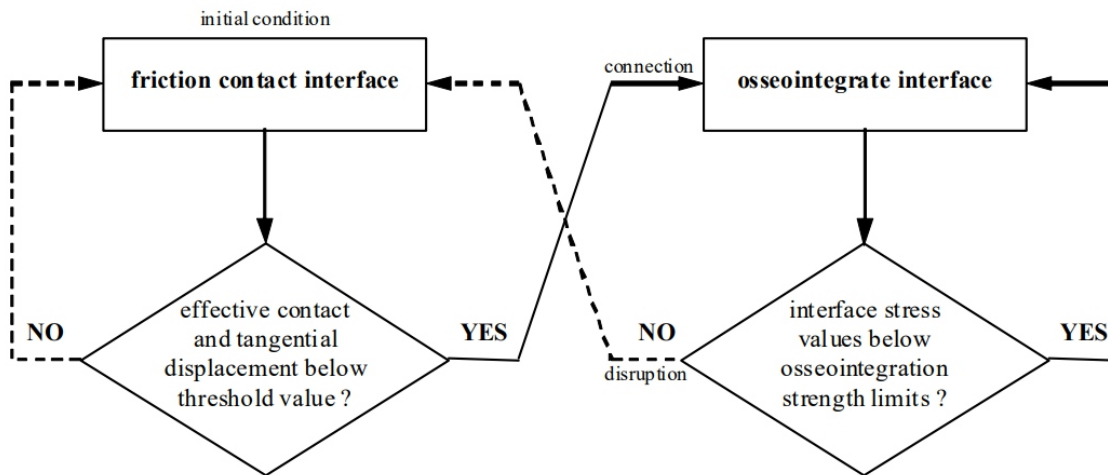


**Figure 3:** Osseointegration model

Note that in order to achieve or to maintain the osseointegration, the above conditions must be verified for every load case.

A consequence of the model is that, on the coated surface, we simultaneously have regions where contact with friction occurs and bonded regions, as determined by the relative displacement and interface stress level at each location. Furthermore, these conditions can change at each iteration (or time step) depending upon the instantaneous relative displacement and interface stresses.

Another issue is the choice of the threshold displacement value and the strength limit of the osseointegration. An experimental study with dogs relates occurrence of osseointegration for displacement values of 0 and 20  $\mu\text{m}$ , but for 40 and 150  $\mu\text{m}$  bone ingrowth does not emerge or it is not totally defined [8]. For humans, some authors reference values between 50 and 150  $\mu\text{m}$  for the threshold displacement value [9, 10]. In the examples presented in this work it is used a threshold value of 50  $\mu\text{m}$ . In relation to the strength limit, it depends on the type of the coated surface as well as the time that have passed after osseointegration was initiated. In Svehla et al. [11] five different types of coat surfaces for a titanium stem are tested. One of the coat surface that is tested is Porocoat (Depuy Orthopaedics, Johnson&Johnson), the porous coat that is used in the tapered stem. Shear stress limits are presented for 4, 8 and 12 weeks after the insertion and for Porocoat shear stress limits are  $18 \pm 10$  MPa after 4 weeks,  $33 \pm 5$  MPa after 8 weeks and  $35 \pm 5$  MPa after 12 weeks. Concerning the tensile limit value, Viceconti et al. [5] reference a value between 0.7 MPa and 0.9 MPa. In order to perform a long term analysis, it was select the osseointegration stress limits corresponding to a longer period of time after the insertion. Thus, in the examples presented in this work it is used a shear stress limit of 35 MPa and a tensile stress limit of 0.8 MPa.

When one compares the extended model derived in this work and the original model presented in

Fernandes et al.[6], the difference is the disruption condition. The present model considers not only the displacement but also the interface stress level. In fact, the original model [6] is just in the displacement and once a point is set to bounded it will remain bounded until the end of process – no disruption condition. This “small” change may have large influence in the overall pattern of osseointegration.

## 2.2 Bone Remodeling Model

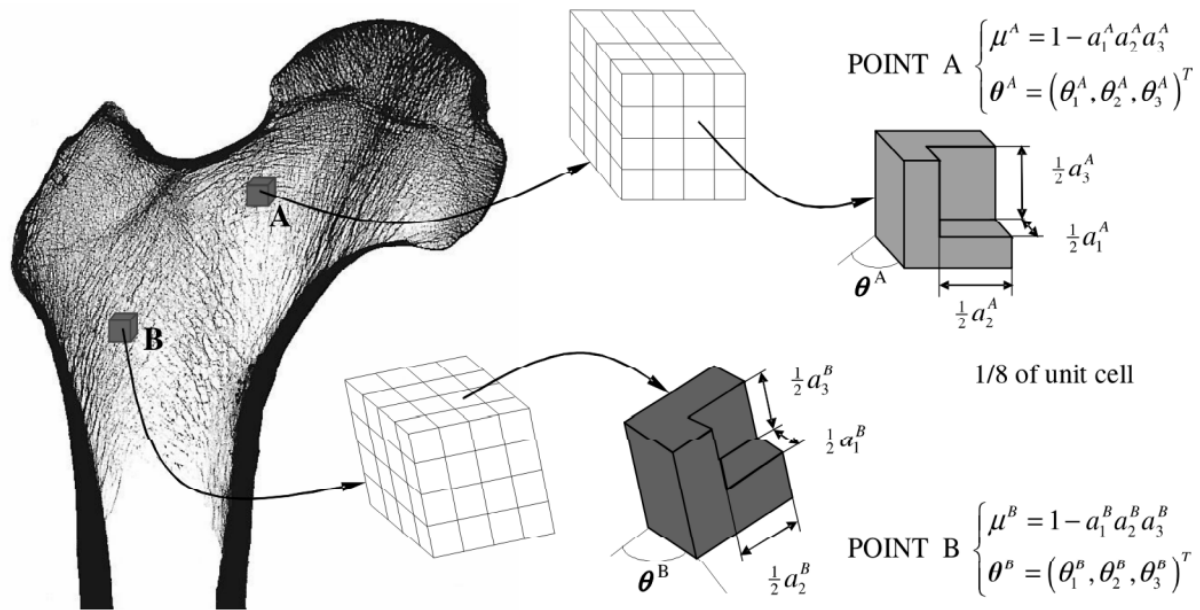
To obtain the law of bone remodeling, a material model for trabecular bone is introduced, with a variable density (the opposite of porosity) from point to point. This porous material is obtained by the locally periodic repetition of a unitary micro cell, with a parallelepiped hole of dimensions  $a = \{a_1, a_2, a_3\}$ , and where density can be obtained by  $\rho = 1 - a_1 \cdot a_2 \cdot a_3$  (figure 4).

The selection of this material model leads to an orthotropic porous material. Thus, at each point bone is characterized by the microstructure parameters  $a_1, a_2$  and  $a_3$ , which define the local relative density. The apparent material properties are calculated through an asymptotic homogenization method [12].

The bone remodeling model consists on the computation of relative bone density, at each point, by the solution of an optimization problem formulated in the continuum mechanics context and assuming contact conditions for the bone/stem interface. Assuming bone adapts to the mechanical environment in order to obtain the stiffest structure for the applied loads, the optimization problem consists of minimizing a linear combination of structural compliance and the metabolic cost to the organism of maintaining bone tissue. The design variables are the hole dimensions of the microstructure defined above. These variables have values in the interval  $a_i \in [0, 1]$ ,  $i=1,2,3$ , where the extreme values,  $a = 0$  and  $a = 1$ , correspond to compact bone and void respectively, while intermediate values correspond to trabecular bone with a given apparent density. One assumes trabecular bone tissue (cell walls) has the mechanical properties of compact bone. The solution of this problem yields the law of bone remodeling,

$$\sum_{P=1}^{NC} \left[ \int_{\Omega} \frac{\partial E_{ijkl}}{\partial \mathbf{a}} e_{kl}(\mathbf{u}^P) e_{ij}(\mathbf{v}^P) d\Omega \right] + \kappa \int_{\Omega} \frac{\partial \mu}{\partial \mathbf{a}} d\Omega = 0 \quad (1)$$

in the sense that when this equation holds the remodeling equilibrium is achieved and at this point the bone correspond to the stiffest structure with total mass regulated by the parameter  $\kappa$  that quantifies biological factors [13]. Thus, this law reflects both mechanical advantage and metabolic cost. In equation (1)  $NC$  is the number of load cases,  $E_{ijkl}$  is the material properties tensor (homogenized properties for trabecular bone),  $e_{ij}$  is the strain field, and  $\mathbf{u}^P$  and  $\mathbf{v}^P$  are the set of state and adjoint virtual displacements, respectively. A detailed description of the derivation of optimality conditions is presented in Fernandes et al. [6].



### 2.3 Computation Model

The computational model contains the osseointegration model and the bone remodeling model. Both models are solved in iterative procedures and, in this work, iterations in the two biomechanical models are performed simultaneously. The computational procedure is based in a finite element model of an implanted femur. Succinctly the computational procedure is as follows: First the bone homogenized elastic properties are computed for an initial solution. Next, one computes the set of displacement fields  $u^P$  and the set of adjoint displacements  $v^P$  using the finite element method. The convergence conditions for osseointegration and

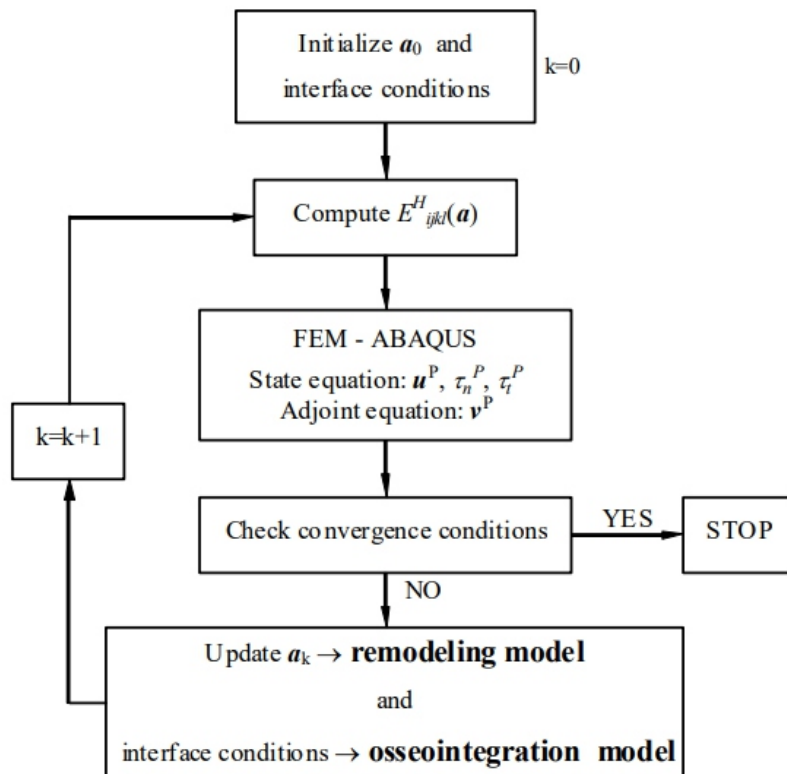


**Figure 5:** Computational model.

---

remodeling are checked and if they are not satisfied, improved values of densities (cell parameters) are computed, the interface conditions are updated and the process restarts (figure 5).

To minimize the computational cost, a mesh of homogenized coefficients is previously computed using PREMAT [12]. Then the homogenized properties are calculated by interpolation of the previously computed values.

The equilibrium and the adjoint problem are solved by the finite element method, making use of the commercial code ABAQUS [14]. The contact problem is solved using standard parameters of ABAQUS with an infinitesimal sliding formulation and Lagrange multipliers to compute the tangential force.

The density (i.e., the sizes of the micro cell holes) is interpolated in a constant mode in each finite element, which let us to write the optimal condition independently for each finite element. The solution for the cell parameters,  $a_i$ , is obtained by an iterative process based on a first order Lagrange method. The design parameters for the element  $e$  in the iteration  $k$  are obtained from the solution of the law of remodeling equation (1).

Concerning the interface conditions, as was previously mention, initially the bone/stem interface conditions are set to contact with friction on the coated area and contact without friction on the non-coated zone. On the coated area, the contact surface in ABAQUS is modeled as nodes against to surface and the analysis describe in the osseointegration model is performed in the slave nodes of the bone/stem interface (see [14] for details). After the initial contact analysis, the interface conditions are updated based on the absolute value of the relative displacement and interface stresses. For each contact node in the friction contact interface, the relative displacement is computed and if the value verifies the condition for osseointegration, bone and stem are bounded in that point. Otherwise that node remains in the friction contact interface. For each “contact” node osseointegrated the interface stresses are computed and if the stresses are below the strength limits, bone and stem remains bounded in that point. Otherwise, the connection between bone and stem is removed and the node that was in the osseointegrate interface goes to the friction contact interface.

Thus, for every iterations of the computational procedure, the interface condition must be updated for each node of the coated interface, as well as the densities for each element of bone

### 3. GEOMETRIC AND FINITE ELEMENT MODEL

The computational model was applied to a three-dimensional model of an implanted left femur. The finite element mesh was created using the bone geometry of the “Standardized Femur” [15] and two different stem geometries were considered. One is based on a conservative stem (Mayo, Zimmer Inc.) and the other, a conventional tapered one, based on the tapered stem (Trilock, Depuy Orthopaedics, Johnson&Johnson). Figure 6 shows the computational geometric model for the implanted femur with the conservative stem.

In the proximal part (see figure 1), before the stem reaches the medullar cavity, it is assumed a perfect adjust between bone and stems. Both stems are proximal half coated stems, i.e., just a portion on the upper part of the stem surface is porous coated (figure 7). So, in the computer model, above a certain point all the stem surface is modeled as coated. This mimics conveniently the tapered stem but it is not the case for the Mayo stem, where uncoated stripes coexist with the coated surface. Thus, in the computer model the conservative stem has, in a certain sense, a larger coated surface than the one existing in the Mayo stem.

The femur is fixed on the lower extremity, the articulation load is applied on the top of the stem ( $F_h$ ) and a global muscles force is applied in the greater trochanter zone ( $F_a$ ). Three load cases (table 1) are taken into account to mimic two situations of walking (load case 1 and 2) and a stair climbing situation



**Figure 6:** Computational geometric model for the implanted femur with the conservative stem.

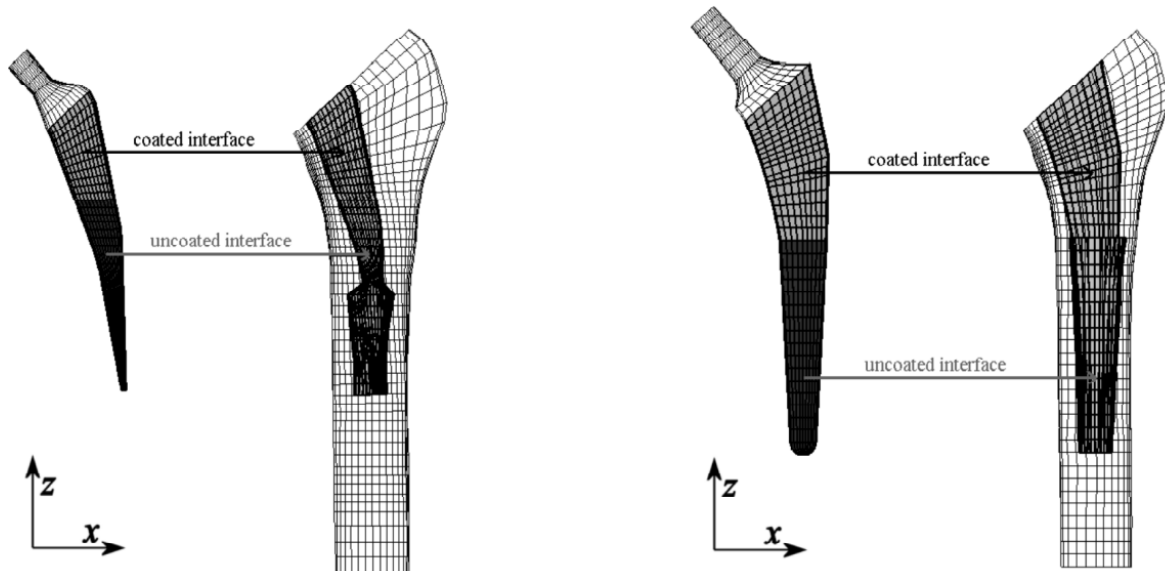


**Figure 7:** Finite element model for the implanted femur with the conservative stem (left) and with the tapered stem (right).

**Table 1** Applied Load Cases

Load		$F_x$ (N)	$F_y$ (N)	$F_z$ (N)
1	$F_a$	-768	-726	+1210
	$F_h$	+224	+972	-2246
2	$F_a$	-166	-382	+ 957
	$F_h$	-136	+630	-1692
3	$F_a$	-383	-669	+ 547
	$F_h$	-457	+796	-1707

---

Stem material is titanium with a Young modulus of 115 GPa and Poisson coefficient of 0.3. In each finite element of bone, the mechanical properties depend on the density value (cell parameters). In this work the initial distribution density is homogenous with a value of 0.7. For compact bone a Young modulus of 20 GPa and Poisson coefficient of 0.3 is considered. It was assumed that bone tissue, which forms wall cells of trabecular bone, has the mechanical properties of compact bone. The finite element mesh uses 8 nodes hexahedron elements and the maximum number of iterations is set to 100.

With respect to the “biological parameter” presented in the remodeling model, it was used a value  $\diamond = 0.1 \times 10^5$ .

Concerning the coating, it was assumed that both stems have the same coating mechanical properties. This simplification is a convenient approach to compare the different shape and size of the stems. For the friction coefficient it was used a density is homogenous with a value of 0.7. For compact bone a Young modulus of 20 GPa and Poisson coefficient of 0.3 is considered. It was assumed that bone tissue, which forms wall cells of trabecular bone, has the mechanical properties of compact bone.

The finite element mesh uses 8 nodes hexahedron elements and the maximum number of iterations is set to 100.

With respect to the “biological parameter” presented in the remodeling model, it was used a value  $\diamond = 0.1 \times 10^5$ .

Concerning the coating, it was assumed that both stems have the same coating mechanical properties. This simplification is a convenient approach to compare the different shape and size of the stems. For the friction coefficient it was used a value of 0.6, corresponding to a stem coated by micro spheres [17]. In relation with the osseointegration strength limits, for the shear stress limit was used a value of 35 MPa. This value is the average value presented for a titanium coated stem with Porocoat (Depuy Orthopaedics, Johnson & Johnson), 12 weeks after the stem insertion [11]. For the tensile stress limit it was used the value of 0.8 MPa [5].

Finally, for the displacement threshold value required in the osseointegration model, it was used a value of 50 mm [9, 10].

## 4. RESULTS

### 4.1 Osseointegration Results

In order to analyze the influence of the interface stress condition in the osseointegration, we compare results based only in the interface displacement condition and results that include the interface displacement condition and the interface stress condition. The model derived in Fernandes et al. [6] does not considerer a disruption condition, it is based only in the interface displacement between bone and stem. The extended model derived in the present work includes the interface displacement condition as well as the interface stress condition, and consequently it has a disruption condition. In figures 8 to 11 are presented osseointegration results in the end of the iterative process.

Figures 8 and 9 shows the osseointegration patterns for the conservative stem and figures 10 and 11 shows the osseointegration patterns for the tapered stem. The results presented in figures 8 and 10 just take into account the displacement condition–model without a disruption condition. The results presented in figures 9 and 11 take into account the interface displacement condition and the interface stress condition–model with a disruption condition.

The uncoated surface is presented in white, coated surface in light gray and the osseointegrate surface presented in dark gray. In table 2 it is presented the percentages of the osseointegrate surface, when compares with the all coated surface. Percentages are computed in terms of the number of nodes. The data is presented for the overall coated surface, as well as for each partial region of the stem (rotating

---

anticlockwise; medial, anterior, lateral and posterior region). For each partial region it is indicated in parentheses the contribution for the overall surface.

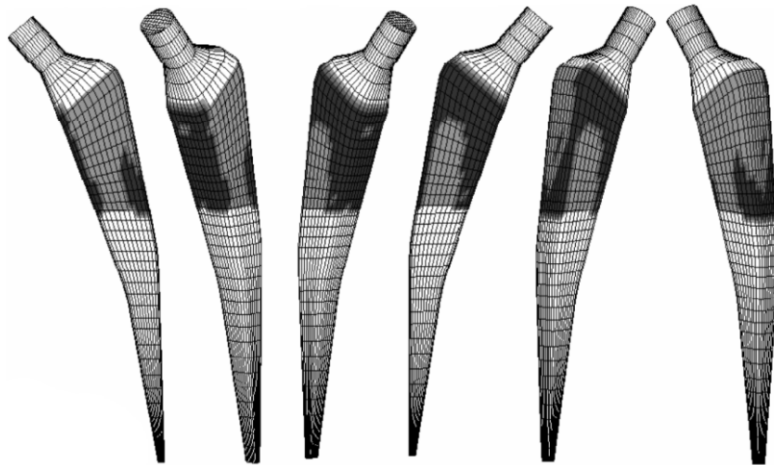


**Figure 8:** Osseointegration pattern for the conservative stem – model without a disruption condition.

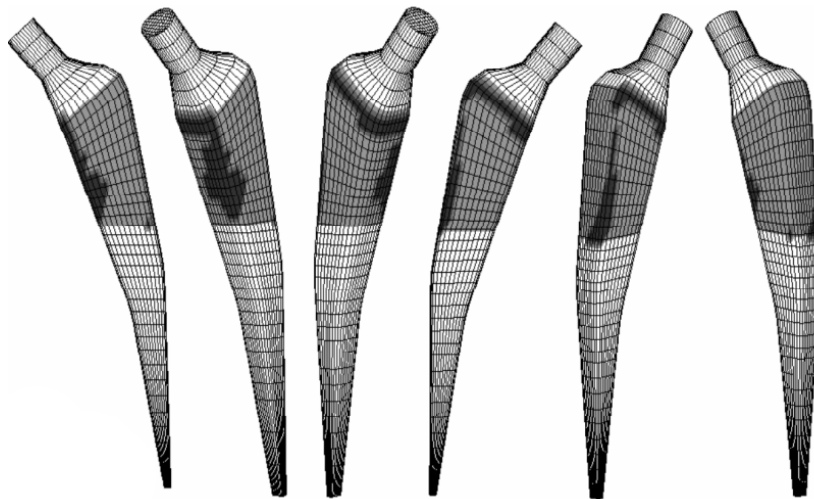


**Figure 9:** Osseointegration pattern for the conservative stem–model with a disruption condition.

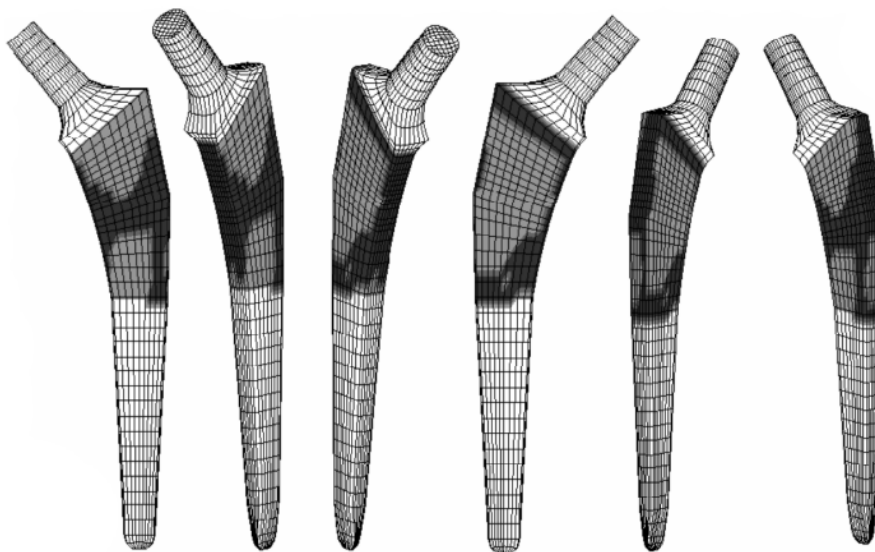


**Figure 10:** Osseointegration pattern for the tapered stem – model without a disruption condition.

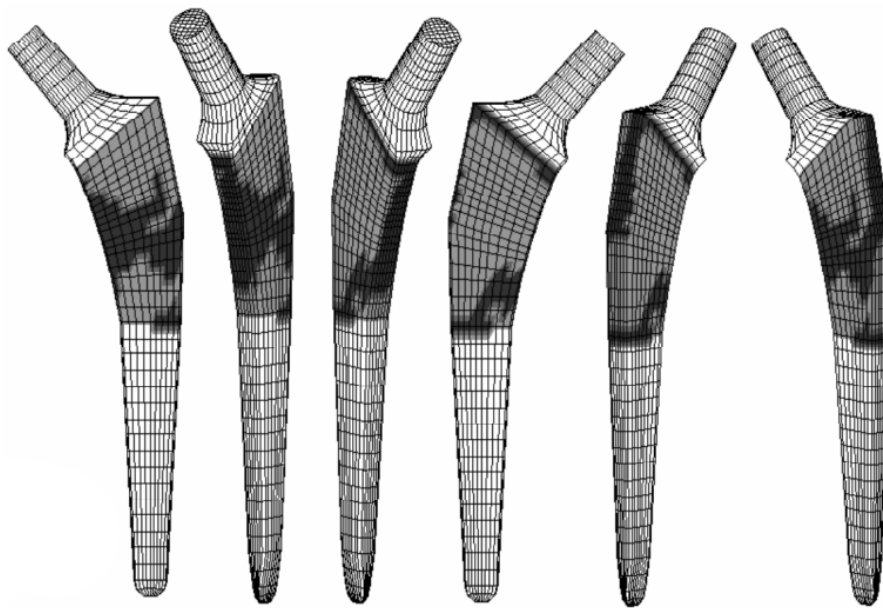


**Figure 11:** Osseointegration pattern for the tapered stem–model with a disruption condition.

**Table 2** Percentage of Nodes Osseointegrated

<i>stem</i>	<i>model without a disruption condition</i>					<i>model with a disruption condition</i>				
	<i>medial</i>	<i>anterior</i>	<i>lateral</i>	<i>posterior</i>	<i>overall</i>	<i>medial</i>	<i>anterior</i>	<i>lateral</i>	<i>posterior</i>	<i>overall</i>
conservative	95.4% (21.5%)	25.0% (6.8%)	41.7% (9.4%)	61.4% (16.9%)	54.6%	50.0% (11.3%)	15.9% (4.4%)	13.0% (2.9%)	22.0% (6.0%)	24.6%
tapered	93.0% (17.4%)	47.9% (15.0%)	78.9% (14.8%)	33.2% (10.4%)	57.6%	81.6% (15.3%)	40.5% (12.6%)	54.4% (10.2%)	20.0% (6.3%)	44.4%

Results show the influence of the disruption condition; computational osseointegration patterns are less extent for the model that takes into account a disruption condition. This influence is more pronounced for the conservative stem and fairly noticed for the tapered stem. Nevertheless, and independently of the model that is used, osseointegration is attained for both stems, even if for the conservative stem with the model with a disruption condition the extent of the osseointegration is minimal. Furthermore, in this case, the most part of osseointegration is achieved in places where Mayo stem has uncoated stripes. Thus, there is some concern with this result for the conservative stem and it requires further investigation.

Comparing the osseointegration attained in each region of the two stems there are similarities but also some differences. For both stems one major part of the osseointegration occurs in the medial zone of the stem (see figure 1). The tapered stem obtain more osseointegration on the anterior part of the stem than on the posterior part, in agreement with clinical results. The conservative stem obtain more osseointegration on the posterior part than on the anterior, at least for the model without a disruption condition.

#### 4.2 Bone Remodeling Results

Figure 12 shows the remodeling results, for both stems, obtained in the end of the iteration process. Results are presented in a gray scale where black represents compact bone, white represents void zones and gray represents the trabecular bone with intermediate density. For each stem are show a anterior and

---

a posterior cross cut.

For both stems, compact bone is obtained in the distal region while in the proximal region one can see the formation of trabecular bone enclosed by a cortical bone shell, reproducing the morphology of the femur.

One can verify that the femur implanted with the conservative stem has less absorption than the one implanted with the tapered stem (the remodeling solution for conservative stem presents more bone mass than the solution for the tapered stem). This can be justified by the fact that the conservative stem has a minor length and a minor size of the coated surface, when compare with the tapered stem. Consequently, the tapered induces a more pronounced bone atrophy than the conservative stem.

Furthermore, for the tapered stem, one can see the densification in the proximal anterior part of the femur in the adjacent zone of the osseointegrate interface (compare figure 11 and figure 12). This result is an evidence of the interconnection between osseointegration and bone remodeling phenomena.

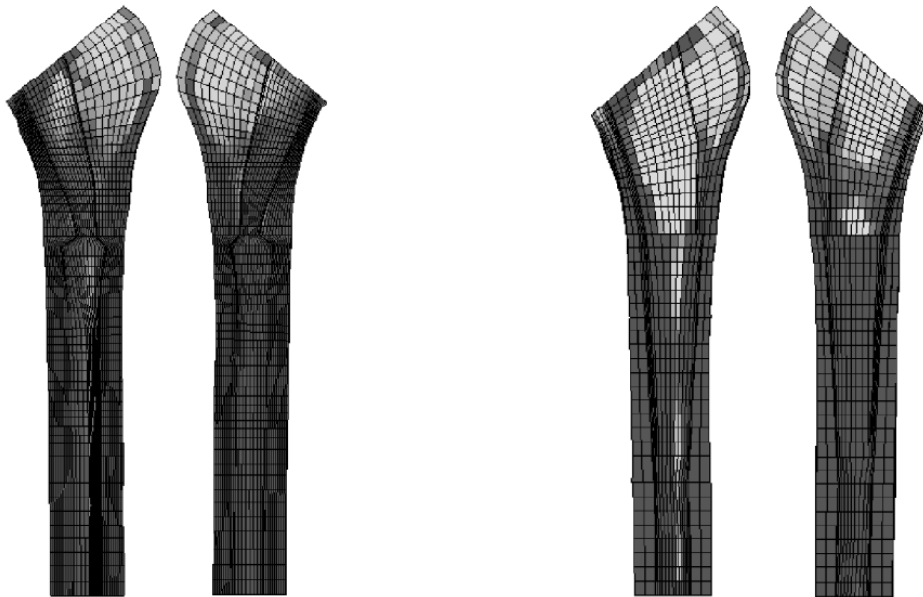


**Figure 12:**Remodeling results for conservative stem (left) and tapered stem (right).

## 5. CONCLUSION

In this work a computational model to simulate the osseointegration and the bone remodeling processes in a cementless femoral stem was developed. The osseointegration process is modeled based on the relative displacement between bone and stem as well as on interface stress level. The model combines the osseointegration analysis with a bone remodeling model where the law of bone remodeling is derived from a material optimization problem (Fernandes et al. [6]). The bone behavior is fully simulated from the immediate post operative condition until a long term condition, where the osseointegration process emphasizes the behavior of the bone/stem interface, addressing the problem of stability of the prosthesis. The model was applied to analyze a conservative stem (Mayo, Zimmer Inc.) comparing its performance with a conventional one (Trilock, Depuy Orthopaedics, Johnson&Johnson). To test the influence of the disruption condition included in the derived osseointegration model, results are compared with a model without a disruption condition.

Obtained results show that osseointegration was attained for both stems. Results also show the influence of considering the interface stress level in the osseointegration process.

Actually, the disruption condition based on the interface stress reduces the amount of the osseointegrated region. This reduction is more moderated for the tapered stem than for the conservative

---

stem. Further investigation should be performed to confirm these results.

In the model, the disruption condition depends on the strength of the osseointegration. This strength is represented by one value for the normal stress and other for the shear stress. However, in vivo the osseointegration strength depends on the elapsed time after the beginning of the osseointegration process [11]. In order to perform a long term analysis, it was selected the osseointegration stress limits corresponding to the longest period of time after the insertion. On the other hand, most of the disruption happens immediately after the bone attachment, that is, in the iterations immediately after the connection is established. So, an improvement can be thought for the computational osseointegration model: the value considered for the osseointegration strength can increase with time. Furthermore, results are sensitive to geometric modeling of the implanted femur. Thus, an adequate control of the modeling, including a geometry and initial density distribution obtained from medical images can concur for the results reliability.

## ACKNOWLEDGMENT

This work was supported by POCI 2010 and Portuguese Foundation for Science and Technology (FCT)

## REFERENCES

- [1] P. Herberts, J. Kärrholm, G. Garellick, L. Linder, A. Lundberg and A. Wykman, *Annual Report 2004 – The Swedish National Hip Arthroplasty Register*, [www.jru.orthop.gu.se](http://www.jru.orthop.gu.se), 2005.
- [2] C. Engh, J. Bobyn and A. Glassman, *Porous-Coated Hip Replacement - The Factors Governing Bone Ingrowth, Stress Shielding, and Clinical Results*. *Journal of Bone and Joint Surgery*, 69-B, N.1, 45-55, 1987.
- [3] M. Viceconti, L. Monti, R. Muccini, M. Bernakiewicz and A. Toni, *Even a thin layer of soft tissue may compromise the primary stability of cementless hip stems*. *Clinical Biomechanics*, 16, 765–775, 2001.
- [4] T. Keaveny and D. Bartel, *Effects of Porous Coating, With and Without Collar Support, On Early Relative Motion for a Cementless Hip Prosthesis*. *Journal of Biomechanics*, 26, N. 12, 1355-1368, 1993.
- [5] M. Viceconti, A. Pancanti, M. Dotti, F. Traina and L. Cristofolini, *Effect of the initial implant fitting on the predicted secondary stability of a cementless stem*. *Medical & Biological Engineering & Computing*, 42, 222-229, 2004.
- [6] P. R. Fernandes, J. Folgado, C. Jacobs and V. Pellegrini, *A contact model with ingrowth control for bone Remodeling around cementless stems*. *J. of Biomechanics*, 35, N.2, 167- 176, 2002.
- [7] J. Kuiper and R. Huiskes, *Friction and Stem Stiffness Affect Dynamic Interface Motion in Total Hip Replacement*. *Journal of Orthopaedic Research*, 14, N.1, 36-43, 1996.
- [8] M. Jasty, C. Bragdon, D. Burke, D. O'Connor, J. Lowenstein, W.H. Harris, *In vivo skeleton responses to porous-surfaced implants subjected to small induced motions*. *Journal of Bone and Joint Surgery*, 79-A, N.5, 707-14, 1997.
- [9] M. Viceconti, R. Muccini, M. Bernakiewicz, M. Baleani and L. Cristofolini, *Large-sliding contact elements accurately predict levels of bone-implant micromotion relevant to osseointegration*. *J. of Biomechanics*, 33, 611-1618, 2000.
- [10] C. A. Engh, D. O'Connor, M. Jasty, T. F. McGovern, J. D. Bobyn, W. H. Harris, *Quantification of implant micromotion, strain shielding, and bone resorption with porous-coated anatomic medullary locking femoral prostheses*. *Clin Orthop*, 285, 13-29, 1992.
- [11] M. Svehla, P. Morberg, B. Zicat, W. Bruce, D. Sonnabend, W.R. Walsh, *Morphometric and mechanical evaluation of titanium implant integration: Comparison of five surface structures*. *J Biomed Mater Res*, 51, 15–22, 2000.

- 
- [12] J. M. Guedes, N. Kikuchi, *Preprocessing and postprocessing for materials based on the homogenisation method with adaptive finite elements methods. Computer Methods in Applied Mechanics and Engineering*, 83, 143-98, 1990.
- [13] P. Fernandes, H. Rodrigues and C. Jacobs, *A Model of Bone Adaptation Using a Global Optimization Criterion Based on the Trajectorial Theory of Wolff. Comp. Meth. Biomech. and Biomedical Eng.*, 2, 125-138, 1999.
- [14] ABAQUS, Version 6.5, Hibbit, Karlsson & Sorensen, Inc., 2004.
- [15] M. Viceconti, M. Casali, B. Massari, L. Cristofolini, S. Bassini and A. Toni, *The 'Standardized Femur Program' Proposal for a Reference Geometry to be Used for The Creation of Finite Element Models of the Femur, Journal of Biomechanics*, 29, N.9, 1241, 1996.
- [16] J. H. Kuiper, *Numerical optimization of artificial hip joint designs, PhD Thesis, Katholieke Universiteit Nijmegen*, 1993.
- [17] M. Dammak, A. Shirazi-Adl, M. Schwartz and L. Gustavson, *Friction Properties at the Bone-Metal interface: Comparison of Four Different Porous Metal Surfaces. J. of Biomedical Materials Research*, 35, 329-336, 1997

---

# Computational Modelling of Ligaments at Non-physiological Situations

**B. Calvo, E. Peña, M.A. Martínez and M. Doblaré**

Group of Structural Mechanics and Material Modelling, Aragon Institute of Engineering Research  
(I3A)University of Zaragoza (Spain)

## ABSTRACT

*A proper understanding of joints biomechanics is essential to improve the prevention and treatment of their disorders and injuries. Despite the many investigations developed in this field, the exact mechanical behavior of the different human joints and the causes of many of their injuries are not completely known yet. Computational models provide therefore a powerful tool for the study of joint function, prosthesis design, and the effects of joint reconstruction. Reliability of these models strongly depends on a precise geometrical reconstruction and on an accurate mathematical description of the behavior of the biological tissues involved, and their interactions with the surrounding environment.*

*The objective of the paper is to describe constitutive models for addressing the computational modelling of ligaments under non-physiological loads. Hyperelastic, viscoelastic, initial strains and damage models are presented to describe the mechanical behavior of ligaments in these situations. In order to show the performance of the framework presented herein, a complex 3D numerical application to ligament mechanics of the anterior cruciate ligament is presented. Results show that the model is able to capture the typical stress-strain behavior observed in ligaments at non-physiological situations and seem to confirm the soundness of the proposed framework.*

**Keyword:** *Computational biomechanics, ligaments, hyperelasticity, viscoelasticity, damage, finite element method Computational modeling of ligaments at non-physiological situations B. Calvo, E. Peña, M.A. Martínez and M. Doblaré*

## 1. INTRODUCTION

Biomechanics is defined as the development, extension and application of mechanics for the purpose of the better understanding physiology and pathophysiology, as well as, the diagnosis and treatment of disease and injury. That is, the overall goal of biomechanics is, and must remain, the general improvement of the human condition [9].

Finite element (FE) method offer, the potential to predict quantities that are difficult or impossible to measure experimentally. In particular, FE method offers the ability to predict spatial and temporal variations in stress, strain, contact area and forces. The FE method also provides a standardized framework for parametric studies, such as evaluation of multiple clinical treatments. A computational analysis may predict possible stress distributions for different geometries and kinematics, provide a basis for evaluation of surgical procedures, and aid in medical education and virtual surgery. The need for such a tool has many uses in the areas of injury assessment and surgery planning [27].

However, the construction of accurate and useful models requires integration of the mechanics concepts, experimental results, and material models and the reliability of these models strongly depends on an appropriate geometrical reconstruction and on an accurate mathematical descriptions of the behavior of the biological tissues involved, and their interactions with the surrounding environment [16].

The construction of an accurate constitutive model is difficult because ligaments are non-linear, anisotropic, inhomogeneous, viscoelastic, and undergo large deformations [27]. In addition, ligaments are usually exposed to a complex distribution of “in vivo” residual stresses as a consequence of the continuous growth, remodelling, damage and viscoelastic strains that they suffer along their whole life [15]. Ligaments, also, exhibit simultaneously elastic and viscous material behavior. This behavior can arise from the fluid flow inside the tissue, from the inherent viscoelasticity of the solid phase, or from viscous interactions between the tissue phases [10]. Furthermore, non-physiological loads drive soft tissue to damage that may induce a strong reduction of the stiffness. In order to obtain a realistic and complete material model under non-physiological situations, elastic behavior, initial strains, viscoelasticity and damage may be coupled to account inelastic features. With all the above in mind, the objective of the paper is to describe constitutive models for addressing the computational modelling of ligaments under non physiological situations using FE method, differentiating between elastic, viscoelastic, initial strains and damage of the ligaments and applications. The paper is organized as follows.

Section 2 describes the basic structure of the ligaments. In Section 3 the constitutive models for ligaments, hyperelasticity, initial strains, viscoelasticity and damage are presented. The application to some examples is presented in section 4. Finally, section 5 includes some concluding remarks.

## 2. STRUCTURE AND PROPERTIES OF LIGAMENTS

Tendons and ligaments are soft tissues composed of closely packed, parallel collagen fiber bundles oriented to provide motion and stability to the musculoskeletal system. Under macroscopic examination, ground substance is observed in the interfibrillar spaces. Although ligaments are considered as composite material consisting of a ground substance matrix reinforced by collagen and elastin, collagen is the primary component that resists the tensile stress in ligaments.

The tensile modulus of the ligament depends on the collagen fibril density, fibril orientation and the amount of collagen cross-linking. When this tissue is tested in tension, the collagen fibrils are aligned and stretched along the axis of loading. For small deformations, when the tensile stress in the specimen is relatively small, a nonlinear toe-region is seen in the stress-strain curve, due to realignment of the collagen fibres, rather than stretching of these fibers. For larger deformations, and after realignment, the collagen fibrils are stretched and therefore generate a larger tensile stress due to the intrinsic stiffness of the collagen fibrils themselves. Due to this phenomenon, the tensile stiffness of ligaments is highly strain dependent (see Fig. 1).

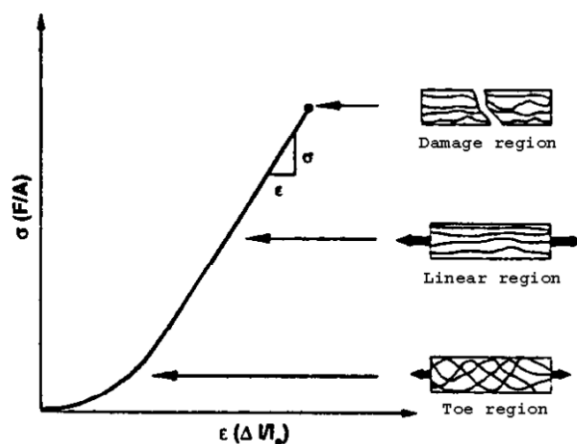


**Figure 1:** Schematic diagram of a uniaxial tensile test where fibers orient in the direction of the load as it increases.

### 3. CONSTITUTIVE MODELS FOR LIGAMENTS

#### 3.1 Continuum Description of the Elastic Behavior

Consider a continuum body with reference configuration  $\mathcal{B}_0$  at the initial reference time  $t = 0$ . Then, an assumed motion  $\chi$  maps this configuration to the current configuration at each time  $t$ . Hence, a point  $X \in \mathcal{B}_0$  transforms to a point  $x \in \mathcal{B}_t$ , where  $X$  and  $x$  define the respective positions of a particle in the reference and current configurations relative to a fixed set of axes. The direction of a fiber at a point  $X \in \mathcal{B}_0$  is defined by a unit vector field  $\mathbf{m}_0(X)$ . It is usually assumed that, under deformation, the fiber moves with the material points of the continuum body. Therefore, the stretch  $\lambda$  of the fiber defined as the ratio between its lengths at the deformed and reference configurations can be expressed as

$$\lambda \mathbf{m}(x, t) = \mathbf{F}(X, t) \mathbf{m}_0(X); \lambda^2 = \mathbf{m}_0 \cdot \mathbf{F}^T \mathbf{F} \cdot \mathbf{m}_0 = \mathbf{m}_0 \cdot \mathbf{C} \mathbf{m}_0 \quad (1)$$

where  $\mathbf{m}$  is the unit vector of the fiber in the deformed configuration,  $\mathbf{F} = \frac{dx}{dX}$  and  $\mathbf{C} = \mathbf{F}^T \mathbf{F}$  are the standard deformation gradient and the corresponding right Cauchy-Green strain measure.

A multiplicative decomposition of  $\mathbf{F} = J^{1/3} \bar{\mathbf{F}}$  and  $\mathbf{C} = J^{2/3} \bar{\mathbf{C}}$  into volume-changing (dilatational) and volume-preserving (distortional) parts is usually established as in [5] and [23].

To characterize isothermal processes, we postulate the existence of a unique decoupled representation of the strain energy density function [23]. Because of the directional dependence on the deformation, we require that the function  $\Psi$  explicitly depends on both the right Cauchy-Green tensor  $\mathbf{C}$  and the fibers direction  $\mathbf{m}_0$  in the reference configuration.

Since the sign of  $\mathbf{m}_0$  is not significant,  $\Psi$  must be an even function of  $\mathbf{m}_0$  and so it may be expressed by

where  $\bar{\Psi}(\bar{\mathbf{C}}, \mathbf{M})$  is the structural tensor [25]. Based on the kinematic description, the free energy can be written in decoupled form as

$$\Psi(\mathbf{C}, \mathbf{m}_0) = \Psi_{vol}(J) + \bar{\Psi}(\bar{\mathbf{C}}, \mathbf{M}) = \Psi_{vol}(J) + \bar{\Psi}(\bar{I}_1(\bar{\mathbf{C}}), \bar{I}_2(\bar{\mathbf{C}}), \bar{I}_4(\bar{\mathbf{C}}, \mathbf{m}_0), \bar{I}_5(\bar{\mathbf{C}}, \mathbf{m}_0)) \quad (2)$$

where  $\Psi_{vol}(J)$  and  $\bar{\Psi}(\bar{\mathbf{C}}, \mathbf{M})$  are given scalar-valued functions of  $J$ ,  $\bar{\mathbf{C}}$  and  $\mathbf{m}_0$  respectively that describe the volumetric and isochoric responses of the material [8],  $\bar{I}_1$  and  $\bar{I}_2$  the first two modified strain invariants of the symmetric modified Cauchy-Green tensor  $\bar{\mathbf{C}}$  (Note that  $\bar{I}_3 = J$  and  $\bar{I}_3 = 1$ ). Finally, the pseudo-invariants  $\bar{I}_4$  and  $\bar{I}_5$  characterize the constitutive response of the fibers [25]:

$$\bar{I}_4 = \mathbf{C} : \mathbf{M}, \bar{I}_5 = \mathbf{C}^2 : \mathbf{M} \quad (3)$$

While the invariant  $\bar{I}_4$  has a clear physical sense, the square of the stretch  $\lambda$  in the fiber direction, the influence of  $\bar{I}_5$  is difficult to evaluate due to the high correlation among the invariants. For this reason and the lack of sufficient experimental data it is usual not to include this invariant in the definition of [25].

We now define the constitutive equation for compressible hyperelastic materials in the standard form

$$\mathbf{S} = 2 \frac{\partial \Psi(\mathbf{C}, \mathbf{M})}{\partial \mathbf{C}} = \mathbf{S}_{vol} + \bar{\mathbf{S}} = J p \mathbf{C}^{-1} + \bar{\mathbf{S}} \quad (4)$$

where the second Piola-Kirchhoff stress  $\mathbf{S}$  consists of a purely volumetric contribution  $\mathbf{S}_{vol}$  and a purely isochoric one  $\bar{\mathbf{S}}$  and  $p$  is the hydrostatic pressure. The associated decoupled elasticity tensor may be written as

$$C = C_{vol} + C_{iso} = 2 \frac{\partial \mathcal{S}_{vol}}{\partial C} + 2 \frac{\partial \bar{\mathcal{S}}}{\partial C} \quad (5)$$

Using the push-forward operator we obtain the Cauchy stress tensor  $\mathbf{1}(\cdot)$  and the elasticity tensor in the spatial description  $\mathbf{1} J C(\cdot)$ . For a more detailed derivation of the material and spatial elasticity tensors for completely incompressible or compressible fibred hyperelastic materials and their explicit expressions, see i.e. [8] or [25].

### 3.2 Enforcing Initial Strains of Ligaments

Initial strains are a consequence of the continuous growth, remodelling, damage and viscoelastic strains that suffer living materials along their whole life. Initial strains can be relieved by selective cutting of the living tissue and removal of its internal constraints. In ligaments of diarthrodial joints, initial stretches provide joint stability even in a relatively unloaded joint configuration [7]. Typical residual strains are approximately 3-5% in these ligaments.

In order to describe the current deformation state of a solid, including the effect of initial deformations, three different configurations are usually defined: a) the stress free state (sf), b) the reference state in which the material is unloaded (0) and c) the current deformed state ( $\cdot$ ).

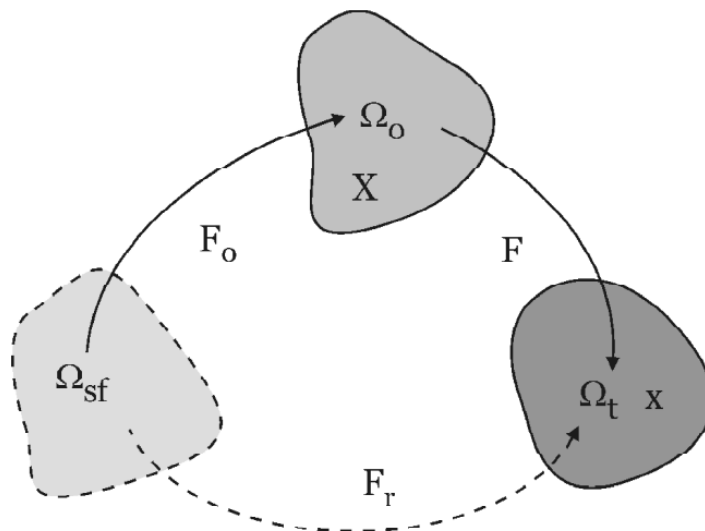


**Figure 2:** Multiplicative decomposition of the total deformation gradient where sf denotes the stress free state, 0 the reference state and the current configuration [15].

It is assumed that the total deformation gradient tensor corresponding to the current state ( $\mathbf{F}_r$ ) admits a multiplicative decomposition [15] such as:

$$\mathbf{F}_r = \mathbf{F} \mathbf{F}_0 \quad (6)$$

The initial stress in the reference state,  $\mathbf{1}(\cdot)$ , is defined for hyperelastic materials in the standard form, by the strain energy density function  $\mathcal{W}(\cdot)$ . Note that this function is always referred to the stress-free state sf while  $\mathbf{1}(\cdot)$  are true stresses in the reference load-free configuration. Then

$$\sigma_0 = \frac{2}{J_0} \chi_* \left[ \frac{\partial \Psi_{\Omega_{sf}}(\mathbf{C})}{\partial \mathbf{C}} \Big|_{\mathbf{C}=\mathbf{C}_0} \right] = \frac{2}{J_0} \mathbf{F}_0 \left[ \frac{\partial \Psi_{\Omega_{sf}}(\mathbf{C})}{\partial \mathbf{C}} \Big|_{\mathbf{C}=\mathbf{C}_0} \right] \mathbf{F}_0^T \quad (7)$$

with  $\chi_*$  the push-forward associated to  $\mathbf{F}_0$  and  $\mathbf{C}_0 = \mathbf{F}_0^T \mathbf{C} \mathbf{F}_0$ . In the same way, it is possible to define the total stresses corresponding to the current state  $\mathbf{C}_r$  in the standard form by using the strain-energy density function  $\Psi_{\Omega_{sf}}$  through  $\mathbf{F}_r$ .

$$\sigma_r = \frac{2}{J_r} \chi_{*r} \left[ \frac{\partial \Psi_{\Omega_{sf}}(\mathbf{C})}{\partial \mathbf{C}} \Big|_{\mathbf{C}=\mathbf{C}_r} \right] = \frac{2}{J_r} \mathbf{F}_r \left[ \frac{\partial \Psi_{\Omega_{sf}}(\mathbf{C})}{\partial \mathbf{C}} \Big|_{\mathbf{C}=\mathbf{C}_r} \right] \mathbf{F}_r^T \quad (8)$$

with  $J_r = J(\mathbf{F}_r)$  and  $\mathbf{C}_r = \mathbf{F}_r^T \mathbf{C} \mathbf{F}_r$ .

Finally, the elasticity tensor in the material description

$$\mathbb{C} = 4 \frac{\partial^2 \Psi_{\Omega_{sf}}(\mathbf{C})}{\partial \mathbf{C} \partial \mathbf{C}} \Big|_{\mathbf{C}=\mathbf{C}_r} \quad (9)$$

As noted,  $\mathbf{F}_0$  is difficult to determine from experiments. In the case of ligaments and tendons, Gardiner et al. [6] proposed a relatively easy form to measure length variations along the fiber direction at different points, that is,  $\mathbf{F}_0$  corresponds to an axial stretch  $\lambda_0$  along the fiber direction  $\mathbf{a}_0$  in the reference state  $\mathbf{C}_0$ . Using the incompressibility condition,  $\mathbf{F}_0$  can be written in a coordinate system (\*) where the fiber direction  $\mathbf{a}_0$  is aligned with the  $X_1$  axis as:

$$[\mathbf{F}_0^*] = \begin{bmatrix} \lambda_0 & 0 & 0 \\ 0 & \frac{1}{\sqrt{\lambda_0}} & 0 \\ 0 & 0 & \frac{1}{\sqrt{\lambda_0}} \end{bmatrix} \quad (10)$$

To introduce initial strains into the finite element formulation, it is necessary to specify  $\mathbf{F}_0$  pointwise within the finite element mesh. An equilibrium step is firstly applied with zero forces with the constitutive behaviour defined by  $\Psi_{\Omega_{sf}}$  in order to obtain a balanced, although not fully compatible configuration. A second load step will result in the deformation gradient  $\mathbf{F}$  that balances the externally applied forces.

### 3.3 Continuum Description of the Viscoelastic Behavior of Ligaments

In order to describe viscoelastic effects we consider the finite-strain anisotropic viscoelastic constitutive behaviour proposed by [14]. They apply the concept of internal variables [22] and postulate the existence of an uncoupled free energy function  $\Psi_{\Omega_{sf}}(\mathbf{C}, \mathbf{Q})$  of the form

$$\Psi(\mathbf{C}, \mathbf{M}, \mathbf{Q}_{ij}) = \Psi_{vol}^0(J) + \bar{\Psi}_0 - \frac{1}{2} \sum_{i=1}^N \sum_{k=m, f_1} (\bar{\mathbf{C}} : \mathbf{Q}_{ik}) + \Xi \left( \sum_{i=1}^N \sum_{k=m, f_1} \mathbf{Q}_{ik} \right) \quad (11)$$

where  $\mathbf{Q}_{ik}$  may be interpreted as non-equilibrium stresses, in the sense of non-equilibrium thermodynamics, and remain unaltered under superposed spatial rigid body motions.  $\bar{\Psi}_0$  is the isotropic contribution due to the matrix material associated to  $I_1$  and  $I_2$  invariants and  $\mathbf{Q}_{ik}$  is the anisotropic contribution due to the fibres associated to  $I_4, I_5$  invariants [14].

Standard arguments based on the Clausius-Duhem inequality  $\int_{\Omega} \dot{\Psi} - \mathbf{S} : \dot{\mathbf{C}} \leq 0$  in  $\Omega$ , lead to the representation

$$\mathbf{S} = 2 \frac{\partial \Psi(\mathbf{C}, \mathbf{M}, \mathbf{Q}_{ik})}{\partial \mathbf{C}} = J p \mathbf{C}^{-1} + J^{-\frac{2}{3}} DEV \left[ 2 \frac{\partial \bar{\Psi}^0(\bar{\mathbf{C}}, \mathbf{M})}{\partial \bar{\mathbf{C}}} - \sum_{i=1}^N \mathbf{Q}_{ik} \right] = \mathbf{S}_{vol} + \bar{\mathbf{S}}^0 - J^{-\frac{2}{3}} \sum_{i=1}^n DEV[\mathbf{Q}_{ik}] \quad (12)$$

where DEV is the deviator operator in the material description [24].

Based on previous studies [19, 21, 26], the ligament is assumed to have a Kelvin-Voigt-type viscoelastic constitutive behaviour. The nonequilibrium second Piola Kirchhof stresses in (12),  $\mathbf{Q}_{ik}$ , are assumed to be governed by a set of linear rate equations

$$\dot{\mathbf{Q}}_{ik} + \frac{1}{\tau_{ik}} \mathbf{Q}_{ik} = \frac{\gamma_{ik}}{\tau_{ik}} DEV \left[ 2 \frac{\partial \bar{\Psi}_k^0(\bar{\mathbf{C}}, \mathbf{M})}{\partial \bar{\mathbf{C}}} \right] \quad (13)$$

$$\lim_{t \rightarrow -\infty} \mathbf{Q}_{ik} = 0$$

where  $\gamma_{ik}$  and  $\tau_{ik}$  are free energy factors associated with relaxation times  $\tau_{ik}$ . The evolution equations (13) are linear and, therefore, explicitly lead to the following convolution representation

$$\mathbf{Q}_{ik}(t) = \frac{\gamma_{ik}}{\tau_{ik}} \int_{-\infty}^t \exp\left[-\frac{(t-s)}{\tau_{ik}}\right] DEV \left[ 2 \frac{\partial \bar{\Psi}_k^0}{\partial \bar{\mathbf{C}}} \right] ds \quad (14)$$

Algorithmically, the constitutive model is appealing since equation (13) can be evaluated via a simple recursion relation which was originally developed for finite strains by [22]. In particular, if the material state is known at a time  $t_n$  and the deformation is known at a time  $t_{n+1}$  with  $t_{n+1} > t_n$ , we may write

$$\begin{aligned} \mathbf{S}_{n+1} = & J_{n+1} p_{n+1} \mathbf{C}_{n+1}^{-1} + J_{n+1}^{-\frac{2}{3}} \sum_{k=m, f_1} \left[ \left(1 - \sum_{i=1}^N \gamma_{ik}\right) \bar{\mathbf{S}}_{(k)n+1}^0 \right] + \\ & + J_{n+1}^{-\frac{2}{3}} \sum_{i=1}^N \left[ \gamma_{ik} \{ DEV[\mathbf{H}_{n+1}^{(ik)}] \} \right] \end{aligned} \quad (15)$$

where  $(\diamond)_{ik} H_n$  are internal algorithmic history variables defined by

$$\mathbf{H}_{n+1}^{(ik)} = \exp\left[\frac{-\Delta t_n}{\tau_{ik}}\right] \mathbf{H}_n^{(ik)} + \exp\left[\frac{-\Delta t_n}{2\tau_{ij}}\right] \left\{ \bar{\mathbf{S}}_{(k)n+1}^0 - \bar{\mathbf{S}}_{(k)n}^0 \right\} \quad (16)$$

where the subscripts  $n$  and  $n+1$  denote quantities evaluated at times  $t_n$  and  $t_{n+1}$  [22,14].

The iterative Newton procedure to solve a nonlinear finite element problem requires the determination of the consistent tangent material operator. This can be derived analytically for the given material equation (5). The symmetric algorithmic material tensor which is expressed as [22]

$$\begin{aligned} \mathbb{C}_{n+1} = & \mathbb{C}_{vol(n+1)}^0 + \sum_{k=m, f_1} [(1 - \gamma_k + \nu_k) \bar{\mathbb{C}}_{(k)n+1}^0 + \\ & - \frac{2}{3} J_{n+1}^{-\frac{4}{3}} \sum_{i=1}^N \gamma_{ik} \{ DEV[\tilde{\mathbf{H}}_n^{(ik)}] \otimes \bar{\mathbb{C}}_{n+1}^{-1} + \bar{\mathbb{C}}_{n+1}^{-1} \otimes DEV[\tilde{\mathbf{H}}_n^{(ik)}] - \\ & - (\tilde{\mathbf{H}}_n^{(ik)} : \bar{\mathbb{C}}) (\mathbb{I}_{\mathbb{C}_{n+1}}^{-1} - \frac{1}{3} \bar{\mathbb{C}}_{n+1}^{-1} \otimes \bar{\mathbb{C}}_{n+1}^{-1}) \}] \end{aligned} \quad (17)$$

with

$$\tilde{\mathbf{H}}_n^{(ik)} = \exp\left[\frac{-\Delta t_n}{\tau_{ij}}\right] \mathbf{H}_n^{(ik)} - \exp\left[\frac{-\Delta t_n}{2\tau_{ij}}\right] \bar{\mathbf{S}}_n^{0(j)} \quad (18)$$

$$\mathbf{H}_{n+1}^{(ik)} = \tilde{\mathbf{H}}_n^{(ik)} + \exp\left[\frac{-\Delta t_n}{2\tau_{ij}}\right] \bar{\mathbf{S}}_{n+1}^{0(j)} \quad (19)$$

### 3.4 On Modeling of Damage Process of Ligaments

In order to reproduce the damage process in ligaments, we consider the directional damage model proposed by Calvo et al. [3]. The damage phenomenon is assumed to affect only the isochoric elastic part of the deformation, as proposed by Simo [22]. The free energy density can be written in a decoupled form, such as

$$\Psi(\mathbf{C}, \mathbf{M}, D_m, D_f) = \Psi_{vol}(J) + (1 - D_m) \bar{\Psi}_0^m(\bar{\mathbf{C}}) + (1 - D_f) \bar{\Psi}_0^f(\bar{\mathbf{C}}, \mathbf{M}, \mathbf{N}) \quad (20)$$

where  $\mathbf{M}$  is the structural tensor,  $(\diamond)_{vol} J$  is a strictly convex function (with the minimum at  $J = 1$ ) which describes the volumetric elastic response,  $(\diamond)_m$  denotes the isochoric effective strain energy density of the undamaged material, which describes the elastic response of the matrix, and  $(\diamond)_f$  denotes the isochoric effective strain energy of the undamage material, which describes the isochoric elastic response of the fibers. The factors  $(1 - D_m)$  and  $(1 - D_f)$  are known as the reduction factors [22], where the internal variables  $(\diamond)_{D_m} [0, 1]$  and  $(\diamond)_{D_f} [0, 1]$  are normalized scalars referred to as the damage variables for the matrix and fibers respectively.

As a particularization of the Clausius-Planck inequality we obtain

$$\mathbf{S} = \mathbf{S}_{vol} + (1 - D_m) \bar{\mathbf{S}}_0^m + (1 - D_f) \bar{\mathbf{S}}_0^f \quad (21)$$

The evolution of the damage parameters  $D_m$  and  $D_f$  is characterized by an irreversible equation of evolution as follows. We define  $\Xi_s^m$  and  $\Xi_s^f$  by the expression [22]

$$\Xi_s^m = \sqrt{2\bar{\Psi}_0^m(\bar{\mathbf{C}}(s))} \quad \text{and} \quad \Xi_s^f = \sqrt{2\bar{\Psi}_0^f(\bar{\mathbf{C}}(s))} \quad (22)$$

where  $\bar{\mathbf{C}}(s)$  is the modified right Cauchy-Green tensor at time  $s$ . Now, let  $\Xi_t^m$  and  $\Xi_t^f$  be the maximum values of  $\Xi_s^m$  and  $\Xi_s^f$  over the past history up to current time  $t$  that is [22]

$$\Xi_t^m = \max_{s \in (-\infty, t)} \sqrt{2\bar{\Psi}_0^m(\bar{\mathbf{C}}(s))} \quad \text{and} \quad \Xi_t^f = \max_{s \in (-\infty, t)} \sqrt{2\bar{\Psi}_0^f(\bar{\mathbf{C}}(s))} \quad (23)$$

We define a damage criterion for the ground substance or matrix in the strain space by the condition that, at any time  $t$  of the loading process, the following expression is fulfilled [22]

$$\phi_m(\mathbf{C}(t), \Xi_t^m) = \sqrt{2\bar{\Psi}_0^m(\bar{\mathbf{C}}(t))} - \Xi_t^m \leq 0 \quad (24)$$

The symmetric algorithmic material tensor which is expressed as

$$\mathbf{C}_{n+1} = \mathbf{C}_{vol(n+1)}^0 + \sum_{k=m, f_1} [(1 - D_{(k)n+1}) \bar{\mathbf{C}}_{(k)n+1}^0 - \bar{\mathbf{S}}_{(k)n+1}] \quad (25)$$

where

$$\bar{\mathbf{S}}_{(k)n+1} = \begin{cases} \bar{\mathbf{g}}'_{(k)n+1} \bar{\mathbf{S}}_{(k)n+1}^0 \otimes \bar{\mathbf{S}}_{(k)n+1}^0 & \text{if } \phi = 0 \text{ and } \mathbf{N}_m : \dot{\mathbf{C}} > 0 \\ 0 & \text{otherwise} \end{cases}$$

#### 4. NUMERICAL EXAMPLES

In order to show the performance of the framework presented herein, some examples are included. The most used isotropically transverse model for ligaments is the early proposed by [29]. However with this model, we can not express the strain energy function in an analytical form. So, the particular form of the deviatoric functions  $\bar{\Psi}_m^0$  and  $\bar{\Psi}_f^0$  used herein are the proposed by [11]

$$\begin{aligned} \bar{\Psi}_m^0 &= C_1(\bar{I}_1 - 3) \\ \bar{\Psi}_f^0 &= \frac{C_3}{2C_4} (\exp^{C_4(\bar{I}_4 - 1)} - C_4(\bar{I}_4 - 1) - 1) \end{aligned} \quad (27)$$

Finally, the volumetric part of the strain energy function is always stated as  $\ln \text{vol D J}$  [8].

##### 4.1 Anterior Cruciate Ligament under Different Strain Rates

Viscoelasticity of ligaments has been clearly demonstrated in creep and stress relaxations tests [17, 18, 19, 28]. There are, however, some variabilities in the findings of different studies performed to evaluate the change in ligament material properties with increasing loading rate [4, 17]. The strain rate during injury is very important regarding the magnitude of the lesion. Therefore, the stress-strain behavior of the ligament is an essential factor.

To illustrate the performance of the visco-hyperelastic behaviour of ligaments and the importance of the strain-rates during their movement, a model of the human anterior cruciate ligament (ACL) was constructed to simulate its behavior under an anterior tibial displacement, see Fig. 4.a. The surface geometries of femur and tibia were reconstructed from a set of Computer Tomography (CT) images, while for the ACL, MRI (Magnetic Resonance Images) were used [13].

Two different strain rates were applied: low (0.012 %S<sup>-1</sup>) and high (50%S<sup>-1</sup>) that correspond to physiological and nonphysiological strain-rates. The elastic and viscoelastic parameters for the human ACL were fitted from published experimental data [17] and are shown in Table 1 and Figure 3. Ligaments were attached to bone. The motion of each bone was controlled by the six degrees of freedom of its reference node. In the analyses, tibia remained fixed. The position at full extension served as the initial reference configuration. An anterior load of 134 N was applied to the femur. In this example we did not consider initial strains [15].

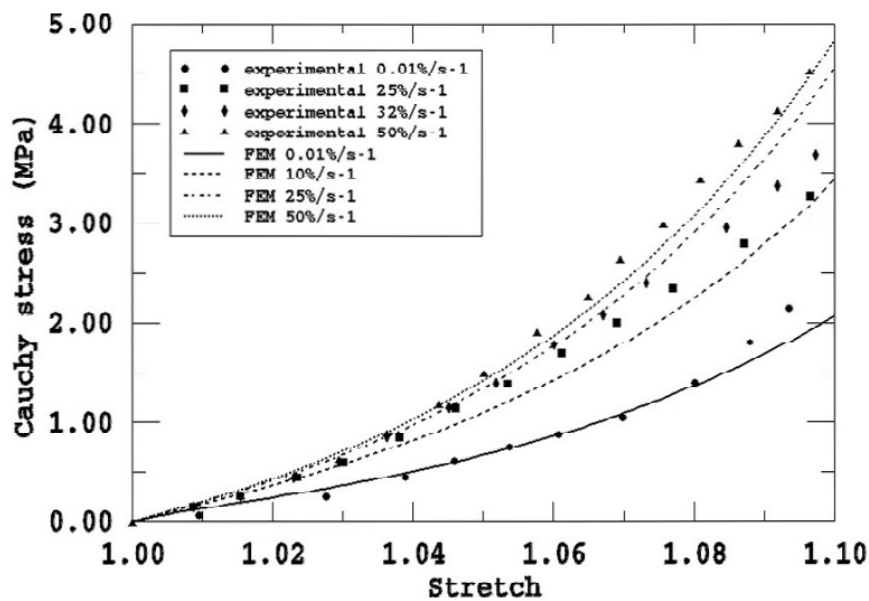


**Figure 3:** Experimental results obtained by [17] and theoretical stress-strain curves at different rates of elongation for the human ACL

**Table 1** ACL elastic, viscoelastic and damage material parameters (Mpa)

$C_1$	$C_2$	$C_3$	$C_4$	D	
1	0.0	0.4	8.1019	8.8e-3	
$\gamma_m$	$\tau_m$	$\gamma_f$	$\tau_f$		
0.31	0.15	0.69	5		
$\psi_{min}^m$	$\psi_{max}^m$	$\beta^m$	$\psi_{min}^f$	$\psi_{max}^f$	$\beta^f$
0.2946	0.4399	0.120	0.9427	1.4086	0.1538

Maximal principal stress distributions in ACL at 0.012%S<sup>-1</sup> and 50%S<sup>-1</sup> of strain rates are presented in Figure 4. The maximal principal stress is located in the central part of the ligament. The maximal principal stress of 7.27 Mpa obtained in the central region for the higher load rate is due to the stiffening effect induced by high load rates. Under physiological strain-rates the maximal principal stress of 4.36 MPa is far from the ultimate stress.

## 4.2 Damage of Human Anterior Cruciate Ligament

The anterior cruciate (ACL) ligament is the most frequent totally disrupted of all the knee ligaments. Sports (sky, basketball, soccer) and traffic accidents are the most important causes of ligament injury. Studies of ligament cutting and measurements of tissue load have shown that ACL provides a primary restraint to anterior-posterior and flexion movement and a secondary restraint to external internal rotation. The purpose of this simulation is to demonstrate the applicability of the model to simulate the structural behavior of soft biological tissues. We reproduce in a human ACL, the experiment developed by [12] in a monkey ACL. That study was performed to determine the viscoelastic behavior of ligaments at different loading rates, such as those associated with sports-related trauma.

The previous human model of the ACL was used to test slow and fast conditions at displacement rates of 0.08467 mm/s and 8.467 mm/s. The elastic, viscoelastic and damage parameters for the human ACL were fitted from published experimental data [1,17] and are shown in Table 1. The fitted curve is shown in Figure 5.

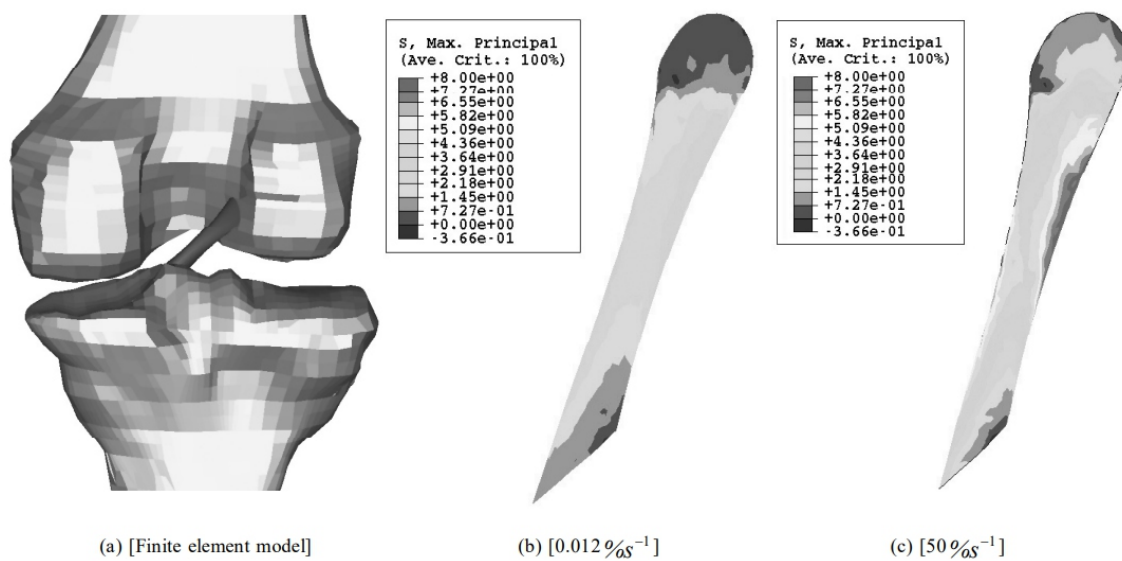


**Figure 4:** Finite element model of the human ACL and maximal principal stress at low and high strain rates (Mpa).

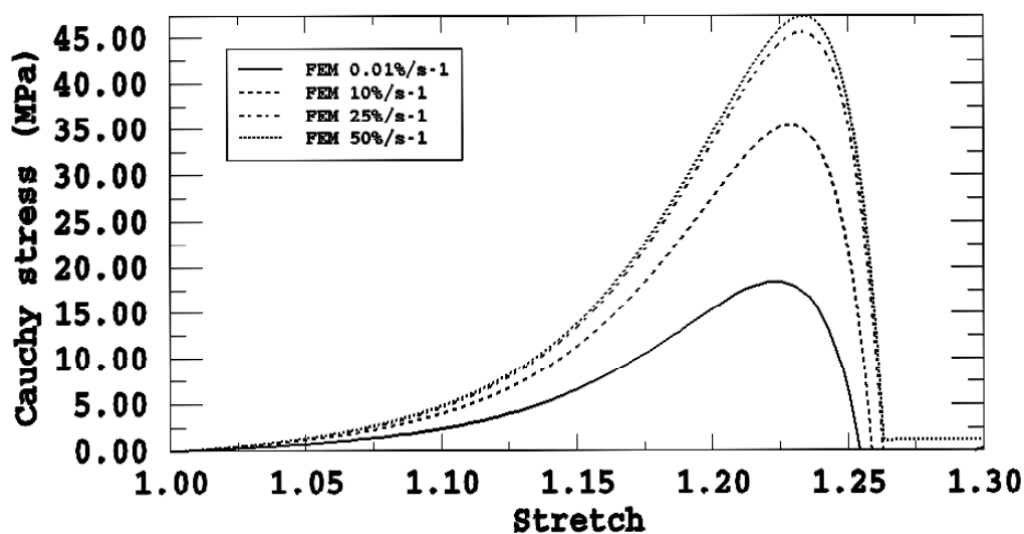


**Figure 5:** Stress-strain response of the human ACL at different displacement rates.

Damage distributions in matrix and fibres at 0.08467 mm/s and 8.467 mm/s of displacement rates are presented in Figures 6 and 7. Due to limitations of the model, we consider failure of the ACL when damage reached a value of 0.55 in both matrix or fibres. We can observe the effect of the strain rate into the damage behavior. At 8.467 mm/s of displacement rate, damage in fibres was much lower (0.34) than at 0.08467 mm/s (0.56). On the contrary, damage in matrix at 8.467 mm/s (0.26) was much higher than at 0.08467 mm/s (0.20). [12] observed that during the failure process, the ligament grossly appears intact while the load is approximately 80 %. The peak values appeared in the ligament substance as has been also reported in previous experimental studies [12].

This is in agreement with the computational results obtained herein due to the damage processes in the matrix substance is lower than in the fibers.

In Table 2 the results are separated according to the strain rate. The overall difference in strength properties at two deformation rates is shown, the load needed until failure at high strain rate is higher than at low strain rate as has been also reported in previous experimental studies [12].

**Table 2** Strain Rate Results by Strain Rate

<i>Strain rate</i>	<i>Maximun load (N)</i>	<i>Strain to failure</i>
Fast	94.88	0.41
Slow	45.1	0.4

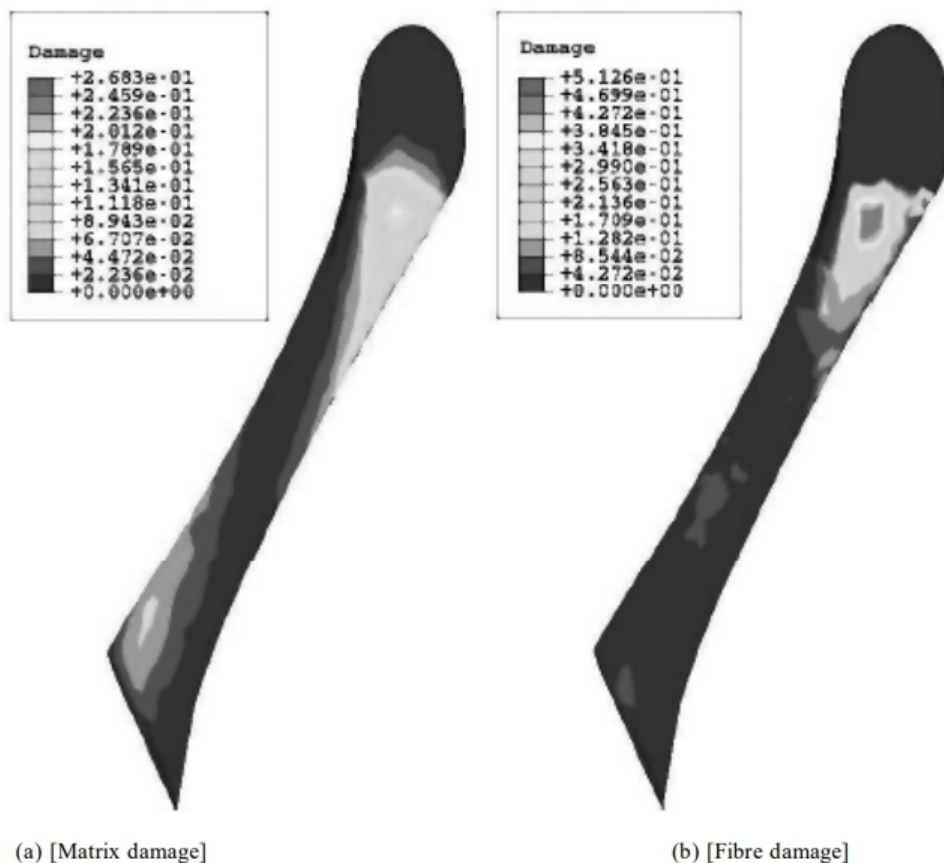


**Figure 6:** Damage in a human ACL at 0.08467 mm/

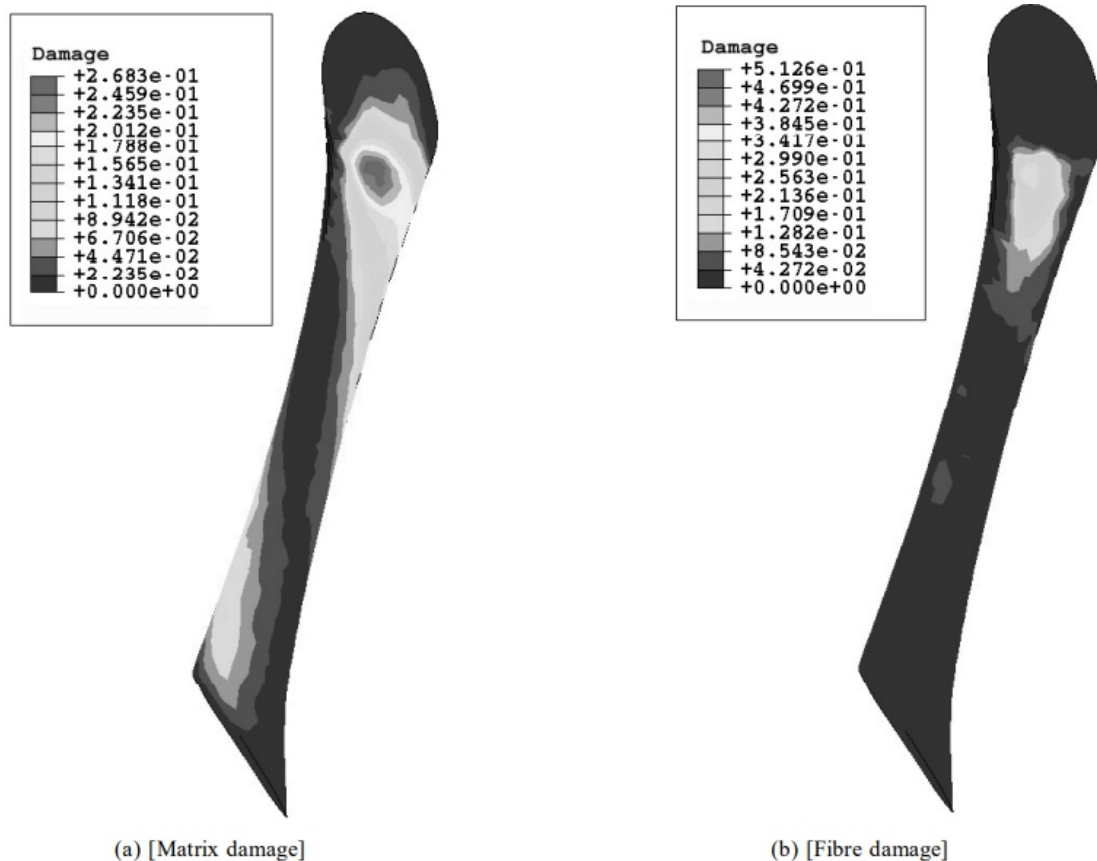


**Figure 7:** Damage in a human ACL at 8.467 mm/s

## 5. DISCUSSION

In this work, we have presented constitutive models that have been used to represent ligaments under non physiological situations. The ultimate goal of these modelling efforts is to improve the clinical diagnosis and treatment of different injuries and disorders of diarthrodial joints. This paper presents visco-hyperelastic and damage models to study the strain softening time-dependent behavior of ligaments. The research question addressed in the paper is to assess whether, in the framework of phenomenological models, a time dependent constitutive damage model with viscoelastic properties different for matrix and reinforcing fibres can predict different experimental evidences in this type of materials [2,20]. From numerical point of view, a general procedure for the simulation of finite strain problems involving dissipative fibred materials has been described in detail. Emphasis has been placed on the numerical treatment of the proposed formulation in the context of the finiteelement method and particular attention has been paid to the derivation of the corresponding tangent tensor, essential for the solution of the implicit finite element equations.

In order to show the performance of the framework presented herein, a complex 3D numerical application to ACL ligament mechanics is presented. Results show that the model is able to capture the typical stress-strain behavior observed in ligaments at non-physiological situations and predict the damage ligament regions that has been reported in previous experimental studies [12].

## 6. ACKNOWLEDGEMENTS

The authors gratefully acknowledge the support of the Spanish Education and Science Ministry (CYCIT DPI2004-07410-C03-01 and FIS2005-05020-C03-03) and the Spanish Ministry of Health

## REFERENCES

- [1] Arnoux, P., P-Chabrand, Jean, M., Bonnoit, J. (2002). *A viscohyperelastic with damage for the knee ligaments under dynamic constraints. Comp Meth in Biomech and Biomedical Eng.* 5, 167–174.
- [2] Bonifasi-Lista, C., Lake, S., Small, M., Weiss, J. (2005). *Viscoelastoc properties of the human medial collateral ligament under longitudinal, transverse and shear loading. J. Orthopaed Res.* 23, 67–76.
- [3] Calvo, B., Peña, E., Martínez, M., Doblaré, M. (2006). *An uncoupled directional damage model for fibered biological soft tissues. Formulation and computational aspects. Int J. Numer Meth Engng.* 69, 2036–2057.
- [4] Danto, M. I., Woo, S. (1993). *The mechanical properties of skeletally mature rabbit anterior cruciate ligament and patellar tendon over range of strain rates. Cursive 11,* 58–67.
- [5] Flory, P. J. (1961). *Thermodynamic relations for high elastic materials. Transaction of the Faraday Societety* 57, 829–838.
- [6] Gardiner, J., Weiss, J. (2003). *Subjet-specific finite element analysis of the human medial collateral ligament during valgus knee loading. J. Orthopaed Res.* 21, 1098–1106.
- [7] Gardiner, J., Weiss, J., Rosenberg, T. (2001). *Strain in the human medial collateral ligament during valgus lading of the knee. Clin Orthop Relat R* 391, 266–274.
- [8] Holzapfel, G. A. (2000). *Nonlinear Solid Mechanics.* Wiley, New York.
- [9] Humphrey, J. D. (2002). *Continuum biomechanics of soft biological tissues. Proc R. Soc Lond A* 175, 1–44.
- [10] Mak, A. (1986). *The apparent viscoelastic behaviour of articular cartilage. The contributions from the intrinsic matrix viscoelastocity and interstitial fluid flows. ASME J. Biomech Engng.* 108, 123–130.
- [11] Natali, A., Pavan, P., Carniel, E., Luisiano, M., Tagliavoro, G. (2005). *Anisotropic elasto-damage constitutive model for the biomechanical analysis of tendons. Med. Eng. Phys.* 27, 209–214.
- [12] Noyes, F., DeLucas, J., Torvik, P. (1974). *Biomechanics of anterior cruciate ligament failure: an analysis of strain-rate sensitivity and mechanisms of failure in primates. J. Bone Joint Surg* 56(A), 236–253.
- [13] Peña, E., Calvo, B., Martínez, M., Doblaré, M. (2006a). *A three-dimensional finite element analysis of the combined behavior of ligaments and menisci in the healthy human knee joint. J. Biomech* 39(9), 1686–1701.
- [14] Peña, E., Calvo, B., Martínez, M. A., Doblaré, M. (2007a). *An anisotropic visco-hyperelastic model for ligaments at finite strains: Formulation and computational aspects. Int. J. Solids Struct* 44, 760–778.
- [15] Peña, E., Calvo, M. A. M. B., Doblaré, M. (2006b). *On the numerical treatment of initial strains in soft biological tissues. Int. J. Numer Meth Engng.* 68, 836–860.
- [16] Peña, E., del Palomar, A. P., Calvo, B., Martínez, M., Doblaré, M. (2007b). *Computational modelling of diarthrodial joints. Physiological, pathological and pos-surgery simulations. Arch Comput Method Eng.* 14(1), 1–54.
- [17] Pioletti, D., Rakotomanana, L., Benvenuti, J.-F., Leyvraz, P.- F. (1998). *Viscoelastic constitutive law in large deformations: application to human knee ligaments and tendons. J. Biomech* 31, 753–757.
- [18] Provenzano, P., Lakes, R., Corr, D., Vanderby, R. (2002). *Application of nonlinear viscoelastic models to describe ligament behavior. Biomech Model Mechanobiol* 1, 45–47.
- [19] Puxkandl, R., Zizak, I., Paris, O., Tesch, W., Bernstorff, S., Purslow, P., Fratzl, P. (2002).

---

*Viscoelastic properties of collagen: synchrotron radiation investigations and structural model. Cursive* 357, 191–197.

[20] Quapp, K., Weiss, J. (1998). *Material characterization of human medial collateral ligament. ASME J. Biomech Eng.* 120, 757–763.

[21] Sasaki, N., Odajima, S. (1996). *Stress-strain curve and Young's modulus of a collagen molecule as determined by X-ray diffraction technique. J. Biomech* 29, 655–658.

[22] Simo, J. (1987). *On a fully three-dimensional finite-strain viscoelastic damage model: Formulation and computational aspects. Comput Methods Appl. Mech Engrg* 60, 153–173.

[23] Simo, J., Taylor, R. (1991). *Quasi-Incompressible Finite Elasticity in Principal Stretches. Continuum Basis and Numerical Algorithms. Comput Methods Appl. Mech. Engrg.* 85, 273–310.

[24] Simo, J. C., Hughes, T. (1998). *Computational Inelasticity. Springer-Verlag, New York.*

[25] Spencer, A. J. M. (1954). *Theory of Invariants. In: Continuum Physics. Academic Press, New York,* pp. 239–253.

[26] Vita, R. D., Slaughter, W. (2006). *A structural constitutive model for the strain rate-dependent behavior of anterior cruciate ligaments. Int J. Solids Struct.* 43, 1561–1570.

[27] Weiss, J., Gardiner, J. C. (2001). *Computational modelling of ligament mechanics. Crit Rev. Biomed Eng.* 29, 1–70.

[28] Weiss, J., Gardiner, J. C., Bonifasi-Lista, C. (2002). *Ligament material behavior is nonlinear, viscoelastic and rate independent under shear loading. J. Biomech.* 35, 943–950.

[29] Weiss, J., Maker, B., S. Govindjee (1996). *Finite element implementation of incompressible, transversely isotropic hyperelasticity. Comput Methods Appl. Mech. Engrg.* 135, 107–128

# Instructions for Authors

## Essentials for Publishing in this Journal

- 1 Submitted articles should not have been previously published or be currently under consideration for publication elsewhere.
- 2 Conference papers may only be submitted if the paper has been completely re-written (taken to mean more than 50%) and the author has cleared any necessary permission with the copyright owner if it has been previously copyrighted.
- 3 All our articles are refereed through a double-blind process.
- 4 All authors must declare they have read and agreed to the content of the submitted article and must sign a declaration correspond to the originality of the article.

## Submission Process

All articles for this journal must be submitted using our online submissions system. <http://enrichedpub.com/> . Please use the Submit Your Article link in the Author Service area.

---

## Manuscript Guidelines

The instructions to authors about the article preparation for publication in the Manuscripts are submitted online, through the e-Ur (Electronic editing) system, developed by **Enriched Publications Pvt. Ltd.** The article should contain the abstract with keywords, introduction, body, conclusion, references and the summary in English language (without heading and subheading enumeration). The article length should not exceed 16 pages of A4 paper format.

### Title

The title should be informative. It is in both Journal's and author's best interest to use terms suitable. For indexing and word search. If there are no such terms in the title, the author is strongly advised to add a subtitle. The title should be given in English as well. The titles precede the abstract and the summary in an appropriate language.

### Letterhead Title

The letterhead title is given at a top of each page for easier identification of article copies in an Electronic form in particular. It contains the author's surname and first name initial .article title, journal title and collation (year, volume, and issue, first and last page). The journal and article titles can be given in a shortened form.

### Author's Name

Full name(s) of author(s) should be used. It is advisable to give the middle initial. Names are given in their original form.

### Contact Details

The postal address or the e-mail address of the author (usually of the first one if there are more Authors) is given in the footnote at the bottom of the first page.

### Type of Articles

Classification of articles is a duty of the editorial staff and is of special importance. Referees and the members of the editorial staff, or section editors, can propose a category, but the editor-in-chief has the sole responsibility for their classification. Journal articles are classified as follows:

#### Scientific articles:

1. Original scientific paper (giving the previously unpublished results of the author's own research based on management methods).
2. Survey paper (giving an original, detailed and critical view of a research problem or an area to which the author has made a contribution visible through his self-citation);
3. Short or preliminary communication (original management paper of full format but of a smaller extent or of a preliminary character);
4. Scientific critique or forum (discussion on a particular scientific topic, based exclusively on management argumentation) and commentaries. Exceptionally, in particular areas, a scientific paper in the Journal can be in a form of a monograph or a critical edition of scientific data (historical, archival, lexicographic, bibliographic, data survey, etc.) which were unknown or hardly accessible for scientific research.

**Professional articles:**

1. Professional paper (contribution offering experience useful for improvement of professional practice but not necessarily based on scientific methods);
2. Informative contribution (editorial, commentary, etc.);
3. Review (of a book, software, case study, scientific event, etc.)

**Language**

The article should be in English. The grammar and style of the article should be of good quality. The systematized text should be without abbreviations (except standard ones). All measurements must be in SI units. The sequence of formulae is denoted in Arabic numerals in parentheses on the right-hand side.

**Abstract and Summary**

An abstract is a concise informative presentation of the article content for fast and accurate Evaluation of its relevance. It is both in the Editorial Office's and the author's best interest for an abstract to contain terms often used for indexing and article search. The abstract describes the purpose of the study and the methods, outlines the findings and state the conclusions. A 100- to 250-Word abstract should be placed between the title and the keywords with the body text to follow. Besides an abstract are advised to have a summary in English, at the end of the article, after the Reference list. The summary should be structured and long up to 1/10 of the article length (it is more extensive than the abstract).

**Keywords**

Keywords are terms or phrases showing adequately the article content for indexing and search purposes. They should be allocated heaving in mind widely accepted international sources (index, dictionary or thesaurus), such as the Web of Science keyword list for science in general. The higher their usage frequency is the better. Up to 10 keywords immediately follow the abstract and the summary, in respective languages.

**Acknowledgements**

The name and the number of the project or programmed within which the article was realized is given in a separate note at the bottom of the first page together with the name of the institution which financially supported the project or programmed.

**Tables and Illustrations**

All the captions should be in the original language as well as in English, together with the texts in illustrations if possible. Tables are typed in the same style as the text and are denoted by numerals at the top. Photographs and drawings, placed appropriately in the text, should be clear, precise and suitable for reproduction. Drawings should be created in Word or Corel.

**Citation in the Text**

Citation in the text must be uniform. When citing references in the text, use the reference number set in square brackets from the Reference list at the end of the article.

**Footnotes**

Footnotes are given at the bottom of the page with the text they refer to. They can contain less relevant details, additional explanations or used sources (e.g. scientific material, manuals). They cannot replace the cited literature.

The article should be accompanied with a cover letter with the information about the author(s): surname, middle initial, first name, and citizen personal number, rank, title, e-mail address, and affiliation address, home address including municipality, phone number in the office and at home (or a mobile phone number). The cover letter should state the type of the article and tell which illustrations are original and which are not.

